Characterization of thermophysical properties and measurement by multispectral pyrometry

Thomas Pierre

HABILITATION À DIRIGER DES RECHERCHES

UNIVERSITE BRETAGNE SUD

Thomas PIERRE

Characterization of thermophysical properties and measurement by multispectral pyrometry

Rapporteurs avant soutenance :

Agnès DELMAS	Maître de conférences HDR, INSA Lyon, France
Thierry DUVAUT	Professeur des universités, Université Reims Champagne-Ardenne, France
Christophe LE NILIOT	Professeur des universités, Aix-Marseille Université, France

Composition du Jury :

Président :	Filippo de Monte	
Examinateurs :	Filippo de MONTE	Professore ordinario, Università degli Studi dell'Aquila, Italia
	Philippe LE MASSON	Professeur des universités, Université Bretagne Sud, France
	Helcio R. B. ORLANDE	Professor, Universidade Federale do Rio de Janeiro, Brasil

Summary

Introduction 7

1. Curriculum Vitæ 13

1.1. University training, 1998-2004 13

1.2. PhD, 2004-2007 14

1.3. Postdoctoral application, Jan. – Jul. 2008 15

2. Teaching and responsibilities 17

2.1. During my PhD 17

2.2. Teaching at the Université Bretagne Sud 17

3. Scientific investments, supervision, and production 21

3.1. Scientific investments 21

3.2. Scientific supervision 22

3.3. Scientific production 25

Nomenclature 35

4. Characterisation of thermal properties by heating contact techniques 39

4.1. Estimation of thermal properties of insulating bio-sourced material with the hot-strip technique and influence of the temperature and humidity 39

4.2. Estimation of the conductive and radiative properties of bio-aerogel with a transient pulsed technique 50

4.3. Infrared thermography for the in-plane thermal properties estimation of materials in a large range of thermal conductivity 61

4.4. Conclusion 78

References 79

5. Temperature emissivity estimation with multispectral pyrometry 87

5.1. Some basics on multispectral pyrometry 87

5.2. The selection of the wavelengths 102

5.3. The simultaneous temperature emissivity estimation 109

5.4. Conclusion 129

References 130

6. Characterization of thermal properties by non-contact techniques 135

6.1. The estimation of the thermal diffusivity of metals at temperature close to the melting point with the aerodynamic levitation 136

6.2. The estimation of the thermal diffusivity of metals at temperature close to the melting point with the second apparatus 149
6.3. Conclusion 157
References 158
General conclusion and perspectives 161

Introduction

Between 2004 and 2007, I made my PhD at the LEMTA, a laboratory of the Université de Lorraine. The subject of my PhD dealt with the microscale temperature measurement by bispectral pyrometry using photon counting in the UV-visible spectral range. This work was mainly experimental and I acquired skills in radiative transfer for the theoretical part, in pyrometry for the experiment part, and also in inverse techniques since the temperature was estimated simultaneously with the emissivity.

Between January and July 2008, I made a post-doctoral application at the University of Quebec in Chicoutimi, in the CURAL laboratory. My acquired skills during my PhD in radiative transfers and inverse techniques allow me to work on infrared tomography for the detection of radiative properties in semi-transparent medium. This work was exclusively numerical but the aimed applications were the detection of cancerous tumours in the human tissues.

Since September 2008, I had a position of Associate Professor at the Université Bretagne Sud, and I share equally my time between teaching in the department Métiers de la Transition et de l'Efficacité Énergétiques (ex Génie Thermique et Énergie) of the Institut Universitaire Technologique and research in the Institut de Recherche Dupuy de Lôme (IRDL). I am a member of the team Assemblages multi-matériaux, one of the five research teams of the IRDL. Its activities are focused on the development, the characterization, and the modelling of processes dedicated to the assembly of materials of different natures [PTR2].

First, I participated to the ANR project "Béton de chanvre" in 2008-2012 (Section 4.1). This project came within the scope of reducing the important energy consumption in the building. I worked on the definition and the characterization of the bio-sourced materials, the hemp concretes. Hemp concretes, considered heterogeneous, anisotropic, and porous material, are obtained by mixing a lime-based binder, hemp particles and water. They have the ability to breathe thanks to its high porosity: air more or less filled with water circulates there. The migrations of water and energy in the volume make its study complex.

In the continuity of working on insulating materials, the "composite" team of the IRDL, in collaboration with the INRA in Nantes, wanted to develop a bio-aerogel and it proposed me to characterize it and to determine the contribution of the inner radiative

and conductive transfers (Section 4.2). Indeed, classical aerogels are super insulating materials with thermal conductivity close to air thermal conductivity where radiative-conductive coupling occurs. At the same time, I continued to study hemp concrete by characterizing its millimetric component: the hemp shiv (Section 4.3). Literature did not mentioned properties of this cellulosic material. For this I developed the use of temperature-temperature analytical model and dedicated experiment to characterize those particles.

These first projects, developed in Section 4, allowed me to develop a systematic methodology in order to conduct scientific works: the setting up of experimental protocols from analytical models and sensitivity studies. Experimental protocol to estimate these properties is developed from a direct model. It is function of properties of interest (conductivity, diffusivity, thermal capacity) and minor others (thermal losses). All are more or less related to each other, and they must be estimated. Sensitivity study is then necessary to be able to answer these two questions: i) what is the level of correlation between these properties? ii) is the correlation between properties time-dependent? By playing on input parameters of the direct model, answers to these questions define maximum duration of the experiment, dimensions of the sample, time and type of heating, what to measure and where to place the measuring probes…

Once experimental protocol has been defined, estimation of parameters is tested from noisy data obtained from direct model. Estimation is carried out by inverse techniques; for example, minimizing the quadratic error between experimental temperature measured (observable) and that given by the direct model at the same location (least squares with Levenberg-Marquardt type optimization algorithm). There are several ways to develop direct models. I mainly work with analytical and semi-analytical models. Most of the time, they have the advantage over numerical ones of operating faster. However, they are more limited because analytical solution to a problem is not always available, or by means of more difficult mathematical tools. The method of thermal quadrupole is very convenient for establishing multilayer analytical models. And addition of Laplace and Fourier integral transformations deals with transient, periodic, and multidirectional problems. However, the use of analytical model often requires to consider constant physical properties, thus constraining the experiment: input of energy such as the maximum temperature rise of the sample leads to variation in physical properties less than uncertainty in their estimation.

I became familiar with the characterization techniques of the hot-plate or hot-strip commonly used. But they remain difficult to perform serenely due to difficulty of controlling the instrumentation necessary for the experiment: thermal properties of heating element used for the thermal stress, contact resistance, heating element/sample contact surface, quantity of energy deposited, position of the thermocouples. Classical theoretical models have flux as input quantity and temperature as observable; they are flux-temperature models and impedance connects both of them. However, uncertainty on the flux actually absorbed by the sample is significant; the part absorbed can be very different from that emitted by the heating element. Therefore, I turned to the development of theoretical temperature-temperature models, which offer favorable outcome to limit the number of uncertain input data. For example, two thermocouples on either side of sample measure both input and the observable, therefore number of parameters to be estimated in the transmittance becomes limited to physical properties of the sample and the heat losses. Experimentally, measurements at ambient temperature by thermocouples have been used for characterization of bio-aerogels, where conductive radiative coupling is present (Section 4.2); but also, by infrared and visible thermography for, first, the study at room temperature of anisotropic materials of millimetric dimensions in order to characterize hemp shiv (Section 4.3), and, second, to estimate the thermal diffusivity of metals close to their melting point (Section 6.2).

Indeed, part of PTR2 has been working for more than twenty years in collaboration with companies (ArcelorMittal, Schneider, EDF, CEA, Stellantis, Framatome, Naval Group) specializing in all types of welding or additive manufacturing. One of PTR2 contributions is to perform numerical simulations of these processes using commercial codes such as Comsol Multiphysics®. Industrial processes being highly multiphysical (thermal, mechanical, hydrodynamic, metallurgical, electromagnetism...), large number of physical properties is required and over a wide temperature range since the matter changes from the solid state to the liquid state and can reach its boiling point. However, the literature is almost mute from the liquid state and beyond. That is why PTR2 started in 2012 the development in the laboratory of high temperature apparatuses in order to characterize liquid metals: for example, a device of aerodynamic levitation of metal balls melted by a laser. The aimed properties are density, surface tension, viscosity, thermal diffusivity, radiative properties, and temperature. I participated and still participate to the estimation

of all these properties, but mainly the temperature and radiative properties (Section 5) and thermal diffusivity (Section 6).

Section 5 deals with the simultaneous estimation of temperature and emissivity of metals. Due to temperature that can up to 3 000 K, the disturbances of environment and atmosphere are negligible. The experience of my thesis dedicated to multispectral pyrometry enabled me to develop at IRDL in 2012 a six-wavelength pyrometer for estimating the temperature and emissivity of metals carried beyond their melting point (Section 5.1). This home-made six-wavelength pyrometer was first calibrated using a home-made blackbody. Radiative fluxes are then directly measured by the pyrometer, upon solid-liquid phase change of the metal balls. Temperature is estimated using the multispectral pyrometry, but it is difficult to address for several reasons. The system to be solved is underdetermined, it systematically includes one more unknown than equations. Indeed, radiative flux emitted by a surface depends on two parameters: temperature and emissivity. Thus, for N radiative fluxes measured at the same temperature at a given time, there are $N+1$ unknowns: N emissivities and temperature (Section 5.2). One solution is to propose a spectral model of emissivity. The literature offers many physical and mathematical models, based on electromagnetic theory or experiment. Unfortunately, the behavior of the surface state is for the most part difficult to control satisfactorily from one experimental apparatus to another, but also from one experiment to another for a given apparatus. The unpredictability of emissivity increases with the dynamic of the experiment. In our case, we are exposed to the following issues: the temperature change of several thousands of kelvins in a few seconds, the diffusion, the presence of oxygen (even residual), the changes of state, the impurities. Therefore, establish a behavioral model of the emissivity believable is almost impossible with a good confidence. However, the low spectral range of the home-made multispectral pyrometer allows the use of simple polynomial models of maximum order 1. It is with this strong hypothesis that estimates of temperature and emissivity of metals have been established. In addition, tests with different emissivity models, inverse techniques of different kinds were compared (Section 5.3): deterministic methods (least squares previously presented) and stochastic methods (different techniques of Bayesian inference). Only the wavelength dependence for the emissivity model is considered since an estimate is made for each time step, whether dynamic or static.

Experience acquired with pyrometry allowed me to work on thermal diffusivity estimation using radiative fluxes instead of direct temperatures, which is not possible due to the high temperatures of liquid metals (Section 6). First attempts focused on the feasibility of estimating thermal diffusivity of liquid metallic droplet during levitation (Section 6.1). Different direct models in spherical coordinates (Section 6.1) and Cartesian coordinates (Section 6.2) have been developed using inputs and observables of different nature: power of the laser, radiative fluxes measured by the six-wavelength pyrometer, by high speed camera...

To sum up, my field of research is two-fold: i) the development of experimental protocols dedicated to the characterization of physical properties of materials; ii) the measurement of temperature and emissivity through multispectral pyrometry. Both themes joint themselves with the common use of inverse techniques, necessary tools as long as more than one parameter needs to be estimated when one experiment is performed.

This document tries to be the reflect of both aspects of my work, and mainly the research one. It is constructed as follows. My curriculum vitae is presented in Section 1. It concerns my university training since 2004 until my present position. Section 2 is the teaching I did in Nancy – as a monitor –, but especially in Lorient in the department named Métiers de la Transition et de l'Efficacité Énergétiques (ex Génie Thermique et Énergie) and at the Faculty of Science. My administrative responsibilities are also presented. Section 3 deals with my scientific investments, supervisions, and publications. Then Sections 4 to 6 relate to my actual research works. They detail what was previously introduced, but I took care to present at the end of each section a synthetic conclusion and also a perspective. Finally, a general conclusion and perspectives Section proposes major axes of future works. Even if it is not conventional, I add a general nomenclature before Section 4. Each section has its own list of bibliographical references presented in this manner [First author Year].

1. *Curriculum vitæ*

1.1. University training, 1998 – 2007

After I first passed a two years diploma, DUT Mesures Physiques, I focused my formation in the field of mechanical engineering, and more specifically the heat transfers. Between 2001 and 2004, I successively passed my bachelor and masters (Licence, Maîtrise, and DEA). Table 1.1 is a synthesis of my diplomas obtained at the university.

Table 1.1. Synthesis of my diplomas.

1998	Baccalauréat STL Physique, Chalon-sur-Saône (71).
1998-2001	DUT Mesures Physiques, Université de Bourgogne, Le Creusot (71).
2001-2003	Licence/Maîtrise IUP Transferts Thermiques, Faculté des Sciences de Reims (51).
2003-2004	DEA Énergétique Physique, Institut National Polytechnique de Grenoble (INPG), Grenoble (38).

The first internship dedicated to research was during my DEA in Grenoble in 2004. M. Alain Chiron de La Casinière (associate professor), from the IRSA laboratory (Interaction entre le Rayonnement Solaire et l'Atmosphère) of the Université Joseph Fourier, proposed me to study the measurement methods of the zenith intensity (*Étude de méthodes de mesure de la luminance zénithale* [Pierre 2004]). I shared my time between Grenoble and Besançon, one of the sunniest cities of France. The subject and its motivations are the following. The decrease of the ozone quantity on Earth imposed the creation of stations all around the Earth dedicated to the measurement of ground solar irradiance, in order to control its temporal evolution. IRSA laboratory belongs to an international network of stratosphere observation (Network for the Dectection of Atmosferic Chemical Change, NDACC). It possesses a measurement station composed of an ultraviolet spectroradiometer and a system able to record, treat, and convert raw data into irradiances. In the case of my internship, the station is equipped of a "barrel" in order to aim specifically the zenith and is used to determine zenith intensity. The objective of my internship was to test a method proposed by A. de La Casinière [de La Casinière 2003] to convert the raw data collected by the spectroradiometer into intensity. After calibration of the spectroradiometer equipped with the barrel, results were successfully

obtained since experimental intensities were compared with those obtained by the resolution of the radiative transfer equation.

This internship was mostly experimental but I worked on the radiative transfer equation and the solar radiation. It allowed me to discover the principle of the photon counting with a spectroradiometer and its calibration procedure.

No communication has been proposed for this work.

References

[de La Casinière 2003] Alain Chiron de la Casinière, Le rayonnement solaire dans l'environnement terrestre, Publibook, Paris, 2003.

[Pierre 2004] T. Pierre, *Étude de méthodes de mesure de la luminance zénithale*, rapport de stage, DEA Énergétique Physique, INPG, 2004.

1.2. PhD, 2004 – 2007

I realized my PhD at LEMTA (Laboratoire d'Énergétique de Mécanique Théorique et Appliquée) and defended it to obtain the title of Docteur en Mécanique Énergétique de Nancy-Université. My work was supervised by Professors A. Degiovanni et B. Rémy (at the time Associate Professor). Its title was *Microscale temperature meausurement by optical way in the ultraviolet-visible spectral range* (*Mesure de la température à l'échelle microscopique par voie optique dans la gamme ultraviolet-visible*). These works were at the same time theoretical and experimental. The temperature of opaque surface was estimated through inverse methods with the help of the multispectral pyrometry and the photon counting.

Mostly experimental, a great part of my work was dedicated to the development of an optical bench and of a high temperature blackbody of small dimensions. This work also was the opportunity to use diverse experimental apparatuses: infrared camera, quantum detectors, FTIR spectroradiometer, for example. Nevertheless, my PhD had been the opportunity to discover the quadrupole methods, to perform parameter estimation with the use of inverse techniques (Levenberg-Marquardt), and develop numerical model with the help of MatLab or FlexPDE.

Some results of my PhD are presented in Section 5 of this manuscript. In addition, the results obtained along my PhD have been published according to the following

references in Section 3.3: [ACL1], [ACL6], [ACTI], [ACTN1], [ACTN2], [ACTN3], [ACTN4], and [OP1].

1.3. Postdoctoral application, Jan. – Jul. 2008

My post-doctoral application was set at the CURAL (Centre Universitaire de Recherche sur l'Aluminium), a laboratory of the UQAC (Université du Québec À Chicoutimi) under the supervision of Professor André Charette between January and July 2008. The subject was *Optical tomography – Inverse techniques for the determination of radiative properties (scattering and diffusion coefficients) in a semi-transparent medium*.

In this inverse problem, the direct model was based on the radiative transfer equation and the inversion was performed with the gradient technique. The work was only numerical. One of the possible applications is the detection of cancerous tumours in the human tissues.

The results of this internship were published according to the following references in Section 3.3: [ACL2], [ACT5] [COM2].

2. Teaching and responsibilities

2.1. During my PhD

During my PhD, I did tutorials as a temporary worker the first year and then as a monitor for the next two years under the supervision of Professor Denis Maillet. Table 2.1 summarizes these lessons with a total volume of 193.5 hTD. The courses were given to first-year students of the engineering cycle of the l'École Nationale Supérieure en Génie des Systèmes Industriels (ENSGSI) and to first-year students of the preparatory cycle of the l'École Européenne d'Ingénieurs en Génie des Matériaux.

Table 2.1. Synthesis of classes taught during my PhD.

		2004/2005	2005/2006	2006/2007
Heat transfers	TD	16	20	10
	TP	40	40	40
Mechanics	TD		7.5	
Materials	TP			20

2.2. Teaching at the Université Bretagne Sud

I do most of my teaching in the department Métiers de la Transition et de l'Efficacité Énergétiques (MTE2, ex Génie Thermique et Énergie, GTE) of the Institut Universitaire Technologique in Lorient, one of the components of Université Bretagne Sud. Figures 2.1 and 2.2 attempt to summarize the courses given during the period 2008-2023, according to the following presentation where the numbers in parentheses are the hours in front of students: discipline (lecture/tutorial/practical work). The colour code is blue for the lecture, orange for the tutorial, and green for the practical work.

Moreover, Figures 2.3 and 2.4 summarize the hours done in the period 2008/2023. Figure 2.3 shows the distinction between the service due (in blue) and the additional hours (in orange). Figure 2.4 shows the distinction between the hours done in front of students and the hours equivalent to administrative responsibilities and others.

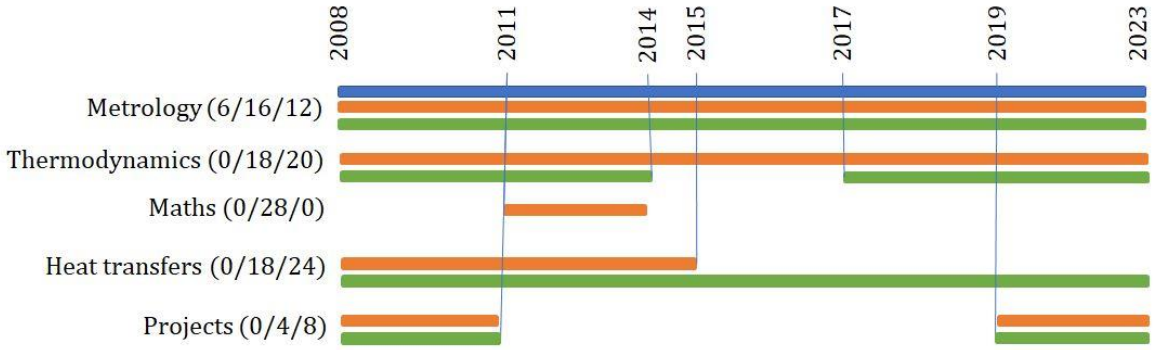

Figure 2.1. Disciplines and hours in BUT1 according to the following presentation: discipline (lecture/tutorial/practical work). Blue: lecture, orange: tutorial, green: practical work.

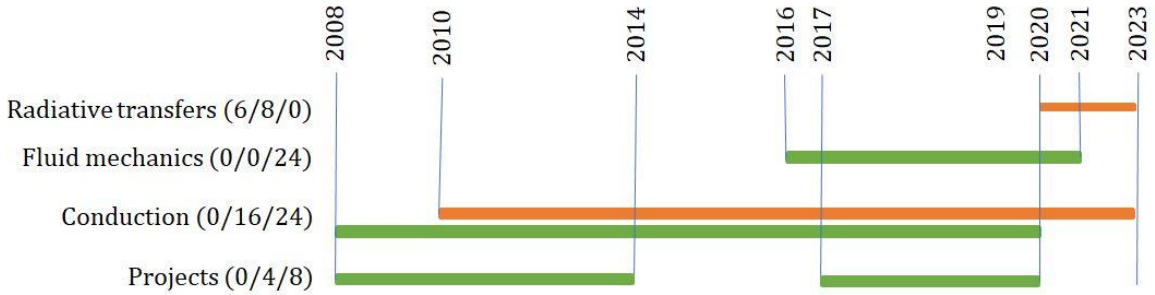

Figure 2.2. Disciplines and hours in BUT2 according to the following presentation: discipline (lecture/tutorial/practical work). Orange: tutorial, green: practical work.

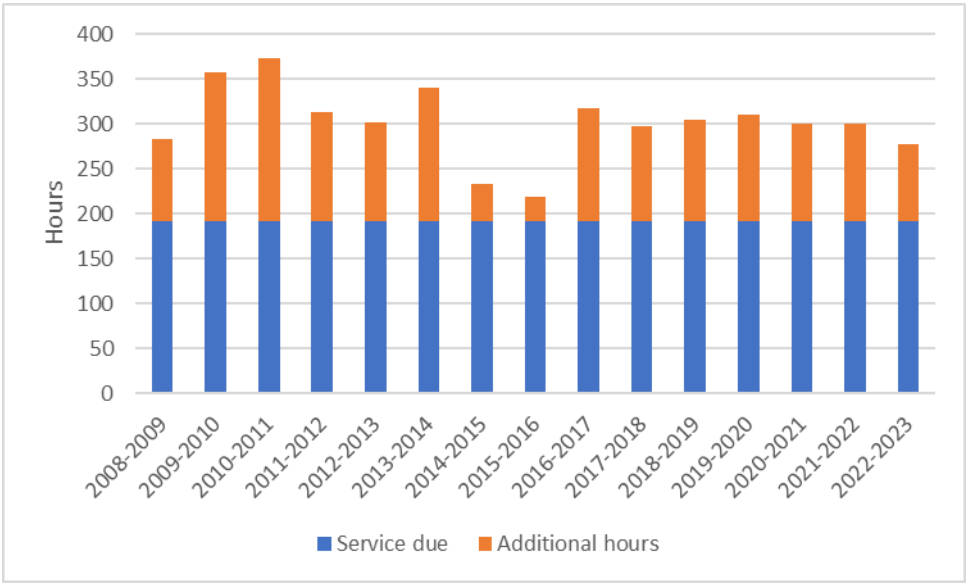

Figure 2.3. Evolution of my annual teaching.

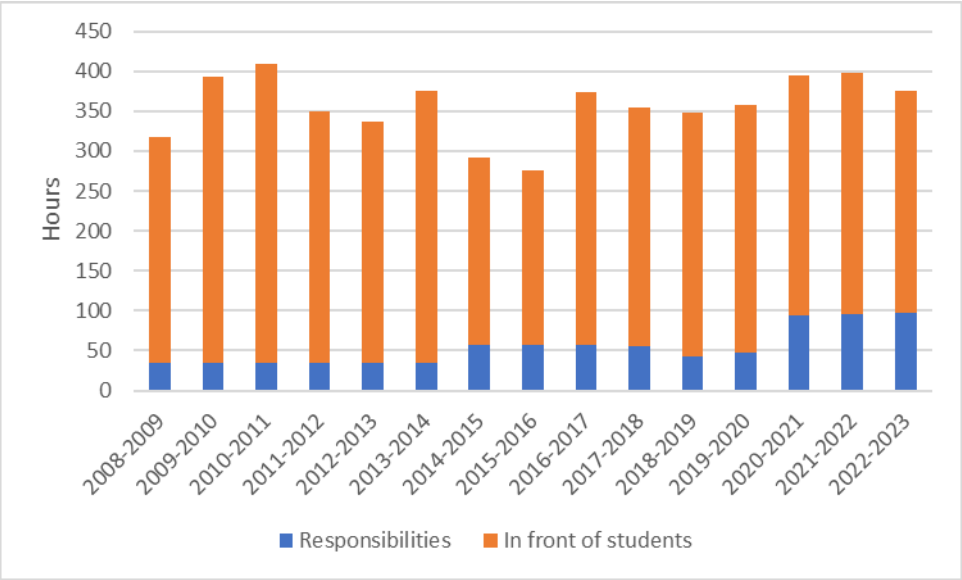

Figure 2.4. Distinction between hours in front of students (blue) and hours due to responsibilities (orange).

At the same time, I held and hold the following pedagogical responsibilities:

- 2014/2017: director of studies, establishment of the timetables for the following students: MT2E1/MT2E2/MT2E2 apprentices;
- 2018/2021: Parcoursup referent for student recruitment;
- 2020/2023: director of studies, establishment of the timetables for the following students: MT2E1/MT2E2/MT2E2 apprentices.

I also take part at the UFR SSI energy specialty in various fields:

- since 2014/2015: Master degree level, radiative metrology (lecture, 4h)
- 2019/2020: level L3, fluid mechanics/energetics (practical works, 24h)
- regular monitoring of trainees (2 or 3 per year, Bachelor to Master degrees).

3. Scientific investments, supervision, and production

3.1. Scientific investments

At the national level, I am an active member of the French thermal society (SFT) and I participate in the High temperatures thematic (2013, 2016, 2023). In addition, for the national SFT congress, I review two or three articles annually.

I have never held a project of my own but I had and still am involved in some:

- In 2008, I first participated in the ANR project (research national agency) Béton de chanvre, supervised by Professor Patrick Glouannec of the Université Bretagne Sud.
- Between 2021 and 2023, three unsuccessful attempts have been made to work on simultaneous temperature emissivity estimation through ANR project. I am responsible for the IRDL of this ANR project in partnership with several French laboratories and companies (IUSTI, ITheMM, CERTES, THEMACS). The proposed project, supervised by Professor Thierry Duvaut of the Université de Reims Champagne-Ardenne.
- Still in 2023, Associate Professor Mickaël Courtois of the Université Bretagne Sud proposed an ANR project dedicated to the thermal characterization of physical properties of liquid metals. If it is accepted, I will be involved in this project.

I co-supervised two thesis through collaborations with ArcelorMittal (thesis of E. Geslain, 2015-2018) and with Mapepas research chair (thesis of L. Dejaeghere, 2012-2016).

I realized deliveries for Orolia, company specialized in the development of emergency beacons: evaluation by infrared thermography of beacon surface temperature increase caused by internal lithium battery thermal runaway.

I organized a working day dedicated to the model reduction (December 9th 2021) in collaboration with LMEE from Université d'Evry.

I participate in thematic schools of Thermal Measurements and Inverse Techniques METTI (2005, 2015, 2019 and in project 2023), for which I presented two dedicated workshops "measurement by the hot plane method" (9h) and "multispectral

pyrometry" in 2019, and will also present in 2023 a lecture on the simultaneous estimation of temperature and emissivity in multispectral pyrometry.

At the international level, in 2008 I made my post-doctoral application at the University of Quebec at Chicoutimi (see Section 1.2). I experimented with the use of inverse techniques in the field of optical tomography.

Recently, I was invited from October 1st to November 30th, 2022 at the Federal University of Rio de Janeiro (UFRJ) thanks to a collaboration with Professor Helcio R. B. Orlande from the University of Rio de Janeiro, Brazil. I worked on the temperature emissivity estimation using different inverse techniques. During this journey, I was able to present this work during a seminar at UFRJ and as an invited lecturer at the Brazilian national thermal congress ENCIT2022 in Bento Gonçalves [INV1]. I had the opportunity to give course (8h) during my stay. This course was delivered to students in Master degree of preparation for their PhD and dealt with radiative metrology and temperature/emissivity estimation by multispectral pyrometry.

Florian Pradelle, Associate professor in the department of mechanical engineering of the Pontifícia Universidade Católica do Rio de Janeiro (Brazil), proposed me to present next November a video conference for graduated students.

I have reviewed 6 articles over the period 2016-2023 for several international journals: International journal of thermophysics, Heat transfer engineering, Building performance, Applied thermal engineering, Inverse problems in science engineering.

I also reviewed, for the title of Doctor Europaeus, the PhD manuscript of Andrea Morcerino, Università di Parma, Italy: Inverse heat transfer approach for heat exchanger characterization, February 12, 2019, work supervised by Professor Fabio Bozzoli.

3.2. Scientific supervision

Tables 3.1 to 3.3 gather all my supervision, respectively, for PhD students (4 defended PhD, 1 in progress), Master Degree students, and Under graduation degree students. The name of all the supervisors are mentioned for the PhD supervision.

Table 3.1. PhD supervision.

Student	Years	Work
Jad Houssein	2021-2024	Determination of the thermal diffusivity of liquid metals at high temperature. Support: IRDL/région Bretagne Carin M. (20 %), Courtois M. (40 %), me (40 %) Present situation : PhD student Associated publications: ACL21, ACTI19
Dylan Le Maux	2017-2020	Physical properties characterization of liquid metals through aerodynamic levitation. Support: IRDL/région Bretagne Le Masson P. (20 %), Courtois M. (45 %), me (35 %) Defense: post-doctoral application, IRDL Associated publications: ACL13, ACL14, ACL15, ACL16, ACL17, ACL18, ACL19, ACL20, ACTI15, ACTI16, ACTI17, ACTI18, ACTN22, ACTN24, ACTN25, COM8
Edouard Geslain	2014-2018	Resistance spot welding of thin coated steel sheets: nugget development in a three-steel sheet assembly. Support: CIFFRE ArcelorMittal Rogeon P. (50 %), Pouvreau C. (25 %), me (25 %). Defense: January 2018 Present situation: contractual employee, Université Bretagne Sud Associated publications: ACL9, ACL15, ACTI9, ACTI13, ACTN17, ACTN18, ACTN20, ACTN23, COM3, COM4, COM7, 0P2
Clara Jimenez-Saelices	2013-2016	Development of thermally super-insulating materials from cellulosic nanofibers. Support: IRDL/INRA Grohens Y. (25 %), Séantier B. (25 %), Cathala B. (25 %), me (25 %) Defense: October 2016

		Present situation: R&D Project Manager in Physico Chemistry at Huddle Corp Associated publications: ACL8, ACTI10
Laurent Dejaeghere	2013-2016	Measurements by multispectral pyrometry and development of a high temperature apparatus. Support: Mapepas research chair Le Masson P. (30 %), Carin M. (30 %), me (40 %). Defense: July 2016. Present situation: senior analyst – Avanade Associated publications: ACL10, ACTI7, ACTI8, ACTI11, ACTN14, ACTN15, ACTN16, COM2, COM5

Table 3.2. Master degree supervision.

Student	Year	Work
Mika Ranaivo	2022	Measurement of the viscosity of liquid metals by aerodynamic levitation.
Thibault Faisandier	2021	Modeling of a process dedicated to the thermal characterization.
Clémantyne Aubry	2019	Simultaneous estimation of temperature and emissivity by least-squares and bispectral pyrometry.
Maxime Capp	2018	Developments of algorithms based on least-squares dedicated to the simultaneous estimation of temperature and emissivity for the thermal diffusivity estimation of liquid metals during aerodynamic levitation
Dylan Le Maux	2017	Radiative measurements through multispectral pyrometry. Application to liquid metals during aerodynamic levitation.
Florian Gesbert	2016	Thermal characterization of materials through random heating – application to insulating materials.

Table 3.3. Under graduation degree supervision.

Student	Year	Work
Tom Guehenneux	2023	Surface tension of liquid metal measurements through aerodynamic levitation.
Maxime Lumeau	2019	Characterization of thermal properties of bituminous materials.
Thomas Lenice	2018	High temperature characterization of materials. Application to aerodynamic levitation and laser heating.
Maxime Bastard	2015	Development of an apparatus dedicated to temperature measurement by multispectral pyrometry during a welding process.

3.3. Scientific production

Table 3.4 gathers all the publications since 2006. The classification has been made according to the HCERES proposition (the link is given in the legend of Table 3.4). Moreover, Figures 3.1 and 3.2 present the progression of the published articles since 2006, only ACL, C-ACTI, and C-ACTN are presented.

Table 3.4. Number of publications since 2006 (classified according to the HCERES).

International publications (ACL)	21
International communications (C-ACTI)	20
National communications (C-ACTN)	26
Invited conference (C-INV)	1
Book chapters (COS)	8
Seminars and conferences (COM)	8
Other publications (AP)	2

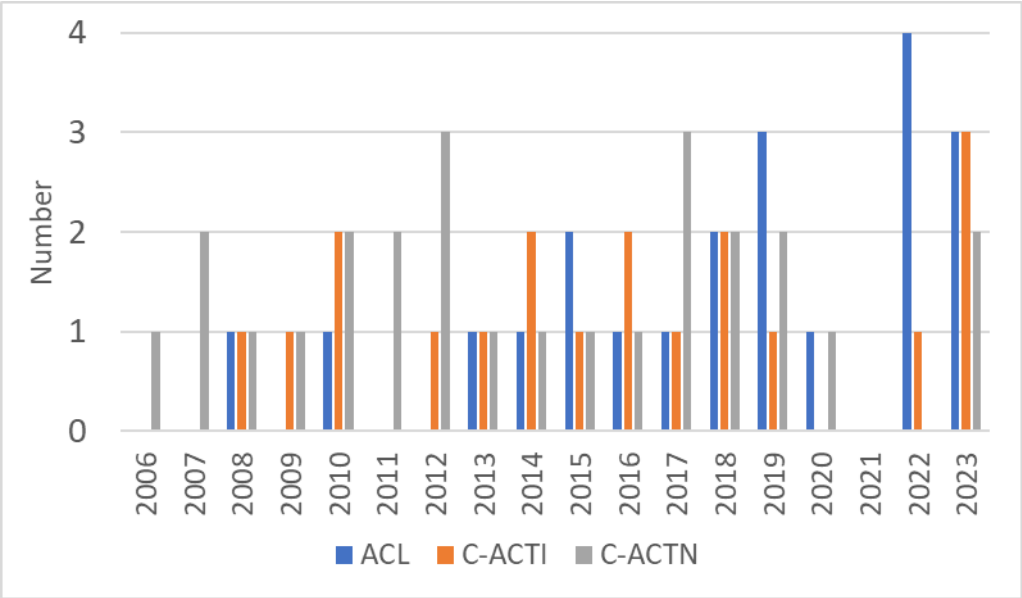

Figure 3.1. Number of publications since 2006.

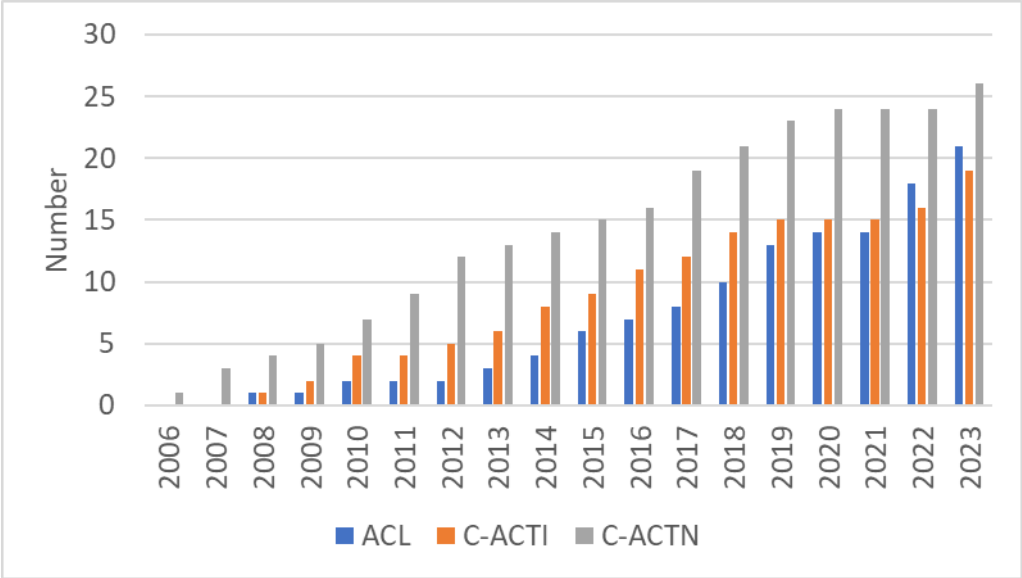

Figure 3.2. Cumulated number of publications since 2006.

Publications in national and international journal with committee of lecture (ACL)

2023 **ACL21** Houssein Jad, et al., *A novel apparatus dedicated to the thermal diffusivity estimation of metals at high temperature*, International Journal of Thermal Science 191 (2023) 108359.

ACL20 Bernard Lamien, Thomas Pierre, H. R. B. Orlande, Philippe Le Masson, Dylan Le Maux, M. Courtois, and Christophe Rodiet, Sequential estimation of high temperatures of liquid metals by using particle filter methods, High Temperatures – High Pressures, Vol. 52, pp 1-23, 2023.

	ACL19	Thomas Pierre et al., *Multiple inversion techniques with multispectral pyrometry for the estimation of temperature and emissivity of liquid niobium and 100c6 steel*, Heat Transfer Engineering, https://doi.org/10.1080/01457632.2023.2241172.
2022	ACL18	Le Maux, Dylan, et al. « Surface Tension of Liquid Fe, Nb and 304L SS and Effect of Drop Mass in Aerodynamic Levitation ». *Journal of Materials Science*, vol. 57, nº 25, juillet 2022, p. 12094-106.
	ACL17	Klapczynski, Vincent, et al. « Temperature and Time Dependence of Manganese Evaporation in Liquid Steels. Multiphysics Modelling and Experimental Confrontation ». *Scripta Materialia*, vol. 221, décembre 2022, p. 114944.
	ACL16	Pierre, Thomas, et al. « Simultaneous Estimation of Temperature and Emissivity of Metals around Their Melting Points by Deterministic and Bayesian Techniques ». *International Journal of Heat and Mass Transfer*, vol. 183, février 2022, p. 122077.
	ACL15	Pierre, Thomas, et al. « In-Plane Thermal Diffusivity Estimation by Radial Fin Method ». *Infrared Physics & Technology*, vol. 120, janvier 2022, p. 103998.
2020	ACL14	Pierre, Thomas, et al. « Transient infrared thermography to characterise thermal properties of millimetre-sized hemp shiv ». *Quantitative InfraRed Thermography Journal*, vol. 17, nº 1, janvier 2020, p. 63-77.
2019	ACL13	Le Maux, Dylan, et al. « Density measurement of liquid 22MnB5 by aerodynamic levitation ». *Review of Scientific Instruments*, vol. 90, nº 7, juillet 2019, p. 074904.
	ACL12	Bernard Lamien, Dylan Le Maux Mickaël Courtois, Thomas Pierre, Muriel Carin, Philippe Le Masson Helcio R. B. Orlande, *A Bayesian Approach for the Simultaneous Estimation of the Thermal Diffusivity and Thermal Conductivity of Aerodynamically Levitated Solid Metals at High Temperatures - Theoretical Study*, International Journal of Heat and Mass Transfer, 141, p. 265-281, 2019.
	ACL11	Thomas Pierre, Muriel Carin, *Apparatus dedicated to the characterization of the thermal properties of millimeter-sized insulating materials*, International Journal of Thermal Science, 135, p. 247-255, 2019.
2018	ACL10	Laurent Dejaeghere, Thomas Pierre, Muriel. Carin, Philippe Le Masson, Mickaël Courtois, *Development and validation of a high temperature inductive furnace dedicated to molten metals characterization*, High Temperatures High Pressure, 2018.
	ACL9	Edouard Geslain, Philippe Rogeon, Thomas Pierre, Cédric Pouvreau, Laurent Cretteur, *Coating effects on contact conditions*, Journal of

		Materials Processing Technology, 253, p. 160-167, 2018.
2017	**ACL8**	Thomas Pierre, Clara Jimenez-Saelices, Bastien Seantier, Yves Grohens, *Transient pulsed technique to characterize the radiative and conductive properties of bio aerogels*, International Journal of Thermal Science, 116, p. 63-72, 2017.
2016	**ACL7**	Pierre, Thomas, et al. « Steady-State and Transient Microscale Temperature Measurements by Multispectral Method and Photons Counting ». *Applied Thermal Engineering*, vol. 99, avril 2016, p. 343-51.
2015	**ACL6**	Thibaut Colinart, Thomas Pierre, *Radiative and hygrothermal properties of spunlaced flax nonwovens*, Journal of Industrial Textiles, p. 1-15, 2015.
	ACL5	Christophe Rodiet, Thomas Pierre, Benjamin Rémy, Alain Degiovanni, *Influence of measurement noise and wavelengths on the temperature measurement of opaque surface with variable emissivity by a multi-spectral method based on the flux ratio in the infrared-ultraviolet range*, High temperatures – High pressures, 44(3), p. 211-226, 2015.
2014	**ACL4**	Thomas Pierre, Thibaut Colinart, Patrick Glouannec, *Measurement of thermal properties of biosourced building materials,* Int J Thermophys (2014) 35:1832–1852.
2013	**ACL3**	Thibaut Colinart, Patrick Glouannec, Thomas Pierre, Philippe Chauvelon, Anthony Magueresse, *Experimental Study on the Hygrothermal Behavior of a Coated Sprayed Hemp Concrete Wall,* Buildings *3*, p. 79-99, 2013.
2010	**ACL2**	Olivier Balima, Thomas Pierre, André Charette, Daniel Marceau, *A least square finite element formulation of the collimated irradiation in frequency domain for optical tomography applications*, Journal of Quantitative Spectroscopy and Radiative Transfer 111 (2010) 280-286.
2008	**ACL1**	Thomas Pierre, Benjamin Rémy, Alain Degiovanni, *Micro-scale temperature by multi-spectral and statistic method in the UV-visible wavelengths*, J. Appl. Phys. 103(3), p. 1-10, 2008.

Invited conferences (C-INV):

2022	**INV1**	Aerodynamic levitation apparatus dedicated to the estimation of physical properties of molten metals, ENCIT2022, Bento Gonçalves, RS, Brazil, November 6th – 10th, 2022.

International communications with proceedings and committee of lecture (ACTI)

2023	**ACTI20**	Luiz F. S. Ferreira, Thomas Pierre, Leonardo A. B. Varon, Helcio R. B. Orlande, *Characterization of thermal properties of mold in petri dishes by laser flash*, ECTP2023, Venice Italy, 10-13 September 2023.
	ACTI19	Jad Houssein, Mickaël Courtois, Thomas Pierre, Gaëtan Le Goïc, Muriel Carin, *A new approach for estimating the thermal diffusivity of molten metals at very high temperature*, ECTP2023, Venice Italy, 10-13 September 2023.
	ACTI18	Dylan Le Maux, Mickael Courtois, Thomas Pierre, Muriel Carin, Philippe Le Masson, *Surface tension measurements of steels by aerodynamic levitation. Influence of the chemical composition*, ECTP2023, Venice Italy, 10-13 September 2023.
	ACTI17	Dylan Le Maux, Mickael Courtois, Thomas Pierre, Muriel Carin, Philippe Le Masson, *Liquid iron viscosity measurements by aerodynamic levitation, both numerical and experimental approaches*, ECTP2023, Venice Italy, 10-13 September 2023.
2022	**ACTI16**	Thomas Pierre, et al., *Multiple inversion techniques with multispectral pyrometry for the temperature and emissivity estimation of liquid niobium and 100c6 steel*, 10th International Conference on Inverse Problems in Engineering ICIPE 2022, Francavilla al Mare, Italy, May 15th – 19th, 2022.
2019	**ACTI15**	Dylan Le Maux, et al., *Density and surface tension measurements on liquid metals by aerodynamic levitation*, ATPC2019 congress, Xian, China, October 2 – 6, 2019.
2018	**ACTI14**	Thomas Pierre, et al., *Transient infrared thermography to characterize thermal properties of millimeter-sized low conductivity materials*, 14th QIRT conference, 25-29 June 2018, Berlin, Germany.
	ACTI13	Édouard Geslain, et al., *Contact temperature measurement by infrared thermography during resistance spot welding process*, 14th QIRT conference, 25-29 June 2018, Berlin, Germany.
2017	**ACTI12**	Thomas Pierre, et al., *Development of a methodology to estimate the thermal diffusivity of solid and liquid metal materials*, 9th International Conference on Inverse Problems in Engineering, May 23-26, 2017, University of Waterloo, Canada.
2016	**ACTI11**	Laurent Dejaeghere, et al., *Inductive high temperatures apparatus dedicated to physical properties characterization of melted metals and alloys*, 11th ATPC 2016, 2 – 6 October 2016, Pacifico Yokohama, Japan.
	ACTI10	Clara Jimenez-Saelices, et al., *Radiative and conductive properties of bio-based aerogels measured by a transient pulsed technique*, 11th ATPC 2016, 2 – 6 October 2016, Pacifico Yokohama, Japan.
2015	**ACTI9**	Édouard Geslain, et al., *Contacts influence on resistance spot weldability of a dissymmetric three-sheets assembly*, 11th International Seminar, Numerical Analysis of Weldability, Graz, Autriche, 27-30 septembre 2015.

2014	**ACTI8**	Laurent Dejaeghre, et al., *Influence of the atmosphere during temperature and emissivity measurements by multispectral method on metallic specimens*, ECTP 2014, 31st August – 4th September 2014, Porto, Portugal.
	ACTI7	Laurent Dejaeghere, et al., *Experimental facility dedicated to high temperatures thermophysical properties measurement: validation of the temperature measurement by multispectral method*, QIRT 2014, 7 – 11 July 2014, Bordeaux, France.
2013	**ACTI6**	Thibaut Colinart, et al., *Hygrothermal behaviour of a hemp concrete wall: comparison between experimental and numerical results*, 13th International Conference of the International Building Performance Simulation Association (BS 2013), Chambery (France), 25-28 août 2013.
2012	**ACTI5**	Thomas Pierre, **et al.**, *Measurement of thermal properties of biosourced materials*, 18th Symposium on Thermal properties, Boulder, CO, USA, 24-29 juin 2012.
2010	**ACTI4**	Thomas Pierre, **et al.**, *A functional approach of the experimental device transfer function for temperature measurements in the UV-visible wavelengths with multispectral method*, Proceedings of the International Heat Transfer Conference IHTC14, august 8 – 13 2010, Whashington, DC, USA.
	ACTI3	Thomas Pierre, et al., *Problématique liée à la mesure de la conductivité thermique d'éco-matériaux du bâtiment*, Actes du 1er Colloque International Francophone d'Énergétique et Mécanique, CIFEM 2010, pp. 434-439, Sénégal, 17-19 mai 2010.
2009	**ACTI2**	Oliver Balima, et al., *A least square finite element formulation of the collimated irradiation in frequency domain for optical tomography applications*, Congrès Eurotherm Seminar Nr 83 15 – 17 avril 2009, Lisbonne, Portugal.
2008	**ACTI1**	Thomas Pierre, et al., *Multi-spectral techniques applied for the measurement of the microscale temperature through cooled multiplier tube in photon counting mode*, Présentation orale au Congrès MNHT2008, 6 – 9 janvier 2008, Tainan, Taiwan.

National communications with proceeding and committee of lecture (ACTN):

2023	**ACTN26**	Luiz F. S. Feirrera, Thomas Pierre, Helcio R. B. Orlande, Parameter estimation during the cooling of mold, Actes du congrès de thermique SFT, Reims, 30 mai – 2 juin 2023
	ACTN25	Dylan Le Maux, et al., *La lévitation aérodynamique dédiée à l'estimation de la viscosité de métaux liquides*, Actes du congrès de thermique SFT, Reims, 30 mai – 2 juin 2023.

2020	**ACTN24**	Dylan Le Maux, et al., *Mesure de tension de surface de métaux à l'état liquide par lévitation aérodynamique*, Actes du congrès de thermique SFT, Belfort, 9 – 12 juin 2020.
2019	**ACTN23**	Édouard Geslain, et al., *Caractérisation des conditions de contact pour le soudage par point*, 24ème congrès de mécanique, Brest, 26 – 30 août 2019.
	ACTN22	Dylan Le Maux, et al., *Mesure de la masse volumique de métaux à l'état liquide par lévitation aérodynamique*, Actes colloque de thermique SFT, Nantes, 3 – 6 juin 2019.
2018	**ACTN21**	Bernard Lamien, et al., *Développement d'un dispositif expérimental pour la caractérisation de métaux autour du point de fusion par lévitation aérodynamique*, Actes colloque de thermique SFT, Pau, 29 mai – 1er juin 2018.
	ACTN20	Édouard Geslain, et al., *Mesure de température de contact lors d'une opération de soudage par point*, Actes colloque de thermique SFT, Pau, 29 mai – 1er juin 2018.
2017	**ACTN19**	Thomas Pierre, et al., *Définition d'une méthodologie pour l'estimation de la diffusivité thermique de métaux solides et liquides par méthode bayésienne*, Actes colloque de thermique SFT, Marseille, 30 mai – 2 juin 2017.
	ACTN18	Édouard Geslain, et al., *Visualisation par thermographie infrarouge du développement de l'échauffement lors du soudage par résistance par point*, Actes du colloque de thermique SFT, Marseille, 30 mai – 2 juin 2017.
	ACTN17	Édouard Geslain, et al., *Caractérisation des résistances de contact électrique entre tôles d'acier revêtues : application au soudage par résistance par point d'un assemblage dissymétrique de 3 tôles*, Actes du colloque de thermique SFT, Marseille, 30 mai – 2 juin 2017.
2016	**ACTN16**	Thomas Pierre, et al., *Développement d'un dispositif expérimental de soudage MIG équipé d'un pyromètre multispectral – Estimation de la température et de l'émissivité autour du bain fondu*, Actes du colloque de thermique SFT, Toulouse, 31 mai – 3 juin 2016.
2015	**ACTN15**	Laurent Dejaeghere, et al., *Influence de l'atmosphère environnante pour des mesures de hautes températures par voie radiative*, Actes du congrès de thermique SFT, La Rochelle, 26 – 29 mai 2015.
2014	**ACTN14**	Laurent Dejaeghere, et al., *Développement d'un banc expérimental dédié à la caractérisation de propriétés thermophysiques de métaux à hautes températures – Validation de la mesure de température par méthode multispectrale*, Actes du congrès de thermique SFT, Lyon, 3 – 6 juin 2014.
2013	**ACTN13**	Thibaut Colinart, et al., *Prise en compte des transferts de masse dans*

		la détermination de la conductivité thermique de matériaux bio-sourcés, Actes du congrès de thermique SFT, Gérardmer, 28 – 31 mai 2013.
2012	ACTN12	Thibaut Colinart, et al., *Étude expérimentale et numérique des caractéristiques thermiques d'une paroi multicouche de béton de chanvre*, Actes du congrès de thermique SFT, Bordeaux, 29 mai – 1 juin 2012.
	ACTN11	Christophe Rodiet, et al., *Optimisation du nombre de longueur d'onde pour la mesure de température par la méthode multispectrale sur des matériaux opaques à émissivité variable dans la gamme Infrarouge-Ultraviolet*, Actes du congrès de thermique SFT, Bordeaux, 29 mai – 1 juin 2012.
	ACTN10	Thibaut Colinart, et al., *Vers une définition de l'état sec d'agro-matériaux à base de chanvre*, XXX^{e} Rencontres de l'AUGC-IBPSA, Chambéry, 6-8 juin 2012.
2011	ACTN9	Thomas Pierre, Thibaut Colinart, *Caractérisation thermo-hydrique d'agro-matériaux à base de chanvre*, Actes du congrès de thermique SFT, Perpignan, 24 – 27 mai 2011, p. 979-984.
	ACTN8	Christophe Rodiet, et al., *Mesure de température par méthode multispectrale*, Actes du congrès de thermique SFT, Perpignan, 24 – 27 mai 2011, p. 495-500.
2010	ACTN7	Christophe Lanos, et al., *Construire et réhabiliter : vers quelles solutions d'isolation ?* colloque Matériaux - Génie civil et habitat du futur, Nantes, Octobre 2010.
	ACTN6	Patrick Glouannec, et al., *Influence de la formulation et du procédé de mise en œuvre sur les propriétés thermique, mécanique et hydrique du béton de chanvre,* colloque Matériaux - Génie civil et habitat du futur, Nantes, Octobre 2010.
2009	ACTN5	Olivier Balima, et al., *Modèle éléments finis de type moindres carrés pour des applications en Tomographie Optique*, Actes du congrès de Thermique SFT, Vannes, 26 – 29 mai 2009, p. 259-264.
2008	ACTN4	Thomas Pierre, et al., *Méthode multi-spectrale avec un réseau de diffraction pour la mesure de la température dans les ultraviolets*, Actes du congrès de thermique SFT, Toulouse, 3 – 6 juin 2008, p. 379-384.
2007	ACTN3	Thomas Pierre, et al., *Mesure de hautes températures par méthode multi-spectrale et statistique dans la gamme UV-visible*, Actes du 4^{e} Colloque Interdisciplinaire en Instrumentation – C2I 2007, Nancy, 17 – 19 octobre 2007, p. 94-103.
	ACTN2	Thomas Pierre, et al., *Mesure de la température à l'échelle microscopique par méthode multi-spectrale et statistique dans la*

gamme UV-visible, Actes du congrès de thermique SFT, Marseille, 29 mai – 1 juin 2007, p. 763-768.

2006	ACTN1	Thomas Pierre, et al., *Métrologie thermique – Mise au point d'un détecteur de température par voie optique à l'échelle microscopique*, Actes du congrès de thermique SFT, Poitiers, 16 – 19 mai 2006, p. 905-910.

Book chapters (OS-C)

2023	OS8	Jean-Claude Krapez, Thomas Pierre, *Measurements without contact in heat transfer: radiation thermometry, Part A: principles, implementation and pitfalls*, METTI 8 Advanced School, Vol. 1, Sept. 24th – Sept. 29th, 2023, Île d'Oléron, France.
	OS7	Thomas Pierre, Philippe Le Masson, Yves Jannot, Andrzej Kusiak, *Thermal characterization by hot-plates*, METTI 8 Advanced School, Vol. 2, Sept. 24th – Sept. 29th, 2023, Île d'Oléron, France.
	OS6	Thomas Pierre, Nicolas Horny, Thierry Duvaut, *Multispectral pyrometry*, METTI 8 Advanced School, Vol. 2, Sept. 24th – Sept. 29th, 2023, Île d'Oléron, France.
	OS5	Philippe Le Masson, Thomas Pierre, *A development of an estimation method of a surface heat flux as a discrete time function*, Vol. 2, METTI 8 Advanced School, Vol. 2, Sept. 24th – Sept. 29th, 2023, Île d'Oléron, France.
2019	OS4	Thomas Pierre, Philippe Le Masson, Yves Jannot, Andrzej Kusiak, *Thermal characterization by hot-plates*, METTI 7 Advanced School, Porquerolles, France, sept. 29th – Oct. 4th 2019.
	OS3	Thomas Pierre, Nicolas Horny, Thierry Duvaut, Christophe Rodiet, *Multispectral pyrometry*, METTI 7 Advanced School, Porquerolles, France, sept. 29th – Oct. 4th 2019.
	OS2	Philippe Le Masson, Thomas Pierre, *A development of an estimation method of a surface heat flux as a discrete time function*, Vol. 2, METTI 7 Advanced School, Porquerolles, France, sept. 29th – Oct. 4th 2019.
2015	OS1	Philippe LE MASSON, Thomas PIERRE, *Tutorial 9: analysis of errors in measurements and inversion*, École METTI6, Biarritz, 1er – 6 mars 2015.

Seminaries, schools and conferences (COM)

2022	COM8	Thomas Pierre, *Aerodynamic levitation apparatus dedicated to the estimation of physical properties of molten metals*, Federal University of Rio de Janeiro, October 14th 2022.
2022	COM7	Edouard Geslain, Thomas Pierre, *Effet de la taille de source sur la*

		mesure de température par thermographie infrarouge à l'échelle microscopique, poster « Work in progress », Société Française de Thermique, Valenciennes, 31 mai – 3 juin 2022.
2019	**COM6**	Philippe Le Masson, Thomas Pierre, *A development of an estimation method of a surface heat flux as a discrete time function*, METTI 7 Advanced School, Porquerolles, France, sept. 29th – Oct. 4th 2019.
2016	**COM5**	Thomas Pierre, et al., *Présentation d'un dispositif hautes températures dédié l'estimation de la diffusivité thermique de métaux à l'état fondu*, Séminaire Matériaux et Fluides à Hautes Températures 2016, Groupe thématique SFT « Hautes Températures », 20 septembre 2016, Paris.
2015	**COM4**	Édouard Geslain, et al., *Observation par caméra thermique du développement de la soudure au sein d'assemblages d'aciers hétérogènes lors du soudage par résistance par point*, CCRS « Soudage par résistance », 2 avril 2015, Villepinte.
	COM3	Édouard Geslain, et al., *Observation par caméra thermique du développement de la soudure au sein d'assemblages d'aciers hétérogènes lors du soudage par résistance par point*, Journée thématique SFT « Transferts aux interfaces », 11 mars 2015, Paris.
2014	**COM2**	Thomas Pierre, et al., *Développement d'un banc à haute température – Mesure de température par pyrométrie multispectrale*, Séminaire Méthodes de mesures et de caractérisation des matériaux à hautes températures, Groupe thématique SFT « Hautes Températures », Paris, 13 février 2014.
2008	**COM1**	Thomas Pierre, *Mesure de la température à l'échelle microscopique dans la gamme ultraviolet-visible*, Les midis du CURAL, Université du Québec à Chicoutimi, Québec, Canada, 19 juin 2008.

Other publications (OP)

2015	**OP2**	Édouard Geslain, et al., *Mise au point d'un dispositif expérimental pour la visualisation par caméra thermique du développement du noyau lors du soudage par résistance par point*, Institut de Soudure, juillet-août 2015, p.39-45.
2008	**OP1**	Thomas PIERRE, et al., *Mesure de hautes températures par méthode multi-spectrale et statistique*, Revue de l'Électricité et de l'Électronique 10, p. 34-39, 2008.

Nomenclature

Latin letters

A	quadrupole coefficient
$\mathcal{A}$	quadrupole coefficient
b	half width, m
B	quadrupole coefficient
$\mathcal{B}$	quadrupole coefficient
Bi	Biot number
C	lightspeed, $m \cdot s^{-1}$
C	specific heat, $J \cdot K^{-1}$
$\mathcal{C}$	quadrupole coefficient
C_1	Planck's law constant, $W \cdot \mu m^4 \cdot m^{-2}$
C_2	Planck's law constant, $\mu m \cdot K$
c_p^m	heat capacity, $J \cdot kg^{-1} \cdot K^{-1}$
D	quadrupole coefficient
$\mathcal{D}$	quadrupole coefficient
e	thickness, m
e	error
E	effusivity, $J \cdot s^{-1/2} \cdot K^{-1} \cdot m^{-2}$
E_λ	energy of a photonic, J
$f(\lambda)$	partial filter spectral transfer function
F	global filter transfer function
Fo	Fourier number
$F_{d1\text{-}2}$	view-factor
h	heat exchange coefficient, $W \cdot K^{-1} \cdot m^{-2}$
h_P	Planck's constant, $J \cdot s$
H	modified Biot number
H	filter amplitude coefficient
I	intensity, $W \cdot sr^{-1} \cdot m^{-2}$
$\mathbf{I}$	identity matrix
I_λ	spectral intensity, $W \cdot \mu m^{-1} \cdot sr^{-1} \cdot m^{-2}$
$I()$	First kind modified Bessel function
J	cost function
$J()$	First kind Bessel function
k_B	Boltzmann's contant, $J \cdot K^{-1}$
k_c	thermal conductivity
k_r	radiative conductivity
$K()$	Second kind modified Bessel function
ℓ	length, m
L	half length, m
$\mathcal{L}^{-1}$	Laplace inverse transform
M	number of time step
n	volume fraction (4.32)
n	refractive index
N	number of wavelengths
$\widetilde{N}$	minimum number of wavelengths
$\mathcal{N}$	norme
φ_λ^0	monochromatic photonic flux density, $ph \cdot s^{-1} \cdot m^{-2}$
$\mathcal{P}_i^{th}$	photonic flux, $ph \cdot s^{-1}$
Q	number of particles
r	radial coordinate
r_c	contact resistance, $m^2 \cdot K^{-1} \cdot W^{-1}$
R	radius, m
RH	relative humidity, %
s	Laplace parameter, s^{-1}
S	water saturation
S_{GS}	Grey scale signal (5.22)
t	time, s

T temperature, °C or K (time domain)
$\mathcal{T}$ transmittance
u eigen value
x Cartesian coordinate
X highspeed camera parameter (5.23)
X sensitivity matrix
y Cartesian coordinate
Y measurement
$Y()$ Second kind Bessel function
$\mathbf{W}$ parameter covariance matrix
z Cartesian coordinate

Greek letters

α thermal diffusivity, $m^2 \cdot s^{-1}$
$\boldsymbol{\beta}$ parameter vector
β parameter
β eigen values in the r-direction, m^{-1}
β_P Planck mean extinction coefficient, m^{-1}
β_R Rosseland mean extinction coefficient, m^{-1}
γ eigenvalue, m-1
$\Delta\#$ # range
δ Dirac function
ε porosity
ε emissivity
ζ constant (4.13)
η quantum efficiency
θ temperature, °C or K (Laplace domain)
θ angle
κ absorptivity (6.2)
λ wavelength, µm
$\pi()$ probability
ρ density, $kg \cdot m^{-3}$
ρ reflectivity
σ Stefan-Boltzmann constant, $W \cdot m^{-2} \cdot K^{-4}$
σ standard deviation, unit of the concerned quantity
τ transmittivity
τ opacity criteria
τ heating time, s
φ heating rate, $W \cdot m^{-2}$ (time domain)
φ azimuth
ϕ constant (4.13)
Φ heating rate, $W \cdot m^{-2}$ (Laplace domain)
Φ radiative flux, W (Section 5)
χ reduced sensitivity
ψ eigenfunction
ω water content, $kg \cdot kg^{-1}$
ω eigenvalue, m^{-1}
$\boldsymbol{\Omega}$ measurement error covariance matrix

Indices & subscripts

0 origin position
0 blackbody
∞ infinity
$\perp$ orthogonal
// parallel
* adimensionned

a	air
a	apparent
a	average (6.33)
b	brass
b	noise
bi	bispectral
c	collimator
cv	convective
e	radial location
eff	effective
exp	experimental
f	filter
h	heating
hs	hot strip
i	wavelength number index
init	initial
j	particle index
k	time index
m	mirror
m	maximum
MAP	maximum *a posteriori*
mono	monospectral
n	eigenvalue index
opt	optimal
rad	radiative
ref	reference
s	solid
s	sample
th	theoretical
x	direction
y	direction
z	direction
w	inner wall
w	water
λ	spectral

4. Characterisation of thermal properties by heating contact techniques

My studies about the characterization of thermal properties started during the ANR project Béton de chanvre (see Section 3.1), which lead to a first publication [Pierre 2014]. The other publications followed on the subject but were the results of personal development [Pierre 2019a][Pierre 2019b][Pierre 2020]. [Pierre 2017] was published during the thesis of Clara Jimenez-Saelices (see Section 3.1). She wanted to know the parts of the conductive and radiative transfers in the aerogels she worked on. So, I developed a specific experimental apparatus to this purpose.

Table 4.1. General information from my published works.

		[Pierre 2014]	[Pierre 2017]	[Pierre 2019a] [Pierre 2020]	[Pierre 2022]	[Pierre 2019b]
Material	Insulating	x	x	x	x	x
	Conducting				x	
Observable	Thermocouple	x	x			x
	Camera			x	x	
Principal flux direction	In-depth	x	x			x
	In-plane			x	x	
Model	Flux-temp.	x				x
	Temp.-temp.		x	x	x	

4.1. Estimation of thermal properties of insulating bio-sourced material with the hot-strip technique and influence of the temperature and humidity [Pierre 2014]

The studies presented in this section constitute a continuity in the setting of experimental protocols dedicated to the characterization of thermal properties of materials heated by Joule effect. Protocols depend on the nature of the material, but should conduct as much as possible to the use of analytical or semi-analytical solutions of the observable over time. Experimentally, the observable is delivered either through the thermoelectric effect (thermocouple) or by radiation (camera, pyrometer).

Table 4.1 details different types of information concerning the nature of the investigated samples, of the observable, the principle direction of the flux, and the type of model. The advantages and the drawbacks of all this information are discussed in each further section, leading to a global reflection of experimental protocol for a given material and using appropriate tools.

4.1.1. Context

This study is dedicated to the thermal characterization of bio-sourced hemp concrete and to propose a predictive thermal conductivity model functions of the temperature and the water content. Mostly used in building, hemp concrete is made from vegetal aggregates such as hemp shives (or hemp hurds) and a lime-binder. With the appropriate proportion of hemp and binder, hemp concrete can cover different uses. Figures 4.1 and 4.2 present focused and tomographic views of hemp concrete.

Figure 4.1 Focused view of a hemp concrete [Pierre 2014] (approximate scale 1:2).

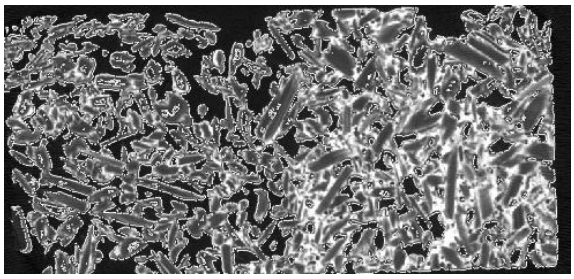

Figure 4.2. Tomographic view of a hemp concrete [Pierre 2014] (approximate scale 1:2).

Hemp concrete has a low bulk density ($300 < \rho < 600$ kg·m^{-3}) and a high porosity ($\varepsilon > 65$ %), and the dry thermal conductivity at ambient temperature is between 0.050 and 0.150 W·m^{-1}·K^{-1}. The knowledge of a single characteristic value may nevertheless not be sufficient to represent the thermal behaviour of the material since temperature and moisture content due to hygroscopic behaviour influence thermal properties during climatic changes: a significant amount of pores is filled with water, which thermal conductivity is 0.600 W·m^{-1}·K^{-1}, while that of air is 0.026 W·m^{-1}·K^{-1}. The consequence of the presence of these three phases (solid matrix, air, and water) and the competition of their effects between them determine the effective thermal properties of the hemp concrete. So, the motivation for determination of the effective thermal conductivity of

such a porous material as a function of temperature and moisture content appears very significant.

The experimental procedure is developed to assess temperature and relative humidity dependence of hemp concrete's thermal properties. The effective thermal conductivity and diffusivity of hemp concrete samples are estimated by *inverse method* and by using a *hot-strip*. The measured values of thermal conductivity are then compared with results from a predictive model based on Krischer's model.

4.1.2. The theoretical model

The hot-strip technique has been used to estimate both thermal conductivity and diffusivity of hemp concrete [Jannot 2004]. It is a 2D transient model developed with the quadrupole formalism. Proposing semi-analytical solution, this formalism is very convenient in case of multilayer problem, including if necessary contact resistance, lumped body assumption, and semi-infinite medium for instance [Maillet 2000].

Considering only the sample, Figure 4.3 presents the sample (in white) and the hot-strip (in grey). There is a symmetrical plane in $x = 0$. The heat transfer is assumed diffusing only in the (x,y) plane. The characteristic dimensions of the sample are its half-width L and its half-thickness e, and for the hot-strip its half-width b.

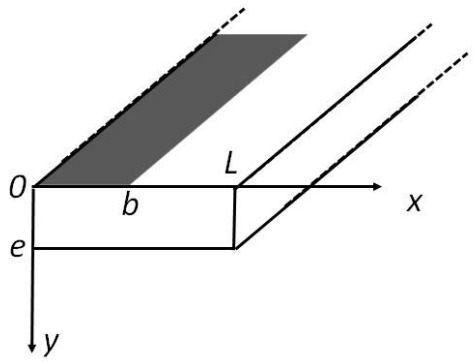

Figure 4.3. Scheme of the sample with the hot-strip.

All physical parameters are assumed isotropic and constant between T_0 and $T_0 + \Delta T$, where T_0 is the initial temperature of the sample and ΔT is the maximum temperature increase during experiment. Neglecting the mass transfers, the sample model is assumed purely conductive:

$$k_x \frac{\partial^2 T}{\partial x^2} + k_y \frac{\partial^2 T}{\partial y^2} = \rho c_p^m \frac{\partial T}{\partial t} \tag{4.1}$$

$$k_x = k_y = k \tag{4.2}$$

$$\alpha = \frac{k}{\rho c_p^m} \tag{4.3}$$

where k is the thermal conductivity, ρc_p^m the heat capacity, and α the thermal diffusivity, and $T = T' - T_\infty$ with T' the absolute temperature of the sample and T_∞ the room temperature. According to Figure 4.3, the initial and boundary conditions are:

$$T(x, y, 0) = 0 \tag{4.4}$$

$$\frac{\partial T(0, y, t)}{\partial x} = 0 \tag{4.5}$$

$$T(L, y, t) = 0 \tag{4.6}$$

$$-k \frac{\partial T(x, 0, t)}{\partial y} = \varphi_0(t) - h_0 T(x, 0, t) \qquad 0 \leq x \leq b \tag{4.7}$$

$$-k \frac{\partial T(x, 0, t)}{\partial y} = h_0 T(x, 0, t) \qquad x > b \tag{4.8}$$

$$T(x, e, t) = 0 \tag{4.9}$$

For both temperature and flux, a double integral transform in space according to the *x*-direction (cosine) and time (Laplace) [Carslaw 1959][Ozisik 2000] leads to:

$$F(\beta_n, y, s) = \int_0^\infty \int_0^\infty f(x, y, t) cos(\beta_n x) e^{-st} dx dt \tag{4.10}$$

where $f(x, y, t)$ is the initial function and $F(\beta_n, y, s)$ its transform, s the Laplace parameter, and X is either L or b, the upper limit of the cosine transform for the temperature and the flux, respectively. Solving Eq. (4.10) allows to get the following heat equation:

$$\frac{d^2\theta}{dy^2} = u_n^2 \theta \tag{4.11}$$

$$u_n^2 = \frac{s}{\alpha} + \beta_n^2 \tag{4.12}$$

where θ is the transformed temperature and β_n are the roots of a transcendental equation obtained with the boundary conditions (4.5) and (4.6). The solution of Eq. (4.11) is:

$$\theta = \phi \, cosh(u_n^2 y) + \zeta \, sinh(u_n^2 y) \tag{4.13}$$

where ϕ and ζ are constants.

Through the *y*-direction, experiment shows that the medium is multi-layered since the heating element, and the contact resistance between the latter and the sample cannot be neglected. Therefore, the quadrupole formalism and solutions of (4.13) allow to express the heat transfer [Maillet 2000] as follows:

$$\begin{bmatrix}\theta_0\\ \Phi_0\end{bmatrix} = \begin{bmatrix}1 & 0\\ C_{hs}s & 1\end{bmatrix}\begin{bmatrix}1 & r_c\\ 0 & 1\end{bmatrix}\begin{bmatrix}A_s & B_s\\ C_s & D_s\end{bmatrix}\begin{bmatrix}\theta_e\\ \Phi_e\end{bmatrix} \tag{4.14}$$

$$\begin{bmatrix}\theta_0\\ \Phi_0\end{bmatrix} = \begin{bmatrix}\mathcal{A} & \mathcal{B}\\ \mathcal{C} & \mathcal{D}\end{bmatrix}\begin{bmatrix}0\\ \Phi_e\end{bmatrix} \tag{4.15}$$

The index for the temperatures and fluxes are for the locations $y = 0$ and e. The first square matrix on the right belongs to the half-hot-strip of heat capacity $C_{hs} = \left(\rho c_p^m e\right)_{hs}$, the second one represents the contact resistance r_c between the hot-strip and the sample, and the third one is the sample where:

$$A_s = cosh(u_n e) \tag{4.16}$$

$$B_s = \frac{sinh(u_n e)}{u_n k} \tag{4.17}$$

$$C_s = u_n k sinh(u_n e) \tag{4.18}$$

$$D_s = A_s \tag{4.19}$$

The solution is at the location $y = 0$:

$$\theta_0 = \Phi_0(s)\frac{tanh(u_n e) + u_n k r_c}{C_{hs}s\ tanh(u_n e) + u_n k(1 + C_{hs}s r_c)} \tag{4.20}$$

From Eq. (4.20), a first inverse integral transform is made:

$$\tilde{T}(x,0,s) = \sum_{n=1}^{\infty}\frac{\psi(\beta_n,x)}{\mathcal{N}(\beta_n)}\theta(\beta_n,0,s) = \sum_{n=1}^{\infty}\frac{2}{L}\theta(\beta_n,0,s)cos(\beta_n x) \tag{4.21}$$

where $\psi(\beta_n, x) = cos(\beta_n x)$ is the eigenfunction and $\mathcal{N}(\beta_n) = L/2$ the norm [Maillet 2000]. Eq. (4.21) determines the temperature at the position (x, $y = 0$) of the hot-strip. Finally, $T(x,0,t)$ is obtained thanks to a numerical inverse Laplace transform [Stehfest 1970a][Stehfest 1970b][De Hoog 1982][Maillet 2000].

4.1.3. The inverse problem: sensitivity analysis and parameter estimation

In Eq. (4.21), the temperature is function of several parameters, those of interest: thermal conductivity and diffusivity, and some due to the experiment: heat density, contact resistance, and heat capacity of the hot-strip.

The sensitivity study focuses only on four parameters: $\boldsymbol{\beta} = [\alpha, k, C_{hs}, r_c]^T$ and the reduced sensitivity is given by:

$$\boldsymbol{\chi}_{\boldsymbol{\beta}} = \boldsymbol{\beta}\frac{\partial \mathbf{T}}{\partial \boldsymbol{\beta}} \tag{4.22}$$

As it has the same unit than the observable, the reduced sensitivity is helpful since the amplitude of the curves (4.22) gives information on the quality of the estimation by comparison with the noise level of the observable (here T). Figure 4.4 presents the evolution of Eq. (4.22) for the four parameters over time. Diffusivity and conductivity are clearly correlated, making their estimation impossible. However, if these parameters are replaced by the effusivity E and the heat capacity ρc_p^m of the sample:

$$\boldsymbol{\beta} = [E, \rho c_p^m, C_{hs}, r_c]^T \tag{4.23}$$

$$E^2 = k\rho c_p^m \tag{4.24}$$

it happens that the two first parameters of vector $\boldsymbol{\beta}$ are not correlated, meaning that they can be estimated as presented in Figure 4.5. Note also that effusivity and heat capacity of the sample behave differently from contact resistance and heat capacity of the hot-strip.

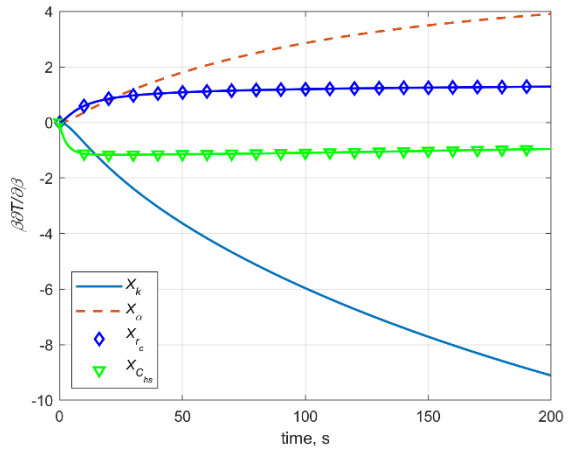

Figure 4.4. Reduced sensitivity of the parameters given by Eq. (4.22).

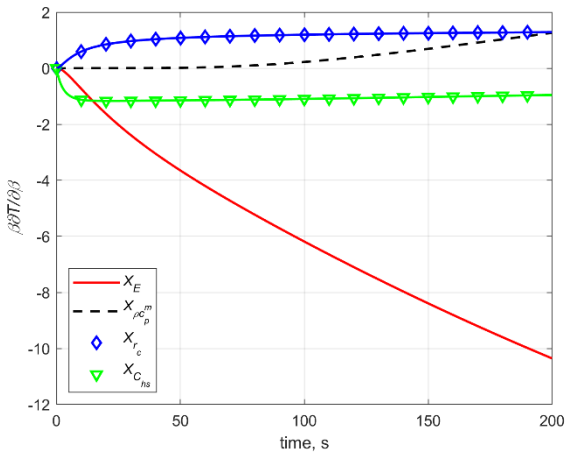

Figure 4.5. Reduced sensitivity of the parameters given by Eq. (4.23).

Parameter estimation is based on the minimization by ordinary least square (OLS) coupled with Levenberg-Marquart (LM) optimization algorithm [Levenberg 1944][Marquardt 1963] of the quadratic error between experimental and theoretical temperatures at location (0,0):

$$J = \sum_{k=1}^{M} \left| T_k^{exp} - T_k^{th}(\boldsymbol{\beta}) \right|^2 \tag{4.25}$$

4.1.4. Experiments, results, and discussion

Two samples are available. The first one with hemp shives oriented in the direction of the heat flux, the second one orthogonally. The influences of relative humidity RH and of temperature T are tested in the ranges [0 % - 95 %] and [-3 °C – 30 °C], respectively.

The sample is equipped of two type K thermocouples, one is located at the front face between the hot-strip and the sample, meaning at the location (0,0) according to Eq. (4.21), and one at the rear face $(0,e)$. Heating is stopped once the temperature at the position $(0,e)$ increases, as it can be seen in Figure 4.6 at $t = 200$ s. Estimation results are presented in Figure 4.7.

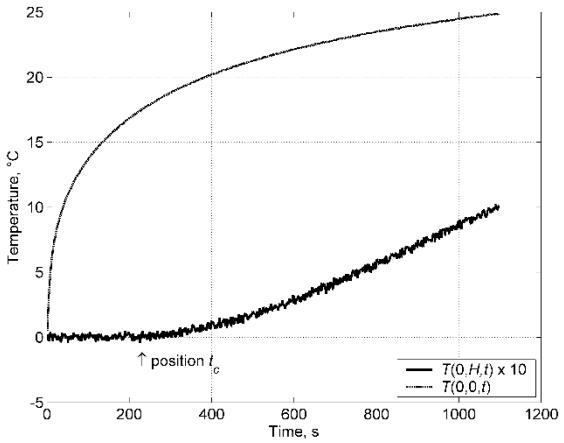

Figure 4.6. Front face and rear face experimental temperatures.

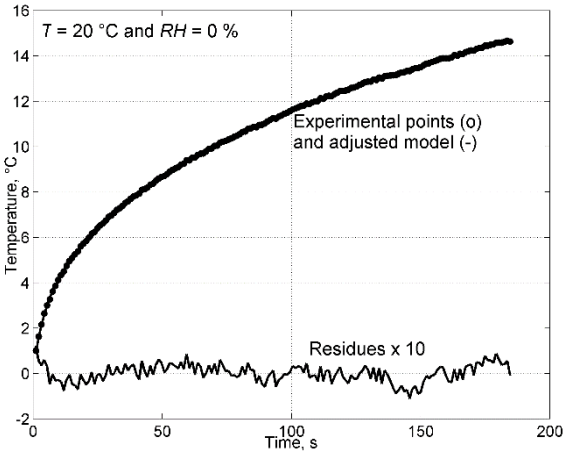

Figure 4.7. Experimental points and adjusted model (4.21) over time and residuals for given room temperature and relative humidity.

Figure 4.8 shows estimation of heat capacity ρc_p^m, which varies linearly with water content w and approached by an additive model:

$$\rho c_p^m = \rho_{dry}\left(c_{p,dry}^m + w c_{p,w}^m\right) \tag{4.26}$$

where $\rho_{dry} c_{p,dry}^m$ is the specific heat of dry hemp concrete and $c_{p,w}^m$ is the water specific heat [Incropera 2011]. In Figure (4.9) the conductivity estimation is presented versus relative humidity and temperature for both samples.

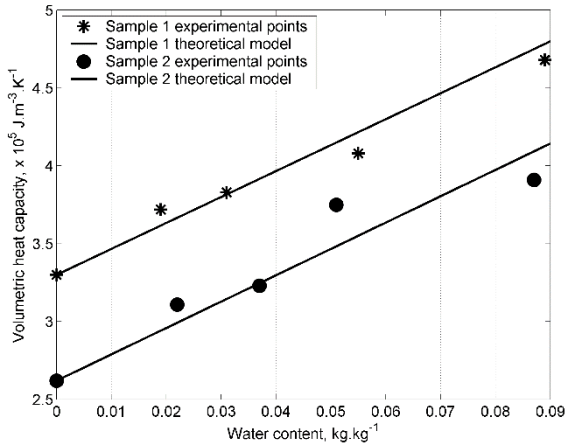

Figure 4.8. Heat capacity versus water content for both samples and comparison with theoretical model.

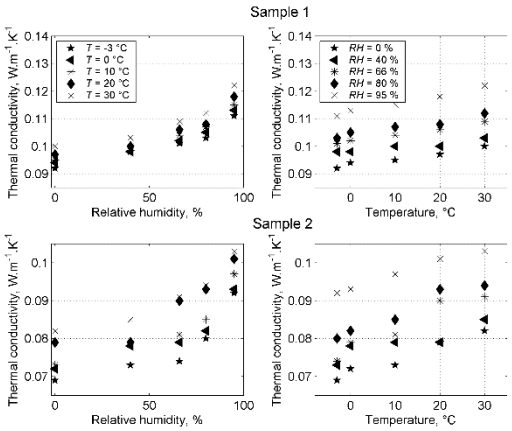

Figure 4.9. Conductivity versus relative humidity (on the left) and temperature for both samples.

Since experimental measurements of thermal properties as a function of temperature and relative humidity are very time consuming, development and application of predictive models are the most convenient method. In literature, many works present prediction of effective thermal conductivity of porous media as a function of the phase number (solid, liquid, gaseous), the porosity, the orientation, and the shape of the pores [Wang 2008]. In our case, Krischer [Krischer 1963] proposed a weighted harmonic mean of series and parallel models (4.27)-(4.31). This model has been adapted over temperature T and water content w variations (4.32).

$$k_{eff} = \frac{1}{\frac{1-n}{k_{\parallel}} + \frac{n}{k_{\perp}}} \tag{4.27}$$

$$k_{\parallel} = (1-\varepsilon)k_s + \varepsilon(1-S)k_a + \varepsilon S k_w \tag{4.28}$$

$$k_{\perp} = \frac{1}{\frac{1-\varepsilon}{k_s} + \varepsilon\left(\frac{1-S}{k_a} + \frac{S}{k_w}\right)} \tag{4.29}$$

$$S = \frac{\rho_{eff}}{\rho_w}\frac{w}{\varepsilon} \tag{4.30}$$

$$\frac{w}{w_0} = \frac{C\ K\ RH}{(1-K\ RH)(1-K\ RH-C\ K\ RH)} \tag{4.31}$$

$$k_{eff}(T,w)=\left\{\frac{n-1}{(1-\varepsilon)k_s(T)+\varepsilon\left[1-\frac{\rho_{dry}(1+w)}{\rho_w(T)}\frac{w}{\varepsilon}\right]k_a(T)+\frac{\rho_{dry}(1+w)}{\rho_w(T)}wk_w(T)}+\frac{n}{\frac{1-\varepsilon}{k_s(T)}+\frac{\varepsilon\left[1-\frac{\rho_{dry}(1+w)}{\rho_w(T)}\frac{w}{\varepsilon}\right]}{k_a(T)}+\frac{\frac{\rho_{dry}(1+w)}{\rho_w(T)}w}{k_w(T)}}\right\}^{-1} \quad (4.32)$$

- Quantities k_s, k_w and k_a are the thermal conductivity of solid phase, moisture and dry air, respectively. Thermal conductivities of air and water are well-known [Sacadura 2000] and their use with temperature is under polynomial forms in the working temperature range.
- Weighting parameter n ranges between 0 and 1. It is a common practice that n is the volume fraction of the medium disposed orthogonally to the heat flux direction.
- Air volumetric fraction in a dry porous material is given by the total porosity ε ($0 \leq \varepsilon \leq 1$). In the case of penetration of liquid water, the filled part of the porous space is given by water saturation S ($0 \leq S \leq 1$).
- Water saturation S in Eqs. (4.28) and (4.29) is given by Eq. (4.30).
- Water content w is expressed by Eq. (4.31) over the entire relative humidity RH range by fitting Guggenheim-Anderson-de Boer model (GAB) [Guggenheim 1966] to experimental data: $w_0 = 0.0143$ kg·kg^{-1}, $C = 14.164$ and $K = 0.877$. These parameters have been estimated by least-squares by minimizing the quadratic error between experimental water content and w from Eq. (4.31).

In Eq. (4.32), the unknown parameters are n, ε, and k_s(T). First, they have been estimated using OLS with LM algorithm by minimizing quadratic error between experimental conductivities k and k_{eff} at dry state ($S = 0$). Then a global polynomial for k_s(T) is deduced.

Figures 4.10 and 4.11 present predicted conductivities of both hemp concrete samples as a function of moisture content w and experimental points. Thermal conductivity calculations have been done for a water content supposed constant between -3 °C and 30 °C, since the experimental apparatus does not allow measurement of the mass evolution during experiments. However, a 0.6 % mass variation has been observed before and after experiments, which leads to a water content variation of 8 %. In parallel, error on thermal conductivity can be approached as the sum of the errors on temperature measurement (experimental noise of about 0.05 °C), on hot-strip dimensions (systematic

error of 0.1 %) and on flux (errors of 0.5 %). As a consequence, error on thermal conductivity is estimated at 3 %.

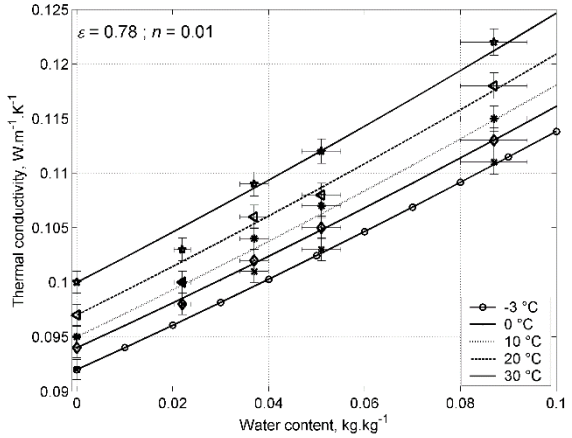

Figure 4.10. Krischer's model adjustment on experimental thermal conductivities versus water content for sample 1.

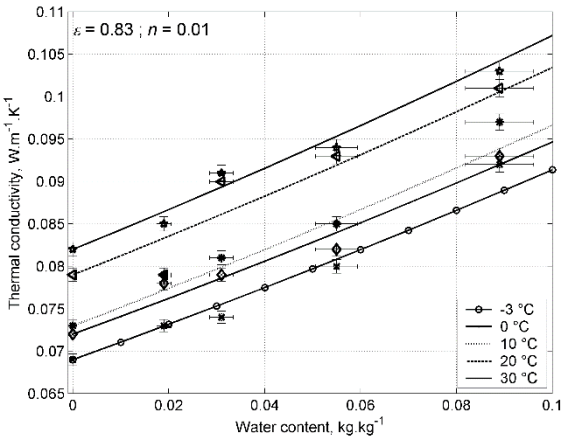

Figure 4.11. Krischer's model adjustment on experimental thermal conductivities versus water content for sample 2.

4.1.5. Conclusion

This study dealt with the estimation of a predictive model of thermal conductivity of a three phases hemp concrete for given temperature and water content based on Krischer's effective conductivity model. The parameters of the predictive model have been estimated by inverse method by minimization with ordinary least squares experimental effective conductivity, which has also been estimated by inverse method using hot-strip technique between theoretical and experimental temperatures at location (0,0). Sensitivity analysis allowed to observe that simultaneous estimation of thermal conductivity and effusivity is possible, making possible the determination of diffusivity and heat capacity. Comparison shows a good agreement between predicted and experimental values and offers interesting outlook.

The use of hot-strip technique is easy to set, but it presents several drawbacks, and particularly with this type of heterogeneous porous material. The presence of instrumentation penalizes systematically the measurements. As mentioned previously, there are unknown parameters appearing in the theoretical expression of the temperature: the hot-strip heat capacity, the contact resistance between the hot-strip and the sample. I could also mention the presence of the thermocouple and the heat rate.

- The *Heat capacity* of the hot-strip is difficult to estimate due to its own heterogeneity. Possibilities to estimate heat capacity of heating element exist but seem much appropriate with square as for hot-plane technique, with the use of semi-infinite models [Jannot 2018][Pierre 2019b].
- The problem with the *contact resistance* is that it is systematically correlated with the sample thermal conductivity. However, for insulating material, which is the case in this study, contact resistance can be neglected if the sample thickness is large enough. Of course, the innocuousness of the contact resistance depends on the thickness of the sample and of its nature (from insulating to conductive).
- The presence of *thermocouple* between the sample and the hot-strip can result in irregular and large value of contact resistance if the sample does not possess a certain flexibility, like rubber. With heterogeneous porous material, punctual measurement with a thermocouple is an issue, since the tip can be either in contact with the solid phase, or with a pore: measurement is rather local than representative of global surface of the sample, this issue is also encountered during measurements with the hot-wire technique [Sjöström 2014][Seng 2019].
- Finally, there is also an uncertainty on the *heat rate* delivered by the hot-strip. The heat dissipation along wires becomes negligible with increasing the surface of the hot-strip. But it remains an uncertainty of the *contact surface* with the sample. The real contact surface is not systematically the hot-strip surface, it can be smaller. A procedure of estimation of real contact surface is proposed in [Jannot 2018] with the help of a well-known material. But it may be questioned if this calibrated real surface is the same with another material, assuming that the pressure applied to maintain the whole experiment is controlled.

Parameter estimation with hot-strip technique is a practical manner to characterize homogeneous insulating materials preferentially with very weak apparent surface porosity, at least with a porosity weaker than the thermocouple dimensions. Characterization of more complex materials such as hemp concrete is also possible but with a global view with the estimation of effective parameters. The control of rear face temperature allows to use semi-infinite or imposed temperature assumptions, and thus to not consider its heat losses. Among all unknown parameters that affect the estimation of those of interest, the main uncertainties come from the knowledge of the heat capacity of the heating element and the heat rate due to the surface contact.

The calculation time with the use of this analytical model for the parameter estimation through OLS with LM is of several tens of seconds. This analytical model is very convenient in our case since we have considered an effective view of the material, meaning a global approach but representative of the material in use. A more accurate study of the material would imply in most of the case the use of multiphysics numerical models and thus a non-negligible increase of the calculation time [Niezgoda 2012b][Nguyen 2016][Bourdot 2017] [Bennai 2018].

To avoid influence of the heat capacity and of the heat rate, an appropriate manner is the use of temperature-temperature model. The model presented in Eq. (4.21) is a flux-temperature model, meaning that input is the heat rate and observable is the temperature. In this case, the transfer function is called impedance. In the case of temperature-temperature model, it is a transmittance. It can be adapted with the hot-strip technique, and we propose to present it in the next sections dedicated to the characterization of conductive and radiative properties of bio-aerogels in Section 4.2 and of various insulating and conductive materials in Sections 4.3 and 4.4, and of high temperature metals in Section 6.

4.2. Estimation of the conductive and radiative properties of bio-aerogel with a transient pulsed technique [Pierre 2017]

4.2.1. Context

This study presents thermal characterization by inverse method of a bio-aerogel with the use of apparatus based on a pulsed technique and a simple theoretical 1D model. Parameters of interest are solid and gas thermal conductivity, radiative effect through a radiative conductivity, and thermal diffusivity.

Aerogels consist of highly porous materials with very low density and large specific surface. Aerogels' low thermal conductivity at ambient atmospheric pressure makes them good candidate of nanoporous heat insulation materials. Currently, usual techniques, such as conductometer [Nguyen 2014], guarded hot-plate [Shi 2013], hot-disk [Grishechko 2013], hot-wire [Rudaz 2014], allow assessing only an effective thermal conductivity. Nevertheless, even if convection is neglected due to the small diameter of pores, gas conduction and radiation occur in addition to solid conduction in aerogel [Ebert 2011][Cuce 2014]. Experimentally, the greatest difficulty is to evaluate the contribution

of each heat mechanism. Regarding the macroscopic approach, radiative flux that reaches a material surface can be reflected, absorbed, or transmitted along the thickness of the material [Incropera 2011][Xie 2013]. As aerogel is capable of absorbing, emitting, and scattering thermal radiation [Wei 2013], heat transfers in it are described by solving combined conductive (Fourier's law) and radiative transfer equations [Ozisik 1973]. Combined calculation of radiation and conduction heat transfer has been extensively studied through more or less sophisticated numerical models [Kunc 1984][Ping 1989][André 1995][Zeng 1995a][Zeng 1995b][Heinemann 1996][Asllanaj 2007][Niezgoda 2011][Chandrasekar 2013]. Maillet *et al.* [Maillet 2000] propose approximate analytical solutions for this problem assuming monodimensionnal heat transfer and azimuthal symmetry. Solutions are proposed in the cases of purely emitting/absorbing media, purely scattering media, and both emitting/absorbing and scattering participating media. In every case, radiative boundary conditions suppose opaque, scattering, absorbing emitting, and reflecting surfaces.

4.2.2. Theoretical model and sensitivity study for the definition of the experiment

A simple theoretical model is proposed based on combination of several studies. First of all, the quadrupole formalism is used to solve conductive-radiative coupling within aerogel [Maillet 2000][Degiovanni 2002][Rémy 2006]. The aerogel thickness is large enough to be opaque. It is assumed that boundaries are opaque too and their effects negligible. In this case, radiative transfer is viewed like a pure diffusion process and can be modelled by a simple thermal resistance $R_r = e/k_r$ [Degiovanni 2002] (Figure 4.14 and Rosseland's model [Ozisik 1973]). Second of all, Jannot *et al.* [Jannot 2009] developed an apparatus dedicated to thermal characterization of opaque insulating material. This is a pulsed transient technique, where the sample is heated on its front face thanks to heating resistance and where two brass plates are placed on both front and rear faces of the sample. We have adapted this technique in our case with only one brass plate on the rear face of the sample (Figures 4.12 and 4.13). Moreover, the following assumptions and considerations are proposed:

- The contact resistances between the heating element and the aerogel and between the aerogel and the brass are not taken into account.
- The brass plate is assumed purely capacitive (C_b in Eq. (4.33)) and not resistive.
- The heat capacity of the heating element is not taken into account.

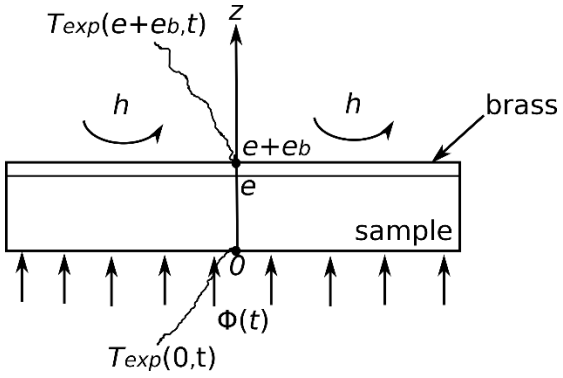

Figure 4.12. Diagram of the experimental set-up.

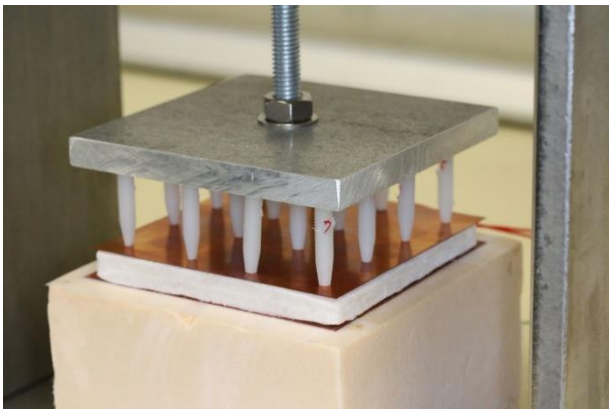

Figure 4.13. Picture of the experimental set-up. Dimensions of the aerogel sample (in white): $e = 9$ mm and $S = 80 \times 80$ mm^2.

Consequently, 1D quadrupole approach leads to express the whole system as follows and presented in Figure 4.14:

$$\begin{bmatrix}\theta_0\\ \Phi_0\end{bmatrix} = \begin{bmatrix}A_{rc} & B_{rc}\\ C_{rc} & D_{rc}\end{bmatrix}\begin{bmatrix}1 & 0\\ C_b s & 1\end{bmatrix}\begin{bmatrix}\theta_{e+e_b}\\ \Phi_{e+e_b}\end{bmatrix} = \begin{bmatrix}\mathcal{A} & \mathcal{B}\\ \mathcal{C} & \mathcal{D}\end{bmatrix}\begin{bmatrix}\theta_{e+e_b}\\ \Phi_{e+e_b}\end{bmatrix} \tag{4.33}$$

$\theta_0 = \theta(0,s)$ and $\theta_{e+eb} = \theta(e+e_b,s)$ correspond, in the Laplace domain, to theoretical temperatures at positions $z = 0$ and $z = e+e_b$, where experimental temperatures are measured. The first square matrix is the conductive-radiative matrix M_{rc} and the second one is the purely capacitive matrix of the brass plate. The terms of the conductive-radiative matrix are the followings (details in Appendix A in [Pierre 2017]):

$$A_{rc} = \frac{A_c R_r + B_c}{B_c + R_r} \tag{4.34}$$

$$B_{rc} = \frac{B_c R_r}{B_c + R_r} \tag{4.35}$$

$$C_{rc} = -\left(\frac{1}{B_c} + \frac{1}{R_r}\right) + \left(\frac{D_c}{B_c} + \frac{1}{R_r}\right)\frac{A_c R_r + B_c}{B_c + R_r} \tag{4.36}$$

$$D_{rc} = \frac{D_c R_r + B_c}{B_c + R_r} \tag{4.37}$$

$$A_c = cosh(qe) \tag{4.38}$$

$$B_c = \frac{sinh(qe)}{k_c q} \tag{4.39}$$

$$C_c = k_c q\ sinh(qe) \tag{4.40}$$

$$D_c = A_c \tag{4.41}$$

$$q^2 = s/\alpha \tag{4.42}$$

$$\alpha = \frac{k_c}{\rho c_p^m} \tag{4.43}$$

where s is the Laplace parameter, $R_r = e/k_r$ is the radiative resistance, k_r is the radiative conductivity, e is the sample thickness, α is the phonic thermal diffusivity [André 1995], k_c the thermal conductivity, and ρc_p^m the thermal capacity of the sample.

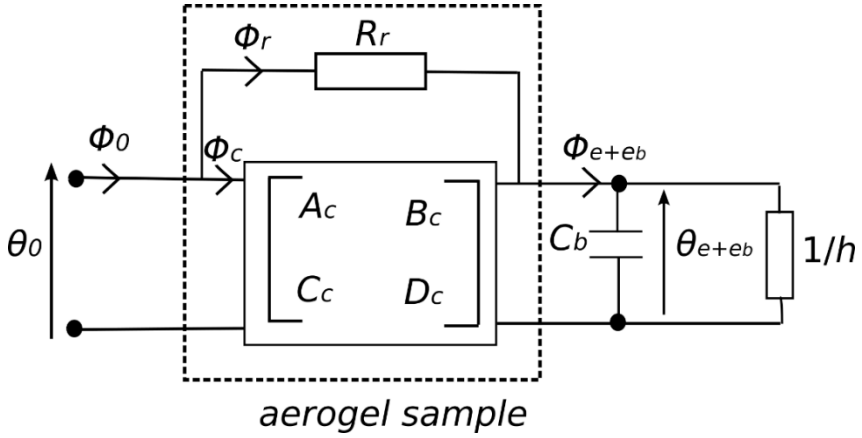

Fig. 4.14. Quadrupole network of the experimentation.

The boundary condition at $z = e+e_b$ is:

$$\Phi_{e+e_b} = h\theta_{e+e_b} \tag{4.44}$$

where h is the heat transfer coefficient between the brass plate and the air. Jannot *et al.* [Jannot 2009] proposed an approach based on the expression of the transfer function $\mathcal{T}(s)$ between temperature expressions at positions 0 and $e+e_b$:

$$\mathcal{T}(s) = \frac{\theta_{e+e_b}(s)}{\theta_0(s)} = \frac{1}{\mathcal{A} + h\mathcal{B}} \tag{4.45}$$

This theoretical expression is used here to estimate experimental temperature $T^{exp}(e+e_b,t)$ versus experimental temperature $T^{exp}(0,t)$:

$$T^{exp}(e+e_b,t) = T^{exp}(0,t) \otimes \mathcal{L}^{-1}[\mathcal{T}(s)] \tag{4.46}$$

Beforehand, Figure 4.15 compares theoretical 1D models based on Eq. (4.33) and 3D models based on [Jannot 2010] expressing front and rear faces temperatures. Dimensions and thermophysical properties values are the following:

- Brass plate: $e_b = 0.15$ mm, $C_b = 3.44 \times 10^6$ J·m^{-3}·K^{-1};
- Aerogel: $e = 9$ mm, $k_c = 20$ mW·m^{-1}·K^{-1}, $k_r = 20$ mW·m^{-1}·K^{-1}, $\alpha = 1.33$ mm^2·s^{-1};

- Heat transfer coefficient: $h = 10$ W·m^{-2}·K^{-1}.

Both models present the same thermograms during more than 200 s (only the first 100 s are plotted here) with mean residuals less than 10^{-3} °C, which means that 1D model is enough for this study. The flux density Φ_0 is also plotted. The Laplace numerical inversion, which allows to perform $\Phi_0(t) = \mathcal{L}^{-1}[\Phi_0(s)]$ used here [De Hoog 1970] gives satisfying results.

The plot of $T^{th}(e+e_b,t)$ in Figure 4.16 is proposed for different values of radiative conductivity k_r between 0 and 20 mW·m^{-1}·K^{-1}. It is obvious that radiative transfer induces sudden temperature increase proportional with k_r. We can also observe a transition break in early time, representing a transition between radiative and conductive effects [Maillet 2000][André 1995].

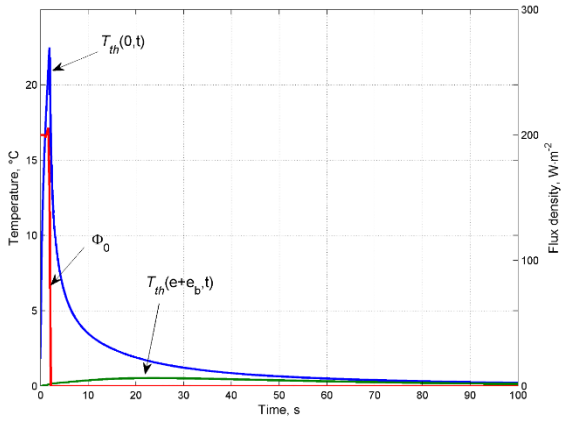

Fig. 4.15. Theoretical 1D and 3D front and rear faces temperatures calculated from equations (4.34) to (4.43) and flux density Φ_0.

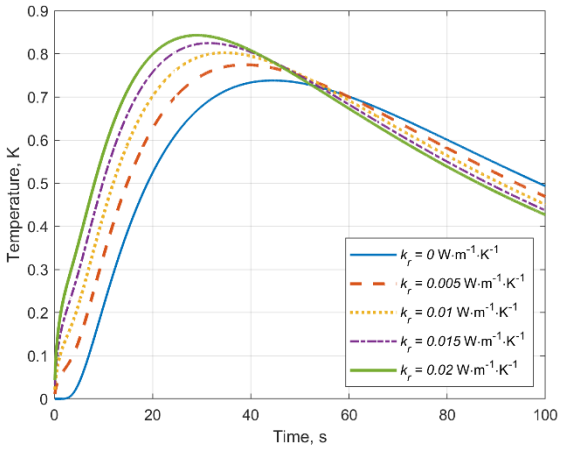

Fig. 4.16. Rear face theoretical temperature $T^{th}(e+e_b,t)$ for different values of radiative conductivity k_r.

Four parameters are unknown in the transfer function $H(s)$ in Eq. (4.45): the thermal diffusivity α, the thermal conductivity k_c, the radiative conductivity k_r, and the heat transfer coefficient h. These four parameters are estimated by inverse method, minimizing the sum of the quadratic difference between experimental values $T^{exp}(e+e_b,t)$ with those calculated by relation (4.46) with experimental value $T^{exp}(0,t)$. The minimization is realized by using LM method.

Now sensitivity study is presented in Figure 4.17:

- All sensitivity curves have equivalent amplitudes and present possibility to estimate the four parameters independently.
- The thermal diffusivity seems to be estimated properly even if a non-negligible correlation exists with the radiative conductivity.
- The principal parameter correlated with the thermal conductivity seems to be the radiative conductivity.
- The presence of the brass plate on the rear face decorrelates the conductivities and the heat transfer coefficient, which is not possible without it [Degiovanni 1977]. Indeed, due to its capacitive properties, the brass delays the development of the convective effects at the rear face.
- Direct contact between the heating element and the sample makes possible decorrelation between radiative and thermal conductivities. Radiative effects being quicker than conductive effects, temperature is at first sensitive to radiative effect.

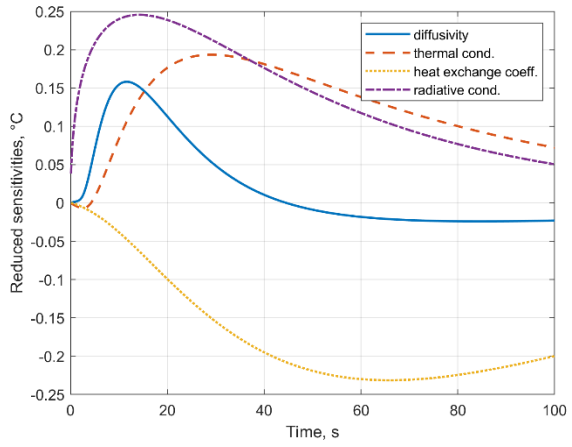

Figure 4.17. Reduced sensitivities of the transmittance function $\mathcal{L}^{-1}[H(s)]$ over time.

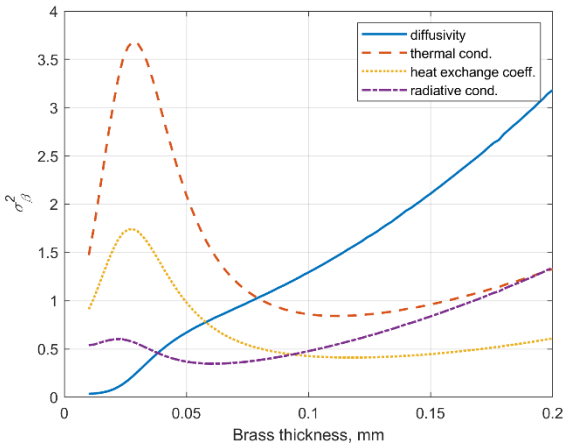

Figure 4.18. Evolution of the variance of each parameter function of the thickness of the brass plate.

A series of simulations have been performed to define the optimal thickness of the brass plate, between 10 µm and 200 µm, considering the thickness (9 mm) of aerogel samples. Experimental measurements have been simulated with addition of a null-average normal noise σ_b of 0.1 °C to $T^{exp}(0,t)$. Figure 4.18 presents the evolution of the variances (4.47) for each parameter estimations [Orlande 2011].

$$var(\boldsymbol{\beta}) = \sigma_{\boldsymbol{\beta}}^2 = \sigma_b^2 \left(X_{\boldsymbol{\beta}}^T X_{\boldsymbol{\beta}}\right)^{-1} \tag{4.47}$$

Except for the variance $var(\alpha)$, every curve present a minimum variance between 50 µm ($var(k_r)$) and 150 µm approximately ($var(h)$ and $var(k_c)$). Experimentally, the brass plate has been chosen with a thickness of 150 µm in order to be not too flexible.

4.2.3. Results and discussions

Experimental apparatus is presented in Figures 4.12 and 4.13. Aerogel sample is placed between a heating element and a brass plate. Initially at $z = 0$, the heating element delivers a thermal flux $\varphi(t)$ during a time step τ. The pressure, which is not controlled, of the brass plate on the top is assured by several punctual PVC tips with a very low contact area. As aerogel is a very fragile material, the two type K thermocouples, which measure experimental temperatures $T^{\exp}(0,t)$ and $T^{\exp}(e + e_b,t)$, are placed upward the heating element and on the upper face of the brass plate. Thermocouples characteristics are the following: 125 µm of diameter for the wire and 300 µm for the tip of the probe. Integration time dt is set at 100 ms (limitation of the temperature recorder).

Figure 4.19 plots the fitting of Eq. (4.46) on experimental rear face temperature with and without radiative transfers. Figure 4.20 shows that the reduced sensitivities X_α of thermal diffusivity seems weakly correlated with other parameters, but its amplitude is weaker. Both models (with and without radiative transfers) give satisfying fittings and close results of estimation as reported in Table 4.2 in terms of thermal conductivity. The sum of both thermal and radiative conductivities is 20 % lower than conductivity estimated with the model without radiation. Heat exchange coefficients are also approximately the same and consistent with typical values for natural convection. However, estimation of thermal diffusivity gives a value 4 times higher without the radiative component in the model. This has already been observed and discussed in [Hahn 1997] [Niezgoda 2012a]. Table 4.2 presents all results obtained by estimation and comparison with measurements with other techniques. It shows that, with the radiative component, estimated thermal diffusivity and thermal conductivity lead to a value of heat capacity in accordance with the one obtained with calorimetry.

Table 4.2. Values of estimated parameter with and without radiation.

	α, mm·s^{-1}	k_c, mW·m^{-1}·K^{-1}	k_r, mW·m^{-1}·K^{-1}	h, W·m^{-1}·K^{-1}
with k_r	1.12	15.1	14.2	8.8
without k_r	4.55	36.5	-	11.0

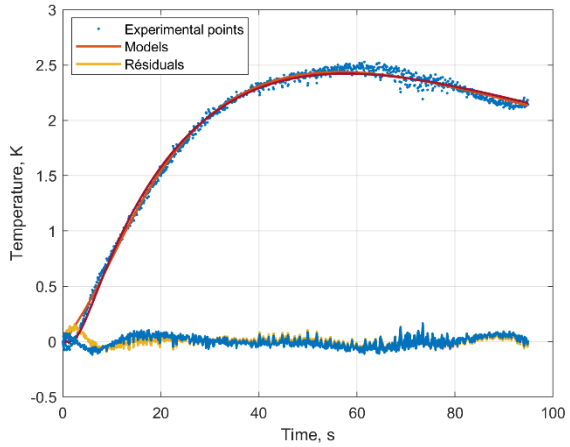

Figure 4.19. Experimental and fitted theoretical rear face temperatures with and without radiation.

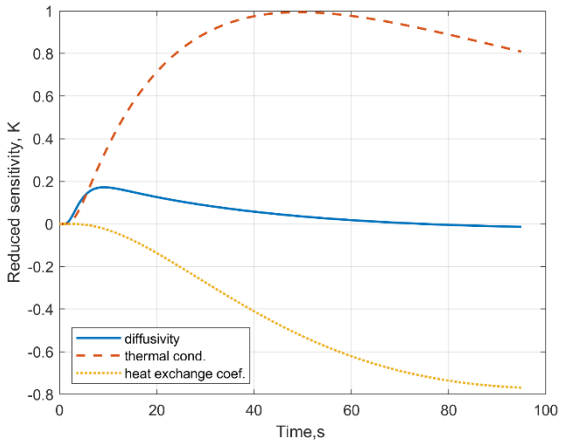

Figure 4.20. Reduced sensitivity considering three parameters: diffusivity, thermal conductivity and heat exchange coefficient.

Table 4.3. Experimental results of thermal properties of aerogels.

	apparatus of this study	guarded hot plate	hot plate	calorimeter
α (mm·s^{-1})	1.12 ± 0.13			
k_c (mW·m^{-1}·K^{-1})	15.1 ± 1.0			
k_r (mW·m^{-1}·K^{-1})	14.2 ± 2.1			
k_{eff} (mW·m^{-1}·K^{-1})	29.3 ± 3.0	36.2 ± 0.3	32.1 ± 0.5	
h (W·m^{-2}·K^{-1})	8.8 ± 1.5			
C_s (kJ·m^{-3}·K^{-1})	13.5 ± 1.0			17.4 ± 1.5
c_p^m (J·kg^{-1}·K^{-1})				$1\,500 \pm 100$

As it was briefly mentioned, Figure 4.21 presents experimental rear face temperatures versus time. A slight slope change is observable, probably due to transition

between radiative and conductive effects, and has been correctly fitted by theoretical curve, and already observed in previous studies [André 1995][Niezgoda 2011].

A final point concerns the comparison between estimated experimental value of the radiative conductivity k_r and theoretical expression of the Rosseland approximation k_r^{th} (4.49) where $\sigma = 5.67 \times 10^{-8}$ W·m^{-2}·K^{-4} is the Stefan-Boltzmann constant. This expression allows to give an estimation of a mean extinction coefficient β, which can be defined according to Eqs. (4.49) and (4.50) representing, respectively, β_R and β_P Rosseland's and the Planck's mean extinction coefficients [Ozisik 1973]. Experimentally, as aerogel scatters the heat flux and is not mainly absorbing, this is an effective mean extinction coefficient $\beta_{\lambda eff}$, which has been measured with a spectroradiometer working between $\lambda_1 = 2$ µm and $\lambda_2 = 25$ µm for a sample of 4 mm of thickness. Spectral normal direct transmittivity has been measured at first (4.51), then Rosseland's and Planck's mean extinction coefficients (Figure 4.22) have been compared with values found in the literature. From Eqs. (4.49) and (4.50) and experimental data, calculations of β_R and β_P give 591 m^{-1} and 664 m^{-1}, respectively. These approximated values are satisfying since they can be compared with the mean extinction coefficient obtained from estimation of radiative conductivity (4.48): $\beta = 660$ m^{-1} for a temperature of $T = 310$ K, which is the mean temperature of the sample during experiments. In every case, opacity criterion $\tau = \beta e > 5$ is fulfilled, supporting *a posteriori* the assumptions taken. Literature mentions also a specific spectral extinction coefficient K_λ expressed in m^2·kg^{-1}, that is to say β/ρ, with ρ the density. In our case, K_λ is equal to 44 m^2·kg^{-1}, which is in good agreement with specific spectral extinction coefficient of aerogel found in literature [Wei 2011][Wei 2013].

$$k_r^{th} = \frac{16}{3} n^2 \sigma \frac{T^3}{\beta} \tag{4.48}$$

$$\frac{1}{\beta_R} = \frac{\int_{\Delta\lambda} \frac{1}{\beta_{\lambda,eff}} \frac{dL^0(T)}{dT} d\lambda}{\int_0^\infty \frac{dL^0(T)}{dT} d\lambda} \tag{4.49}$$

$$\frac{1}{\beta_P} = \frac{\int_{\Delta\lambda} \beta_{\lambda,eff} L^0(T) d\lambda}{\int_0^\infty L^0(T) d\lambda} \tag{4.50}$$

$$\tau_\lambda^\perp = \frac{I_\lambda}{I_\lambda^0} = e^{-\beta_{\lambda,eff}\, e} \tag{4.51}$$

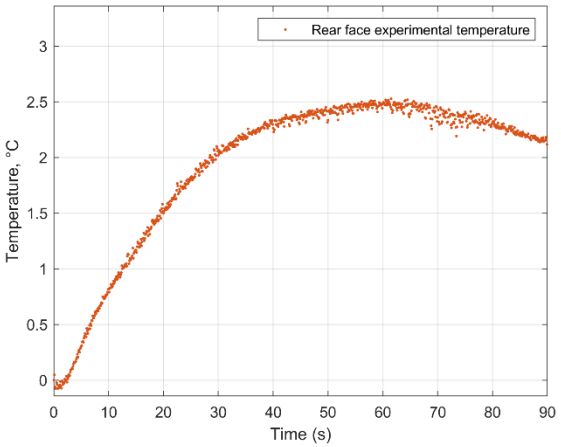

Figure 4.21. Experimental points: observation of a break between radiative and conduction heat transfers around 8 s.

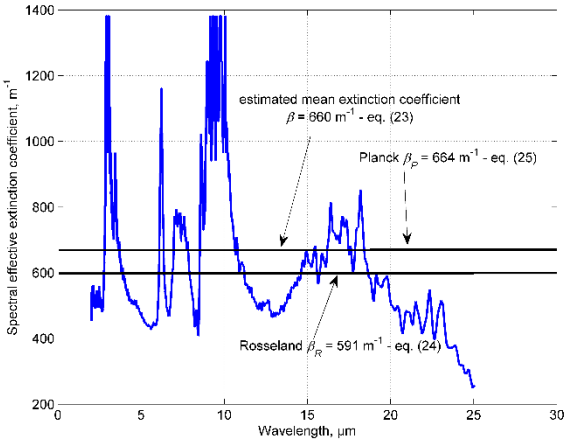

Figure 4.22. Spectral effective, Planck's and Rosseland's mean extinction coefficients of the aerogel versus the wavelength in the IR range.

4.2.3. Conclusion

This section was dedicated to the estimation of thermal properties of bio-aerogel. As both conductive and radiative transfers occur, they have been theoretically modelled through the quadrupole formalism, considering a simple resistance for the radiative transfer in parallel of conduction.

Parameter estimation has been performed through inverse method with the same procedure as in Section 4.1, but theoretical model is this time a temperature-temperature model, meaning that input data are the front face temperatures and observable are the rear face temperatures. This model is very practical since it diminishes drastically the number of unknowns due to instrumentation (Section 4.1.4). Indeed, there were four parameters to estimate, but three were of interest, the last one being the rear face heat exchange coefficient.

The knowledge of global behaviour of heterogeneous porous materials is very convenient in an engineering way for applications. Specific conduction-radiation coupling is a classical topic of research, but it is generally studied through the use of numerical simulations [Kunc 1984][Ping 1989][Zeng 1995a][Zeng 1995b][Heinemann 1996][Asllanaj 2007][Chandrasekar 2013] implying therefore high computational time. However, the use of the quadrupole formalism dedicated to radiative transfers is very interesting. Since it offers possibility to run fast analytical models and to go more deeply in microscopic structure of the tested material.

In this experiment, aerogel sample was briefly heated, such as in the flash method [Degiovanni 1977][Degiovanni 2002]. As theoretical model is developed in the Laplace domain, the right form of the heat flux in the time domain should be verify: de Hoog numerical inversion technique has been used successfully. It exists several numerical inversion techniques from Laplace to time domains if no solution can be easily obtained: de Hoog, Stehfest, Fourier.

As mentioned in Section 4.1, this experimentation was not only based on the use of an existing and validated technique, but it was an opportunity to improve and modify it for the necessity of the study. For this purpose, sensitivity studies are powerful tools, they allow:

- to observe that heat exchange coefficient is decorrelated from both thermal and radiative conductivities due the presence of the rear face brass plate;
- to decorrelate thermal conductivity and radiative conductivity with the removal of the first brass plate from [Jannot 2009];
- to define an objective criterion for definition of the thickness of the brass plate.

However, numerous experiments were necessary to obtain satisfying and reliable results. Many times, both thermal and radiative conductivities were correlated, and no sensitivity to the thermal diffusivity was observed. The great difficulty to control the thickness of the sample is a key issue due to its flexibility. The contact resistance between it and the brass plate that has been assumed first negligible should be reconsidered for thin sample. It is thus better to have thicker sample.

Finally, measurement with thermocouples placed on the sample is not appropriate, since their contact can cause a risk of deterioration of the sample. That is why they are placed on the heating element and on the brass plate, implying possible problem of thermal inertia. Measurement without contact can thus be a good alternative with the use of thermography, but it implies reconfiguration of the experiment – and a non-negligible increase of its financial cost. This type of visualization is presented in the next section with the use of infrared thermography in order to estimate in-plane thermal diffusivity of materials ranged between insulators to conductors. So far, experiments were dedicated to in-depth properties.

4.3. Infrared thermography for the in-plane thermal properties estimation of materials in a large range of thermal conductivities [Pierre 2019a][Pierre 2020][Pierre 2022]

4.3.1. Context

[Pierre 2019a] and [Pierre 2020] are in the continuity of [Pierre 2014]. They are based on the development of experiment dedicated to thermal characterization of millimeter-sized material: hemp shiv. In the domain of building, there is a lack of knowledge concerning thermal properties of hemp shiv, one of the components of hemp concrete, porous heterogeneous material. The most common data concern effective thermal conductivity of loose hemp shives through the hot-wire technique [Sjöström 2014], but there is no direct experimental measurement of hemp shiv itself. However, literature mentions estimation of effective conductivity by inverse method between experimental results and complete numerical model of the hemp concrete considering size and orientation of hemp shives [Nguyen 2016][Dartois 2017]. Experiments dedicated to thermal characterization of materials of small thicknesses are difficult and technical issues increase when the samples become millimeter-sized and less. Encountered difficulties concern the type of solicitation, the measurement of the heat flux dissipated in the sample, the size, and the location of the thermocouple. Rémy *et al.* proposed an original method to circumvent the problem of boundary conditions based on a particular treatment of the theoretical problem of fin model in Cartesian coordinates, and performed transient measurements of temperature on low conductive material using IR camera [Rémy 2005]. The theoretical model is a temperature-temperature one where the temperature at a position z is linearly related to temperatures at positions z_1 and z_2 knowing that $z_1 < z < z_2$. In [Pierre 2022], we have adapted the model proposed by Rémy *et al.* [Rémy 2005] to a cylindrical coordinate system with finite and semi-infinite medium and for broad range of isotropic and anisotropic materials. Other criteria have also been added in this study to discuss the quality of estimations, such as correlation coefficients between parameters.

Section 4.3.2 presents both theoretical development in Cartesian and cylindrical coordinates. Section 4.3.3 concerns sensitivity studies and inverse problem in both cases. Finally, Section 4.3.4 deals with experimental results still in both cases, first in Cartesian coordinates, then in cylindrical coordinates.

4.3.2. The theoretical models

4.3.2.1. The Cartesian model

As depicted in Figure 4.20, a heat flux $\varphi(t)$ is applied on the top surface of the sample. Heat losses are considered on the other surfaces. In fin model, only heat transfer along the descendent z- direction is taken into account. The heat equation is then given by Eq. (4.52), where $\bar{T}(z,t) = T^*(z,t) - T_\infty$ is the average temperature of the cross section at the location z, k and α are, respectively, the thermal conductivity and diffusivity of the sample, h is the heat exchange coefficient, e and ℓ are the sample thickness and width, respectively, T^* is the sample temperature and T_∞ is the room temperature.

$$\frac{\partial^2 \bar{T}}{\partial z^2} - \frac{2h(e+\ell)}{el}\frac{\bar{T}}{k} = \frac{1}{\alpha}\frac{\partial \bar{T}}{\partial t} \tag{4.52}$$

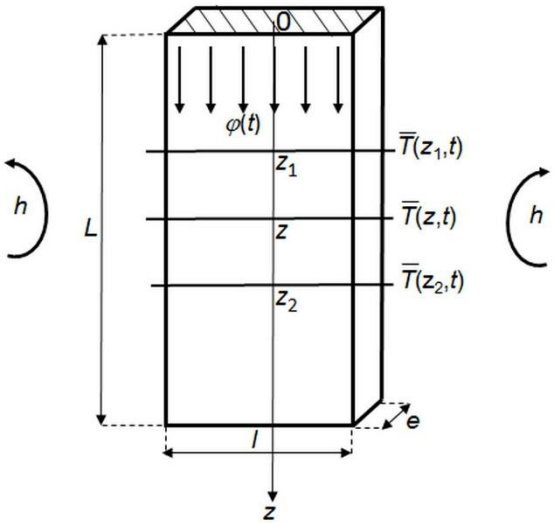

Figure 4.23. Sketch of the sample.

Eq. (4.52) is easily solved using Laplace transform and quadrupole formalism [Maillet 2000]. Since boundary conditions are not known precisely, the method proposed by Rémy *et al.* [Rémy 2005] considers a linear combination between temperature at location z with temperatures located at positions z_1 and z_2 on either side of z as presented in Eqs. (4.53)-(4.57) and Figure 4.23, where s is the Laplace parameter.

$$\bar{T}(z,t) = \bar{T}(z_1,t) \otimes \mathcal{L}^{-1}[\mathcal{T}_1(z,s)] + \bar{T}(z_2,t) \otimes \mathcal{L}^{-1}[\mathcal{T}_2(z,s)] \tag{4.53}$$

$$\mathcal{T}_1 = \frac{sinh[\omega(z_2 - z)]}{sinh[\omega(z_2 - z_1)]} \tag{4.54}$$

$$\mathcal{T}_2 = \frac{sinh[\omega(z - z_1)]}{sinh[\omega(z_2 - z_1)]} \tag{4.55}$$

$$\omega = \sqrt{\frac{s}{\alpha} + H} \tag{4.56}$$

$$H = \frac{h(e + l)}{kel} \tag{4.57}$$

Transmittance $\mathcal{T}$ depends on two parameters: in-plane thermal diffusivity α and modified Biot number H.

4.3.2.2. The cylindrical model

The quadrupole formalism [Maillet 2000] expresses temperature along the r-direction between two coordinates r_1 and r (Figure 4.24).

$$\begin{bmatrix} \theta(r_1, s) \\ \Phi(r_1, s) \end{bmatrix} = \begin{bmatrix} A & B \\ C & D \end{bmatrix} \begin{bmatrix} \theta(r, s) \\ \Phi(r, s) \end{bmatrix} \tag{4.58}$$

$$A = \omega r[K_1(\omega r)I_0(\omega r_1) + K_0(\omega r_1)I_1(\omega r)] \tag{4.59}$$

$$B = \frac{1}{2\pi kl}[I_0(\omega r)K_0(\omega r_1) - I_0(\omega r_1)K_0(\omega r)] \tag{4.60}$$

$$C = 2\pi kl\omega^2 r_1 r[K_1(\omega r_1)I_1(\omega r) - K_1(\omega r)I_1(\omega r_1)] \tag{4.61}$$

$$D = \omega r_1[K_1(\omega r_1)I_0(\omega r) + K_0(\omega r)I_1(\omega r_1)] \tag{4.62}$$

where I_0, I_1, K_0, and K_1 are the modified Bessel functions.

In time domain, temperature at radius r is linearly related to temperature at radius r_1 as:

$$T(r, t) = T(r_1, t) \otimes \mathcal{L}^{-1}[\mathcal{T}(r, s)] \tag{4.63}$$

$$\mathcal{T}(r, s) = \frac{K_0(\omega r)}{K_0(\omega r_1)} \tag{4.64}$$

$$H \approx \frac{2h}{ke} \tag{4.65}$$

Transmittance $\mathcal{T}$ depends on the same parameters as before: in-plane thermal diffusivity α and modified Biot number H. Contrary to Cartesian model, only experimental temperature $T(r_1, t)$ is necessary as input data.

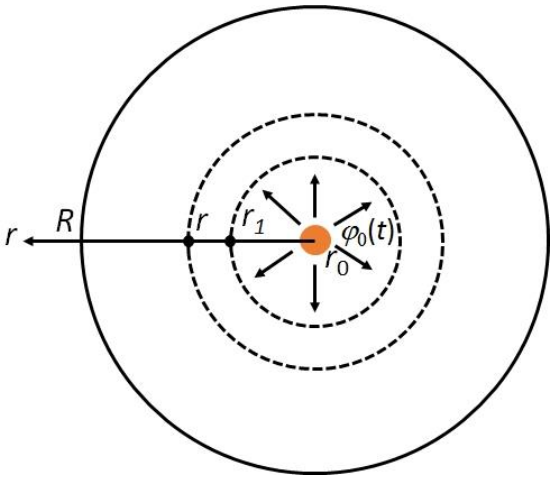

Figure 4.24. Sketch of the theoretical radial model for semi-finite medium.

4.3.3. The inverse problem and the sensitivity study

4.3.3.1. The Cartesian model

In practice, temperatures $\bar{T}(z_1,t)$ and $\bar{T}(z_2,t)$ are experimental ones $\bar{T}^{exp}(z_1,t)$ and $\bar{T}^{exp}(z_2,t)$ obtained through infrared thermography at locations z_1 and z_2, respectively. Theoretical temperature $\bar{T}(z,t)$ in Eq. (4.53) is fitted with experimental temperature $\bar{T}^{exp}(z,t)$ by ordinary least-squares regression coupled with LM algorithm by estimating thermal diffusivity α and modified Biot number H, by solving criteria (4.66) where $\boldsymbol{\beta} = [\alpha, T]^T$ represents the parameters, M the number of points, and σ the noise standard deviation:

$$\sum_{k=1}^{M} |\bar{T}(z,t_k,\boldsymbol{\beta}) - \bar{T}^{exp}(z,t_k)|^2 \rightarrow M\sigma^2 \qquad (4.66)$$

Finally, thermal conductivity and heat exchange coefficient can be deduced from measurements of heat capacity c_p^m and density ρ obtained by appropriate apparatus.

The possibility to estimate both thermal diffusivity and modified Biot number lays on sensitivity analysis of temperature $\bar{T}(z,t)$ with these parameters. Reduced sensitivity (4.22) is plotted in Figures 4.25 and 4.26 for low conductivity materials: polycarbonate and balsa, respectively [Carré 1990][Speight 2005]:

- Polycarbonate: $k = 0.200$ W·m^{-1}·K^{-1}, $\rho = 1\,000$ kg·m^{-3}, $c_p^m = 1\,250$ J·kg^{-1}·K^{-1};
- Balsa: $k = 0.05$ W·m^{-1}·K^{-1}, $\rho = 100$ kg·m^{-3}, $c_p^m = 1\,400$ J·kg^{-1}·K^{-1}.

and for three types of surrounding conditions (vacuum, natural, and forced convection), with the following values for global heat transfer coefficient:

- Vacuum: $h = 2$ W·m^{-2}·K^{-1} (see Eq. (4.68));

- Natural convection: $h = 10$ W·m^{-2}·K^{-1};
- Forced convection: $h = 40$ W·m^{-2}·K^{-1}.

For natural and forced convection, typical values for air are chosen based on [Incropera 2011]. For natural convection, correlation for laminar flow along a vertical plate of 20 mm long at temperature surface of 313 K and surrounding air at 293 K is used given the experimental set-up. For forced convection, correlation for flat plate in parallel laminar flow is used assuming gas velocity of around 2 m·s^{-1}.

Results are presented in Figures 4.25 and 4.26 for random positions $z_1 = 2$ mm, $z = 3$ mm, and $z_2 = 5$ mm. The solid lines concern temperature sensitivity to thermal diffusivity and dashed line to modified Biot number, and circle ●, star ✶, and triangle ▼ symbols represent, respectively, values $h = 2$, 10, and 40 W·m^{-2}·K^{-1}. In each case, it is shown that estimation of both parameters is possible. As expected, temperature becomes less sensitive to modified Biot number, when the latter decreases.

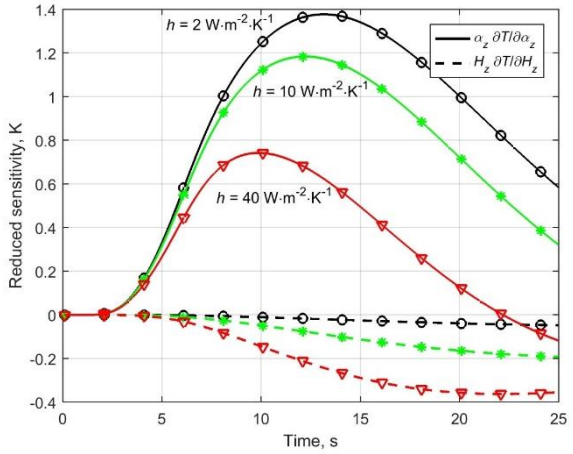

Figure 4.25. Reduced temperature sensitivities for thermal diffusivity and modified Biot number versus time obtained for polycarbonate for three types of environment condition.

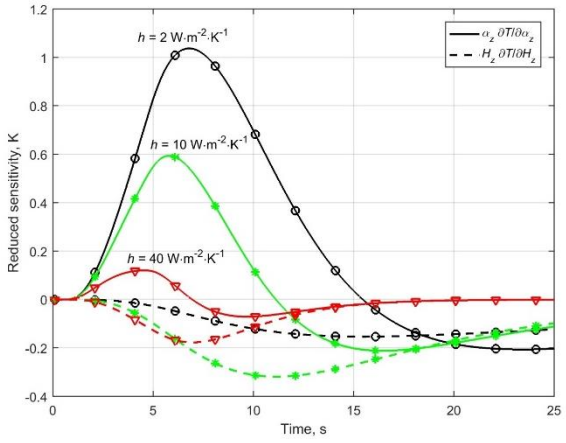

Figure 4.26. Reduced temperature sensitivities for thermal diffusivity and modified Biot number versus time obtained for balsa for three types of environment condition.

4.3.3.2. The cylindrical model

Two experimental temperatures are required to perform an estimation with the relation (4.63): observable $T^{exp}(r,t)$ and input temperature $T^{exp}(r_1,t)$. Estimation procedure is identical with parameters to estimate (4.66).

Reduced sensitivities are presented in the case of balsa and aluminum ($k = 40$ W·m^{-1}·K^{-1}, $\rho = 2\,700$ kg·m^{-3}, $c_p^m = 860$ J·kg^{-1}·K^{-1} [Geslain 2018]) in Figures 4.27 and 4.28, respectively. Both figures show different behaviors between sensitivity to in-plane thermal diffusivity and to modified Biot number, which allows to predict that estimation of both parameters seems possible. In Figure 4.27, for balsa, sensitivity to modified Biot number H decreases slowly, but in Figure 4.28 transfer function seems to be insensitive to H in the case of aluminum, which presumes that its estimation would be difficult.

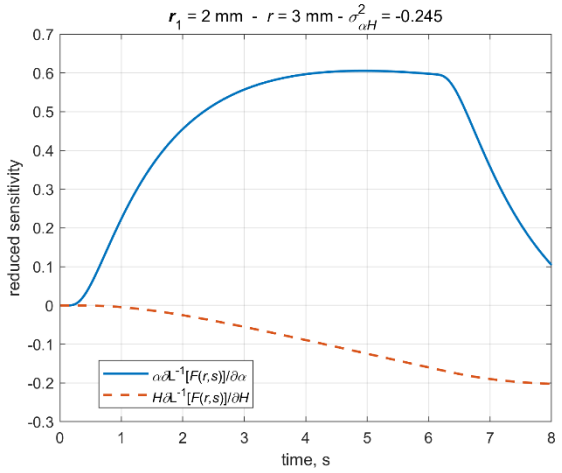

Figure 4.27. Reduced sensitivity curves to α and H in the case of the balsa.

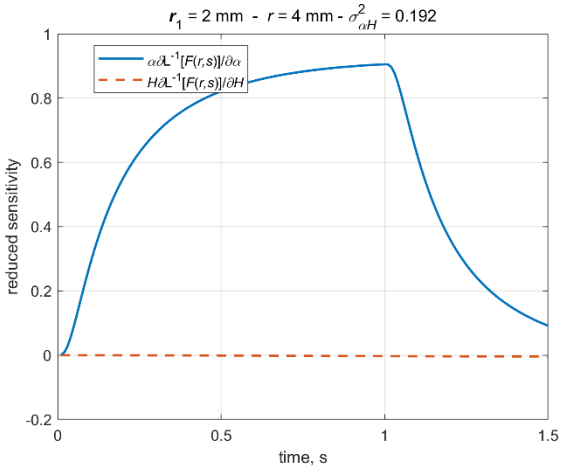

Figure 4.28. Reduced sensitivity curves to α and H in the case of the aluminum.

In this section, correlation coefficient $\sigma_{\alpha H}^2$ [Beck 1977] has been studied to see correlation level between both parameters. "Parameters tend not to be correlated when $\sigma_{\alpha H}^2$ tends to 0, and on the contrary become more and more correlated when $\sigma_{\alpha H}^2$ tends to $\pm$ 1" [Rigollet 2019]. This parameter is studied versus two positions r_1 and r, which are not as random as expected. Here is presented the case of choice of position r, and more precisely distance $r - r_1$. In Figure 4.27 for the balsa and $r - r_1 = 1$ mm $\sigma_{\alpha H}^2 = -0.245$, and in Figure 4.28 for the aluminum and $r - r_1 = 2$ mm $\sigma_{\alpha H}^2 = 0.192$. Figure 4.29 shows for balsa and aluminum theoretical evolution of $\sigma_{\alpha H}^2$ versus distance $r - r_1$. It is shown that

the former has a minimum value, corresponding to a minimum correlation between in-plane thermal diffusivity and modified Biot number.

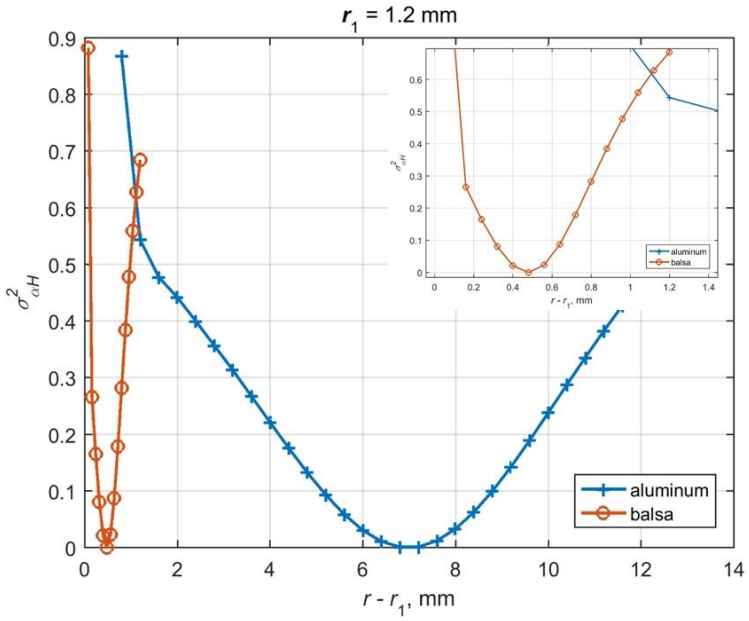

Figure 4.29. Comparison between evolution of correlation $\sigma^2_{\alpha H}$ coefficient for balsa and aluminum.

4.3.4. Experiments, results and discussion

Experiments using Cartesian and cylindrical models are quite similar. First, Figures 4.30 and 4.31 present global view of experimental apparatus composed of a stainless steel chamber with a sapphire window in which the heated sample is placed, and of an IR camera. Vacuum can be performed within the chamber. IR camera is a Flir X6580sc model working in the range [1.5 µm – 5.1 µm] and equipped with a 15 µm resolution microscopic lens. The acquisition frequency is 50 Hz and the tests last 30 s. Sample is warmed with a heating element covered by a thin aluminum foil, on which test sample is stuck. Aluminum foil is used to avoid radiation of the heating element to the sample. Type K thermocouple is placed at the rear side of the sample only to control initially the temperature given by the camera, then it is removed. A continuous heating is applied until sample surface temperature has increased by a maximum of about 20 K. Three types of surrounding are considered in the stainless steel chamber: vacuum, natural convection, and forced convection. It is noteworthy that the air velocity is not measured and the Reynolds number cannot be calculated.

The second experimental set-up, developed to correspond to the theoretical model, is presented in Figures 4.32 and 4.33. A thin sample is heated on its center by a heating source. The heating source is a cylindrical copper spot of about $r_0 = 1$ mm radius embedded in the sample and heated by Joule effect through electric current coming from the sample rear face. The electric wires are maintained with conductive stick, which should be let dry at least for 24 hours. Then the heating element is switched on few seconds and turned off when a maximum temperature increase of 10 K is reached in the sample or when semi-infinite assumption is no more valid. All tested samples are gathered in Table 4.4.

Table 4.4. Synthesis of the materials tested for the Cartesian and the cylindrical models.

Material	Cartesian model	Cylindrical model
Polycarbonate	x	x
Balsa ⊥	x	x
Balsa //	x	x
Hemp shiv ⊥	x	
Hemp shiv //	x	
Steel DC54		x
Aluminum AA5182		x

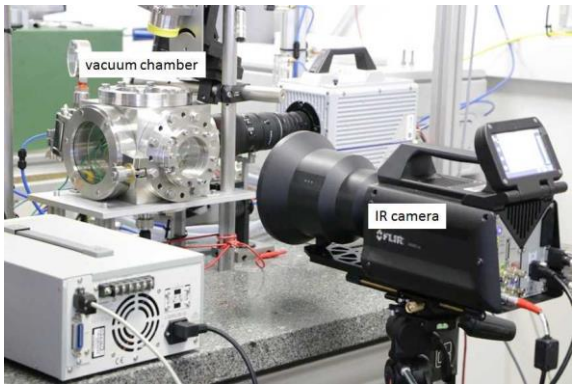

Figure 4.30. Experimental apparatus: vacuum chamber and IR camera.

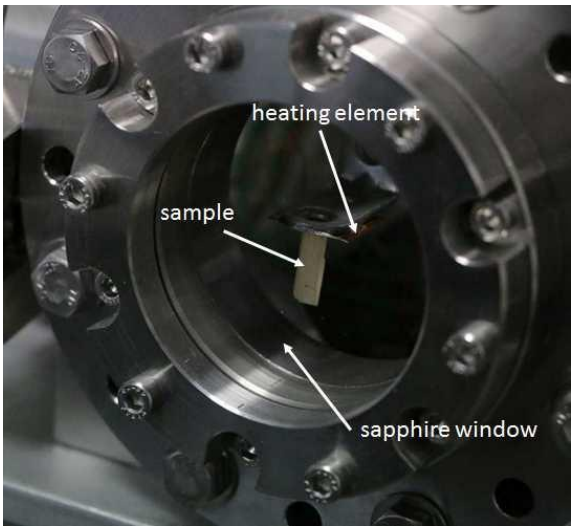

Figure 4.31. Experimental apparatus: sample and heating element.

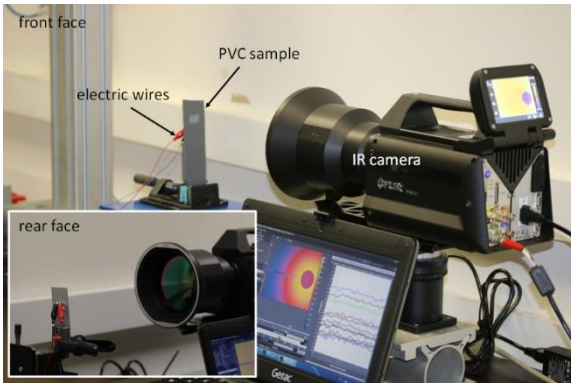

Figure 4.32. View of experimental set-up.

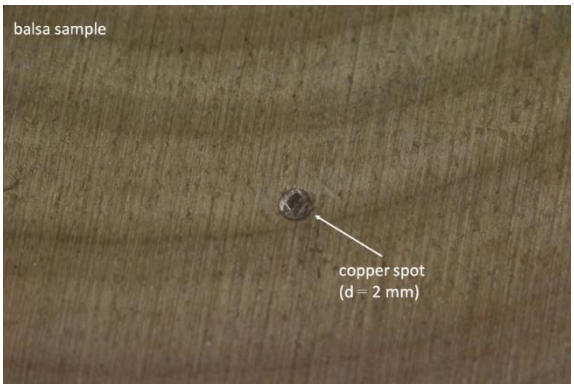

Figure 4.33. View of the copper spot embedded in the balsa sample.

For the first study, Figure 4.34 shows example of IR image of the balsa sample with five lines located at positions $z = 0$ mm, 0.99 mm, 1.77 mm, 2.90 mm, and 4.14 mm, where ten combinations are possible. Average temperature of each line is recorded versus time. Figure 4.35 plots both evolutions of the five average temperatures (solid lines) at these locations and their temperature derivatives (dashed lines) versus time:

$$\frac{\partial \overline{T}(z,t)}{\partial t} \tag{4.67}$$

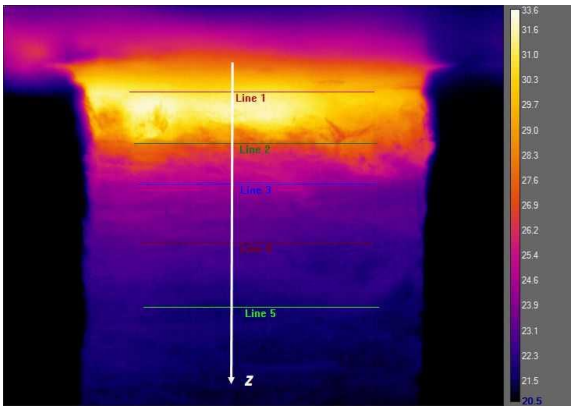

Figure 4.34. Example of IR thermogram for balsa. Temperature scale shown on the right is expressed in degree Celsius.

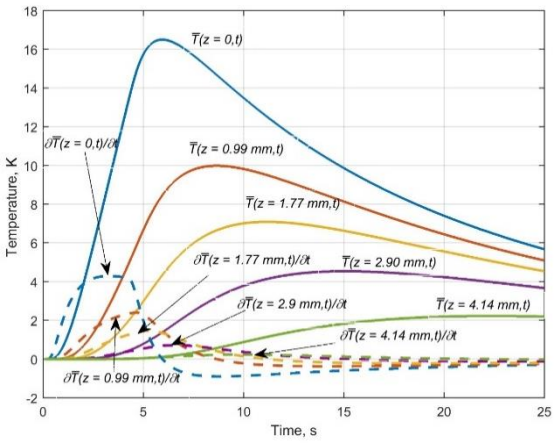

Figure 4.35. Evolution of th temperature rises and their time derivatives at z-positions versus time.

Derivatives decrease when the z-positions increase as expected. Indeed, temperature is less sensitive to thermal diffusivity if the derivative becomes null, which is almost the case for temperature $\overline{T}(z = 4.14 \text{ mm}, t)$. However, for three temperatures

with high enough time derivatives, plot shows that estimation time must last until the second time derivative $\partial \bar{T}(z = 4.14 \text{ mm}, t)/\partial t$ reaches its maximum.

Quality of the estimation is also discussed through calculation of covariance $\sigma_{\alpha H}$ from covariance matrix (4.47) and of residuals.

Table 5 gathers estimation results for the ten possible combinations when balsa is in vacuum. Once thermal diffusivity is estimated, the thermal conductivity is calculated using values of density ρ and heat capacity c_p^m from measurements performed in our laboratory with a micro calorimeter for each sample [Pierre 2019a]. Finally, combination of Eq. (4.57) and (4.3) is used to calculate heat exchange coefficient h.

Table 4.5. Estimation results for all possible combinations in the case of balsa in vacuum.

combination	$z_i/z/z_j$ mm/mm/mm	convergence	$\sigma_{\alpha H}$	α $mm^2 \cdot s^{-1}$	h $W \cdot m^{-2} \cdot K^{-1}$	covariance matrix of residuals
1	0/0.99/1.77	yes	0.047	0.304	0.7	0.022
2	0/0.99/2.90	yes	0.0008	0.407	2.9	0.032
3	0/0.99/4.14	yes	0.104	0.467	3.7	0.017
4	0/1.77/2.90	yes	0.115	0.228	9.4	0.197
5	0/1.77/4.14	yes	0.097	0.378	9.2	0.185
6	0/2.90/4.14	yes	0.125	0.319	10.9	0.230
7	0.99/1.77/2.90	no	1	x	x	x
8	0.99/1.77/4.14	no	1	x	x	x
9	0.99/2.90/4.14	no	1	x	x	x
10	1.77/2.90/4.14	no	1	x	x	x

Convergence is not achieved for the four last combinations, due to null time derivative of the temperature. The six first cases are successful, covariance between thermal diffusivity and heat exchange coefficient is close to zero, which means that both parameters can be estimated separately. As experiment is performed in vacuum, valuable estimation of heat exchange seems to be for combinations 2 and 3, where both covariances are weak. In vacuum, theoretical linearized heat exchange coefficient is evaluated at $h = 3.3$ $W \cdot m^{-2} \cdot K^{-1}$ using the following expression:

$$h = 4\varepsilon\sigma T^3 \tag{4.68}$$

where here $T$is in kelvin, ε is the emissivity of balsa. Thus, thermal diffusivity is estimated considering results from combinations 2 and 3.

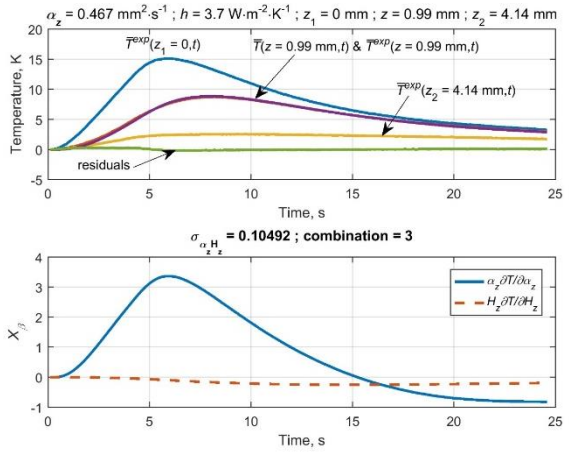

Figure 4.36. Example of estimation and results in the case of balsa in vacuum.

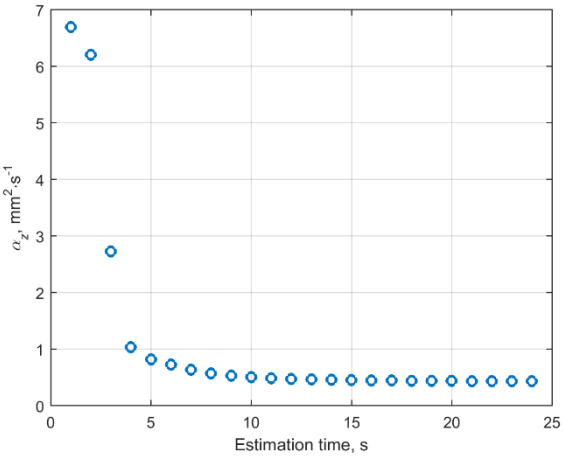

Figure 4.37. Evolution of estimated thermal diffusivity over estimation time in the case of balsa sample during experiment in vacuum.

Figure 4.36 presents estimation plots for combination 3. The upper figure plots temperature evolutions versus time and residuals. The lower figure plots reduced sensitivities of estimated temperature $\bar{T}(z,t)$ versus estimated parameters. As previously shown in Figure 4.26, sensitivity of temperature to heat exchange coefficient in vacuum is very weak compared to sensitivity to thermal diffusivity. Last point concerns estimation time. Figure 4.37 plots evolution of estimation of thermal diffusivity versus estimation time. Obviously, it is necessary to have a minimum time of estimation, since estimated values tend to a constant one: a minimum estimation time of 10 s is required. This observation can be related to sensitivity of time derivative (4.68), which tends to zero after 10 s after reaching its maximum as shown in Figure (4.22).

The present methodology is applied to five samples presented in Table 4.4 for three kinds of environment conditions in the chamber. Figures 4.38 to 4.41 gather all estimation results for the five samples.

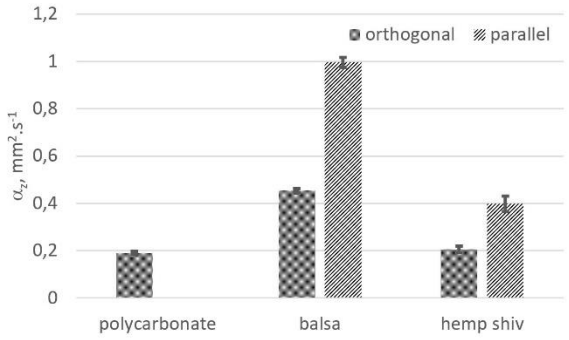

Figure 4.38. Thermal diffusivity results for all samples with their uncertainties.

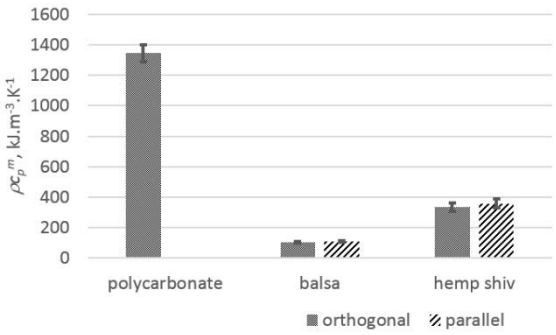

Figure 4.39. Volumetric heat capacity results for all samples with their uncertainties.

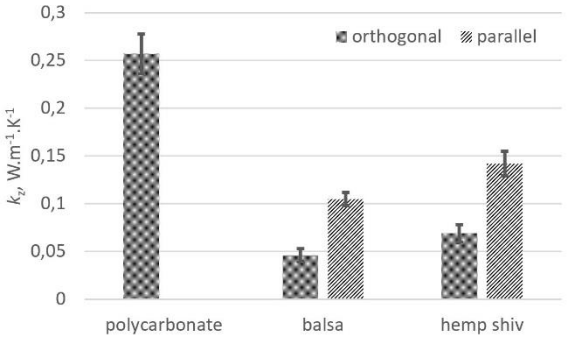

Figure 4.40. Thermal conductivity results for all samples with their uncertainties.

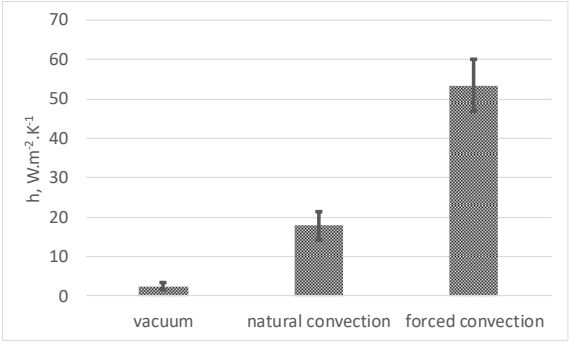

Figure 4.41. Heat exchange coefficients for three experimental conditions with their uncertainties.

Estimation of thermal diffusivity (Figure 4.38) of polycarbonate leads to an average value of same order of magnitude but higher than literature of 28 % [Speight 2005]. Estimation of thermal diffusivities of balsa shows a ratio of about 2.2 between parallel and orthogonal samples, which is consistent with results found in literature [Carré 1990][Speight 2005]. Same observation can be done for hemp shives, which values of thermal conductivity are also consistent with literature for cellulosic materials [Carré 1990] and less than 25 % higher compared to estimated values of [Dartois 2017]. Most of the time, covariance matrix tends to a null value, which makes considering that both parameters are uncorrelated and have been estimated properly. The only cases where covariance matrix is close to unity is for parallel balsa during measurements in the vacuum and with natural convection. It is probably because *z*-positions were not well-chosen; change them would help to get a better covariance and a stronger estimation. In Figure 4.39, two close values for volumetric heat capacities appear for balsa, on the one

hand, and for hemp shiv, on the other hand. These results are consistent with the fact that it is a volumetric property, which does not depend on direction of the fibres, contrary to thermal conductivity (Figure 4.40) and consequently to thermal diffusivity. Finally, estimated heat exchange coefficients (Figure 4.41) seem consistent with the type of environment condition, even if results are rather scattered and independently of estimated thermal diffusivity values. Despite the fact that Figures 4.25 and 4.26 show a decreasing influence of the heat exchange coefficient from forced convection to vacuum environment, discrepancy regarding estimation of thermal diffusivity appears to be relatively stable for the three environment conditions, probably due the seeking of the z-positions, which change from one experiment to another.

For the second study, every infrared scene at each time step are recorded and then analyzed with the help of a Matlab® program. As shown in Figure 4.42, the position $r = 0$ is the center of the copper spot and is defined through the position (x_0, y_0) in the infrared scene. Therefore, it is easy to know location of temperature $T(r;t)$ for some given r radius and θ angle, in (x, y) coordinate system, with the following relations:

$$x = x_0 - r\cos(\theta) \tag{4.69}$$

$$y = y_0 - r\sin(\theta) \tag{4.70}$$

Contrary to previous study which is valid for average temperatures, this one deals with temperatures of unique pixel, implying possible weak signal-to-noise ratio. Conversion from pixel to distance is made possible thanks to the resolution (15 µm).

With PVC sample, for two given r_1 and r positions, and for different angles ranged between 0 and $\pi/2$ according to Eqs. (4.69) and (4.70), Figure 4.43 presents experimental temperatures of roughly same evolutions versus time. They are almost independent of the angle, confirming therefore the isotropic nature of PVC. Tests with mild steel and aluminum alloy present similar observations.

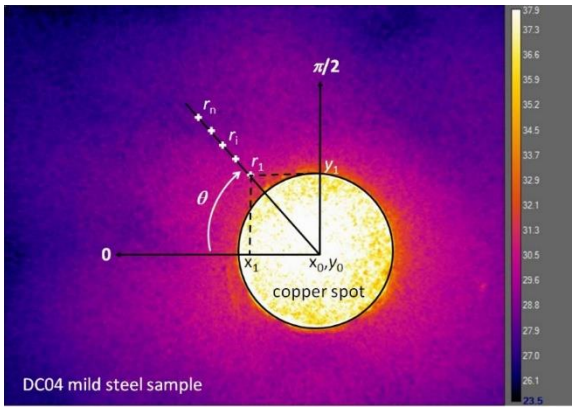

Figure 4.42. Representation of infrared scene measured for mild steel and of relation between Cartesian and polar coordinates. Scale on the right is temperature expressed in degrees Celsius.

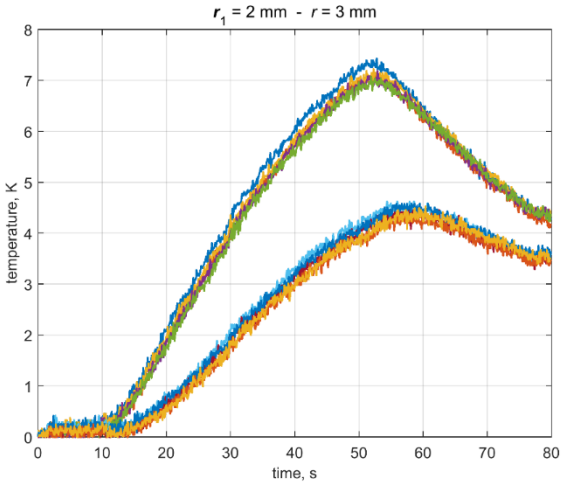

Figure 4.43. Experimental temperature variations of PVC for angles $\theta = 0$, $\pi/6$, $\pi/4$, $\pi/3$, $\pi/2$ and for $r_1 = 2$ mm (the highest) and $r = 3$ mm.

Now estimation results are presented. Figure 4.44 presents correlation coefficient $\sigma_{\alpha H}^2$ as a function of the distance $r - r_1$ for $r_1 = 2$ mm and r varying until maximum distance filmed by infrared camera ($r_1 - r = 3$ mm), which varies with experiments. Figure 4.44 presents similarities with Figure 4.29 with a minimum for $r - r_1 = 0.7$ mm. It shows that for $r - r_1 < 0.70$ mm, covariance varies to large extent with values close to 1: fitting of theoretical model on experimental temperature is unsuccessful and estimated values have no meaning. For $r - r_1 > 0.70$ mm, covariance increases slightly from 0.45 to 0.7 and theoretical model fits on experimental temperatures: large possibilities exist to estimate the properties. An Example of temperature estimation during test with PVC for $\theta = 0$ is presented in Figure 4.45, for given position $r_1 = 2$ mm and $r_1 - r = 0.7$ mm when covariance $\sigma_{\alpha H}^2$ starts to have low value. Residuals are constantly around zero. Estimation is extended for several positions r_1. For a given r_1, position r is searched to reach minimum of $\sigma_{\alpha H}^2$ over the distance $r - r_1$ and, then, estimated parameters are recorded.

The methodology is applied to some samples presented in Table 4.4, and Table 4.6 gathers all estimation results for the five samples.

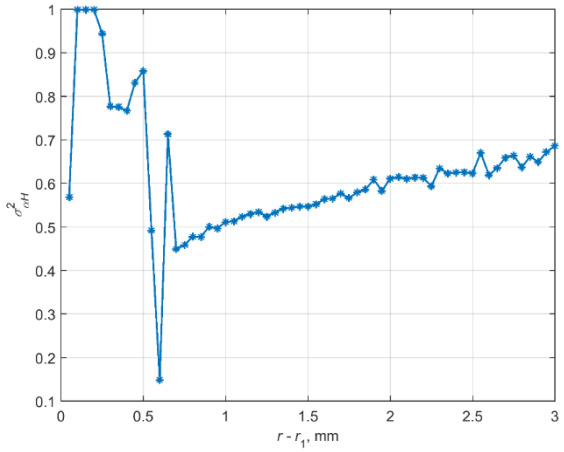

Figure 4.44. Evolution of the variance $\sigma^2_{\alpha H}$ versus distance $r - r_1$ for $\theta = 0$ and $r_1 = 2$ mm.

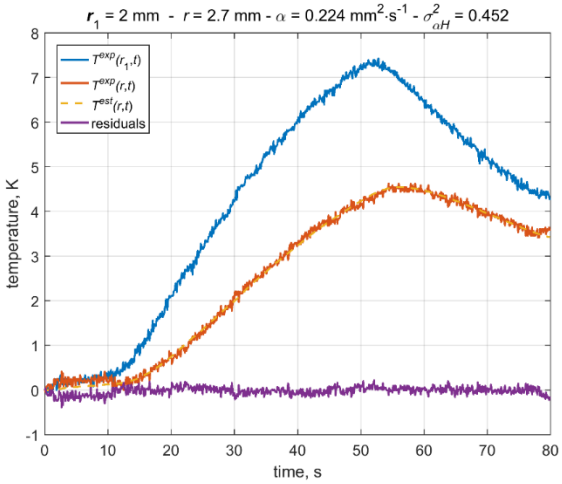

Figure 4.45. Experimental and estimated temperatures during test with PVC.

Table 4.5. Estimation results for the four samples (* interpolated value from laboratory measurements, ** for $h = 10$ W·m^{-2}·K^{-1}).

	balsa ⊥	balsa //	PVC	DC54	AA5182
r_1 (mm)	2.00	2.00	2.00	2.00	2.00
r_{min} (mm)	3.15	3.10	3.15	4.65	6.00
$\alpha^{est} \pm \sigma_\alpha$ (mm^2·s^{-1})	0.97 ± 0.27	1.20 ± 0.38	0.22 ± 0.03	19 ± 4	49 ± 17
α literature (mm^2·s^{-1})	0.48 ± 0.02	0.95 ± 0.03	0.20 ± 0.03	18.70*	$53.6^* \pm 1.4^*$
$H^{est} \pm \sigma_H$ (10^3 m^{-2})	90 ± 30	21.5 ± 6.9	31.0 ± 4.5	-	-
h (W·m^{-2}·K^{-1})	4.1 ± 2.1	4.5 ± 1.9	7.8 ± 2.0	-	-
k (4.65)	0.09 ± 0.06	0.02 ± 0.03	0.03 ± 0.02	$< 10^{-3}$**	$< 10^{-3}$**

For PVC, estimated in-plane thermal diffusivity α has a mean value similar to reference. Regarding modified Biot number H, distribution is more uniform and scattered, which may be due to the low sensitivity of this parameter. Nevertheless, from thermal conductivity value of PVC found in literature, calculation of heat exchange coefficient h gives a consistent value for free convection [Incropera 2011].

For DC54 mild steel, and AA5182 aluminum alloy, in-plane thermal diffusivity estimation is consistent with literature. However, dispersion is important (particularly for aluminum alloy). Because of the high in-plane thermal diffusivity of metallic samples and the limited power supply, temperature increase could not be above 3 K for aluminum alloy (instead of 10 K). On the one side, this makes the choice of the position r_1 more difficult. On the other side, modified Biot number H cannot be estimated, since observable is insensitive to it. Tests with aluminum show one limitation of the techniques considering the current size of the sample. A solution is to work with larger sample and supply a higher electric power to reach 10 K and have higher signal-to-noise ratio.

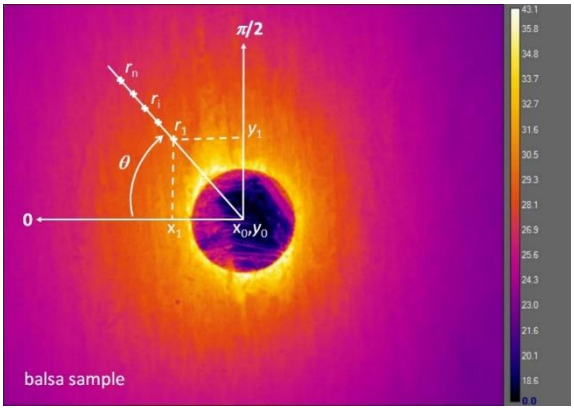

Figure 4.46. Infrared scene of balsa with fibers oriented in vertical direction ($\theta = \pi/2$). Scale on the right is temperature expressed in degrees Celsius.

Finally, balsa is tested. In Figure 4.46, temperature distribution is not homogeneous highlighting anisotropic structure of the material. Here, heat flux tends to flow preferentially along natural orientation of fibers. Except some points, all results are centered on a single value with a rather important standard deviation. The mean values have the same order of magnitude than literature data [Pierre 2019]. Nevertheless, it is slightly lower in longitudinal direction and higher in transverse direction. Therefore, thermal diffusivity ratio between both directions is only 1.3, compared to the ratio of 2.2 measured by guarded hot-plate technique [Carré 1990]. On the other hand, modified Biot number H ratio is equal to 2.5 assuming identical heat exchange coefficient in both directions.

Choice of r_1 position is experimental and can vary from one sample to another. Of course, it must be placed after r_0, meaning beyond the radius of the copper spot, but not

too close to avoid some potential effects of contact resistance between the copper spot and the sample.

Heat exchange coefficient h is consistent with free convection values considering estimated values of H and thermal conductivity k of samples found in literature. Besides, real Biot number ($he/2k$) is calculated to verify the fin effect assumption. A value of $h = 10$ W·m^{-2}·K^{-1} is considered for aluminum and mild steel. Except for measurements with balsa with $\theta = 0°$, where $Bi = 0.09 \pm 0.06$, meaning close to the limit value of 0.1, the fin effect assumption is always verified.

4.3.5. Partial conclusion

Theoretical models proposed in these three publications allowed to estimate by inverse methods in-plane thermal diffusivity of different materials with the help this time of non-contact infrared thermography. Experimentally, infrared camera measured all temperatures necessary for the theoretical direct temperature-temperature model, which remains very convenient, since the unwanted parameters are reduced to one coefficient. This coefficient is assimilated to a Biot number, since it depends on thermal conductivity, on the heat losses due to the fin effect, and on dimensions of the material.

Sensitivity study showed that influence of the Biot number decreases for weak heat losses (*e. g.* vacuum) and for conductive materials (*e.g.* aluminum). And once again, coefficient correlation matrix permitted to:

- discuss the choice of temperatures used as input data of observable;
- discuss quality of the estimation;
- give more precise information about minimum estimation time.

Generally, these experiments allowed to characterize samples of millimetric dimensions and even more, and also of insulating to conductive materials. It is required to consider a maximum temperature increase of 10 K, in order to assume temperature-independent of thermal properties of the sample.

Characterization becomes more difficult with the decrease of conductivity, due to non-linearity of the heat losses. Measurements in vacuum is an appropriate substitution environment for insulating materials. On the contrary, characterization of conductive materials of small dimensions becomes difficult due to the quick dissipation of heat. Samples of greater dimensions are required.

Fin effect assumption allows to focus only on one face of the sample, and thus the use of infrared camera. This apparatus offers many advantages. It allows a global visualization of the sample and the possibility to record thermal images over time for the post-treatment with a sufficient frequency.

The microscopic G1 lens gives access to scene with a resolution of 15 µm, meaning that one pixel covers a surface of 225 µm²: a surface about 50 times smaller than with type K thermocouple of 125 µm of diameter presented in Section 4.2.3. But signal is more impacted by the noise (Figure 4.45). It should be advantageous to consider average temperature given by 50 pixels instead of one pixel such as in Figure 4.34.

It was previously mentioned that a maximum temperature increase should not exceed 10 K to assume physical properties independent of temperature and thus make possible analytical solution. Measurements in a maximum 10 K temperature range gives the possibility to use digital level information of the camera instead of temperature, as long as there exists linear evolution between them such as presented in Figure 4.47 for IR camera used for these studies. If the initial temperature of the sample is the room temperature, it is not necessary to mention emissivity of the sample in the setting of the camera.

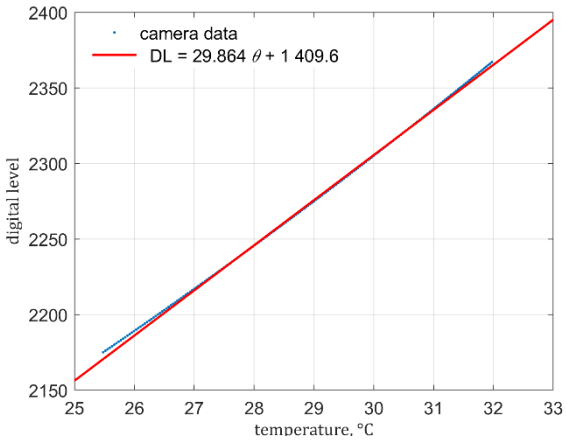

Figure 4.47. Sensitivity of the infrared camera in the range [25 °C – 32 °C].

4.4. Conclusion

This Section 4 was dedicated to thermal characterization by inverse methods of materials of different natures when the sample is heated by contact. This section was mainly focused on the use of analytical and semi-analytical models for the definition of experimental protocols.

Solving heat transfer problems consist in developing direct model, which gives results with acceptable uncertainties after acceptable calculation time. Therefore, for pure heat transfers, analytical or semi-analytical models must be privileged since they are quicker than numerical ones. Moreover, the geometry and the nature of the studied materials offer possibility to make other simplifications with the help of adimensioned numbers (Biot number, Fourier number). 3D problem can become 2D, 1D, or even 0D (lumped body). For parameter estimation, reducing calculation time is of course important matter, but not only. It is also important to reduce the number of unknown parameters that are not of interest. That is the objective of the use of temperature-temperature models instead of flux-temperature ones.

Experimentally, temperature measurements are classically done in contact with thermocouples or without contact with infrared camera. Standard thermocouples are very easy to make, cheap, strong, and deliver linear evolution of a voltage versus temperature. But they are intrusive and can offer only punctual observation of the temperature of a material, and their response time increases with the diameter of the tip. They are convenient in the case of non-porous, homogeneous materials. On the contrary, infrared camera is very practical, but very expensive. It allows to get a global view of a sample and make possible multiple post-treatment with a resolution smaller than the thermocouple and an acquisition frequency equivalent as for the thermocouple.

Inverse methods were not the object of this Section 4. They are presented in Section 5 dedicated to temperature-emissivity estimation by multispectral pyrometry.

References

[André 1995] S. André, A. Degiovanni, *A theoretical study of the transient coupled conduction and radiation heat transfer in glass: phonic diffusivity measurements by the flash technique*, Int. J. Heat Mass Transf., vol. 38, nº 18, p. 3401-3412, 1995.

[Asllanaj 2007] F. Asllanaj, X. Brige, and G. Jeandel, *Transient combined radiation and conduction in a one-dimensional non-gray participating medium with anisotropic optical properties subjected to radiative flux at the boundaries*, J. Quant. Spectrosc. Radiat*. Transf.*, vol. 107, no. 1, pp. 17–29, 2007.

[Beck 1977] J. V. Beck, K. J. Arnould, Parameter estimation in engineering and science, Ed. Wiley & Sons, New-York, 1977.

[Bennai 2018] Bennai, F., et al. « Experimental Characterization of Thermal and Hygric Properties of Hemp Concrete with Consideration of the Material Age Evolution ». *Heat and Mass Transfer*, vol. 54, nº 4, avril 2018, p. 1189-97.

[Bourdot 2017] Bourdot, Alexandra, et al. « Characterization of a Hemp-Based Agro-Material: Influence of Starch Ratio and Hemp Shive Size on Physical, Mechanical, and Hygrothermal Properties ». *Energy and Buildings*, vol. 153, octobre 2017, p. 501-12.

[Carré 1990] P. Carré, R. Le Gall, *Définition et détermination des conductivités thermiques dans les structures C.V.R. – balsa*, Rev. Gén. Therm. Fr., n°340, p. 211-215, avril 1990.

[Carslaw 1959] Carslaw H. S., Jaegger J. C., Conduction of heat in solids, 2nd edition, Oxford, 1959.

[Chandrasekar 2013] S. Chandrasekhar, *Radiative Transfer*. Courier Corporation, 2013.

[Cuce 2014] E. Cuce, P. M. Cuce, C. J. Wood, and S. B. Riffat, *Toward aerogel based thermal superinsulation in buildings: A comprehensive review*, Renew. Sustain. Energy Rev., vol. 34, pp. 273–299, 2014.

[Dartois 2017] S Dartois, S. Mom, H. Dumontet, A. Ben Hamida, *An iterative micromechanical modeling to estimate the thermal and mechanical properties of polydisperse composites with platy particles: Application to anisotropic hemp and lime concretes*, Construction and Building Materials 152 (2017) 661-671.

[de Hoog 1982] De Hoog F. R., Knight J. H., Stockes A. N., *An improved method for numerical inversion of the Laplace transform*, SIAM J. Sci. Stat. Comput., Vol. 3, No. 3, 1982.

[Degiovanni 2002] Degiovanni, Alain, et al. « Transient Radiation-Conductive Heat Transfer Problems: "The Quadrupole Method" ». *Journal of Thermal Science*, vol. 11, nº 4, novembre 2002, p. 359-71.

[Degiovanni 1977] A. Degiovanni, *Diffusivité et méthode flash*, Revue Générale de Thermique, n°185, mai 1977, p. 420-442.

[Ebert 2011] H.-P. Ebert, *Thermal Properties of Aerogels*, in Aerogels Handbook, M. A. Aegerter, N. Leventis, and M. M. Koebel, Eds. Springer New York, 2011, pp. 537–564.

[Geslain 2018] E. Geslain, *Soudage par résistance des tôles fines revêtues : formation du noyau dans un assemblage de trois tôles*, thèse, Université Bretagne Sud, 2018.

[Grishechko 2013] L. I. Grishechko, G. Amaral-Labat, A. Szczurek, V. Fierro, B. N. Kuznetsov, A. Pizzi, and A. Celzard, *New tannin–lignin aerogels*, Ind. Crops Prod., vol. 41, pp. 347–355, Jan. 2013.

[Guggenheim 1966] Guggenheim E.A., *Application of Statistical Mechanics*, Clarendon Press, Oxford, 1966.

[Hahn 1997] Hahn, O., et al. « Transient Coupled Conductive/Radiative Heat Transfer in Absorbing, Emitting and Scattering Media: Application to Laser-Flash Measurements on Ceramic Materials ». *International Journal of Heat and Mass Transfer*, vol. 40, n° 3, février 1997, p. 689-98.

[Heinemann 1996] U. Heinemann, R. Caps, and J. Fricke, *Radiation-conduction interaction: an investigation on silica aerogels*, Int. J. Heat Mass Transf., vol. 39, no. 10, pp. 2115–2130, 1996.

[Incropera 2011] F. P. Incropera, *Fundamentals of Heat and Mass Transfer*, John Wiley & Sons, 2011.

[Jannot 2004] Jannot, Yves, et Pierre Meukam. « Simplified estimation method for the determination of the thermal effusivity and thermal conductivity using a low cost hot strip ». *Measurement Science and Technology*, vol. 15, septembre 2004, p. 1932-38.

[Jannot 2009] Y. Jannot, A. Degiovanni, G. Payet, *Thermal conductivity measurement of insulating materials with a three layers device*, International Journal of Heat and Mass Transfer 52 (2009) 1105-1111.

[Jannot 2010] Y. Jannot, V. Felix, A. Degiovanni, *A centered hot plate method for measurement of thermal properties of thin insulating materials*, Meas. Sci. Technol. 21 (2010) 035106 (8pp).

[Jannot 2018] Jannot Y., Degiovanni A., *Thermal Properties Measurement of Materials*, ISTE Editions Ltd., London, 2018.

[Krischer 1963] Krischer O., Kroll K., Die Wissenschaftlichen grundlagen der Trocknungstechnik, Springer-Verlag, Berlin, 1963.

[Kunc 1984] T. Kunc, M. Lallemand, J. B. Saulnier, *Some new developments on coupled radiative-conductive heat transfer in glasses – experiments and modelling*, Int. J. Heat Mass Transfer, Vol. 27 No. 12, pp. 2307-2319, 1984.

[Levenberg 1944] Levenberg, K., *A method for the solution of certain nonlinear problems in least squares*, Quart. Appl. Math. 2, 164-168, 1944.

[Maillet 2000] Maillet D., André S., Batsale J.-C., Degiovanni A., Moyne C., Thermal quadrupole (John Wiley and Sons Ltd., Chichester, 2000).

[Marquardt 1963] Marquardt, D. W., *An algorithm for least squares estimation of non-linear parameters*, SIAM J. Appl. Math. 11, 431-441, 1963.

[Niezgoda 2011] M. Niezgoda, D. Rochais, F. Enguehard, P. Echegut, B. Rousseau, *Modeling of time-resolved coupled radiative and conductive heat transfer in multilayer semitransparent materials up to very high temperatures*, Applied Physics Letters 99, 224101 (2011).

[Niezgoda 2012a] Niezgoda M., Modélisation du transfert thermique au sein de matériaux poreux multiconstituants, thèse, Université d'Orlans, 2012.

[Niezgoda 2012b] Niezgoda, Mathieu, et al. *Modeling heat transfer within porous multiconstituent materials*. juin 2012, p. 012001.

[Nguyen 2014] S. T. Nguyen, J. Feng, S. K. Ng, J. P. W. Wong, V. B. C. Tan, and H. M. Duong, *Advanced thermal insulation and absorption properties of recycled cellulose aerogels*, Colloids Surf. Physicochem. Eng. Asp., vol. 445, pp. 128–134, 2014.

[Nguyen 2016] S. T. Nguyen, A. D. Tran-Le, M. N. Vu, Q. D. To, O. Douzane, T. Langlet, *Modeling thermal conductivity of hemp insulation material: A multiscale homogenization approach*, Building and Environment 107 (2016) 127-134.

[Orlande 2011] H. Orlande *et al.*, Thermal Measurements and Inverse Techniques, CRC Press, Taylor & Francis Group, 2011.

[Ozisik 1973] N. Ozisik, *Radiative transfer and interactions with conduction and convection*, John Wiley & Sons, Ltd., New-York, 1973.

[Ozisik 2000] Ozisik N., Heat Conduction (John Wiley and Sons Ltd., New-York, 2000).

[Pierre 2014] Pierre, Thomas, et al. « Measurement of Thermal Properties of Biosourced Building Materials ». *International Journal of Thermophysics*, vol. 35, nº 9, octobre 2014, p. 1832-52.

[Pierre 2017] Thomas Pierre, Clara Jimenez-Saelices, Bastien Seantier, Yves Grohens, *Transient pulsed technique to characterize the radiative and conductive properties of bio aerogels*, International Journal of Thermal Science, 116, p. 63-72, 2017.

[Pierre 2019a] Pierre, Thomas, et Muriel Carin. « Characterization of the Thermal Properties of Millimeter-Sized Insulating Materials ». *International Journal of Thermal Sciences*, vol. 135, janvier 2019, p. 247-55.

[Pierre 2019b] Pierre T., Le Masson P., Jannot Y., Kusiak A., *Thermal characterization by hot-plates*, METTI 7 Advanced School, Porquerolles, France, sept. 29th – Oct. 4th 2019.

[Pierre 2020] Pierre, Thomas, et al. « Transient infrared thermography to characterise thermal properties of millimetre-sized hemp shiv ». *Quantitative InfraRed Thermography Journal*, vol. 17, nº 1, janvier 2020, p. 63-77.

[Pierre 2022] Pierre, Thomas, et al. « In-Plane Thermal Diffusivity Estimation by Radial Fin Method ». *Infrared Physics & Technology*, vol. 120, janvier 2022, p. 103998.

[Ping 1989] T. H. Ping, M. Lallemand, *Transient radiative-conductive heat transfer in flat glasses submitted to temperature, flux and mixed boundary conditions*, Int. J. Heat Mass Transfer, Vol. 32 No. 5, pp. 795-810, 1989.

[Rémy 2005] B. Rémy, A. Degiovanni, D. Maillet, *Measurement of the in-plane thermal diffusivity of materials by infrared thermography*, International Journal of Thermophysics, Vol. 26, No. 2, March 2005.

[Rémy 2006] B. Rémy and A. Degiovanni, *Measurements of the Thermal Conductivity and Thermal Diffusivity of Liquids. Part II: 'Convective and Radiative Effects'*, Int. J. Thermophys., vol. 27, no. 3, pp. 949–969, 2006.

[Rigollet 2019] F. Rigollet, D. Maillet, *Lecture 3. Basics for linear estimation, the white box case*, Metti 7 Advanced School, Thermal Measurements and Inverse Techniques, Volume 1: Lectures, Porquerolles, France, Sept. 29th – Oct. 4th, 2019.

[Rudaz 2014] C. Rudaz, R. Courson, L. Bonnet, S. Calas-Etienne, H. Sallée, and T. Budtova, *Aeropectin: Fully Biomass-Based Mechanically Strong and Thermal Superinsulating Aerogel*, Biomacromolecules, vol. 15, no. 6, pp. 2188–2195, 2014.

[Sacadura 2000] Sacadura J.-F., *Initiation aux transferts thermiques*, éditions Tec&Doc, Paris, 2000.

[Seng 2019] Seng, Billy, et al. « Characterization of a Precast Hemp Concrete. Part I: Physical and Thermal Properties ». *Journal of Building Engineering*, vol. 24, juillet 2019, p. 100540.

[Shi 2013] J. Shi, L. Lu, W. Guo, Y. Sun, and Y. Cao, *An environment-friendly thermal insulation material from cellulose and plasma modification*, J. Appl. Polym. Sci., vol. 130, no. 5, pp. 3652–3658, 2013.

[Sjöström 2014] J. Sjöström, P. Blomqvist, *Direct measurement of the thermal properties of wood pellets: Elevated temperatures, fine fractions and moisture content*, Fuel 134 (2014) 460-466.

[Speight 2005] J. G. Speight, N. A. Lange, *Lange's handbook of chemistry*, McGraw-Hill 2005, 16e éd., p. 2758, 2005.

[Stehfest 1970a] Stehfest H., *Algorithm 368, Numerical inversion and Laplace transforms*, Commun. ACM, 13, 47-49, 1970.

[Stehfest 1970b] Stehfest H., *Remarks on* a*lgorithm 368, Numerical inversion and Laplace transforms*, Commun. ACM, 13, 624, 1970.

[Wang 2008] Wang, Moran, et Ning Pan. « Predictions of Effective Physical Properties of Complex Multiphase Materials ». *Materials Science and Engineering: R: Reports*, vol. 63, no 1, décembre 2008, p. 1-30.

[Wei 2011] G. Wei, Y. Liu, X. Zhang, F. Yu, and X. Du, *Thermal conductivities study on silica aerogel and its composite insulation materials*, Int. J. Heat Mass Transf., vol. 54, no. 11–12, pp. 2355–2366, 2011.

[Wei 2013] G. Wei, Y. Liu, X. Zhang, and X. Du, *Radiative heat transfer study on silica aerogel and its composite insulation materials*, J. Non-Cryst. Solids, vol. 362, pp. 231–236, 2013.

[Xie 2013] T. Xie, Y.-L. He, and Z.-J. Hu, *Theoretical study on thermal conductivities of silica aerogel composite insulating material*, Int. J. Heat Mass Transf., vol. 58, no. 1–2, pp. 540–552, 2013.

[Zeng 1995a] S. Q. Zeng, A. Hunt, and R. Greif, *Theoretical modeling of carbon content to minimize heat transfer in silica aerogel*, J. Non-Cryst. Solids, vol. 186, pp. 271–277, 1995.

[Zeng 1995b] S. Q. Zeng, A. J. Hunt, R. Grief, and W. Cao, *Approximate Formulation for Coupled Conduction and Radiation Through a Medium With Arbitrary Optical Thickness*, J. Heat Transf., vol. 117, no. 3, pp. 797–799, 1995.

5. Temperature emissivity estimation with multispectral pyrometry

This part is dedicated to parameter estimation of both temperature and emissivity of emitting surface with the help of radiative flux. The method is called the multispectral pyrometry. My first works on this subject started during my thesis [Pierre 2007][Pierre 2008]. Then I continued to work again from 2012 during the thesis of L. Dejaeghere [Pierre 2016][Dejaeghere 2018] with the development of a home-made six-wavelength pyrometer. Since 2017, my collaboration with Professor Helcio Orlande from UJFR allows me to use other inverse techniques such as Bayesian inference for simultaneous estimation of temperature and emissivity, since I used to work only with deterministic techniques (OLS) [Pierre 2022][Pierre 2023][Lamien 2023].

This part is divided in three sections. Section 5.1 is dedicated to basics on multispectral pyrometry and general aspects of radiative measurements: different types of signals and calibration. Section 5.2 concerns one major aspect of multispectral pyrometry: the proper selection of wavelengths. Section 5.3 deals with parameter estimation using deterministic and stochastic methodologies.

5.1. Some basics on multispectral pyrometry

5.1.1 Definition

Larousse dictionary briefly defines pyrometry as the “measure of high temperatures” [www.larousse.fr]. Indeed, “pyro” comes from the Greek *πυρ*: fire and evokes high temperatures, and “metry” *μετρον*: the measure. But this definition seems too restrictive with our XXI century eyes. Implicitly, we could complete it by “without contact” since fire suggests a distance, contrary to the measurements with contact by thermocouple. The second point concerns the definition of what are high temperatures. It is a relative point of view and depends on applications. For example, here are four examples of high temperatures with “high-temperature” mentioned in the title of the article: 2 000 °C [Khalid 2008], 300 °C [Ikeuchi 1998], 200 °C [Smith 2000], and -173 °C [Gömöry 1997]. I would suggest that the temperature of a surface is high as long as the surrounding can be ignored. Finally, the qualifying adjective multispectral is easier to understand, meaning at several wavelengths.

In the case where the temperature of the investigated surface is higher than the temperature of the surrounding, the theoretical radiative flux Φ_i^{th} received by a multispectral pyrometer is:

$$\Phi_i^{th} = H_i \int_{\Delta\lambda} f_i(\lambda)\varepsilon(\lambda,\theta,\varphi,T)I^0(\lambda,T)d\lambda \tag{5.1}$$

where $f_i(\lambda)$ is the spectral transfer function around the i^{th} wavelength given by manufacturer data, H_i is an amplitude correction obtained after calibration with a blackbody (this point is discussed later), $\varepsilon(\lambda,T)$ is the emissivity depending on direction (θ,φ), wavelength (λ), and temperature (T), I^0 is the intensity given by Planck's law (5.2) or Wien's approximation (5.3) [Ozisik 1973][Sparrow 1978][Siegel 1992] [Modest 2003]. The transfer function $H_i(\lambda)$ is estimated through calibration with a blackbody, it considers spectral and geometrical aspects (*i.e.* solid angle, transmittance of the optics given by manufacturers) of radiative flux between the surface to the pyrometer. Since the measurement is never strictly monochromatic, the flux expressed in watt is obtained by integration in the narrow spectral domain $\Delta\lambda$ around the i^{th} wavelength.

$$I^0(\lambda,T) = \frac{2h_P c^2}{\lambda^5\left(e^{\frac{h_P c}{k_b \lambda T}} - 1\right)} \tag{5.2}$$

$$I^0(\lambda,T) = \frac{2h_P c^2}{\lambda^5} e^{-\frac{h_P c}{k_b \lambda T}} \tag{5.3}$$

In Eqs. (5.2) and (5.3), $h_P = 6.662 \times 10^{-34}$ J·s, $k_b = 1.38 \times 10^{-23}$ J·K^{-1}, and $c = 3 \times 10^8$ m·s^{-1} are Planck's constant, Boltzmann's constant, and light speed, respectively [Ozisik 1973][Sparrow 1978][Siegel 1992][Modest 2003].

It is common to simplify Eq. (5.1) by Eqs. (5.4)-(5.6) in order to help the calculation and be less time consuming [Pierre 2023].

$$\Phi_i^{th} \approx F_i\ \varepsilon(\lambda_i,\theta,\varphi,T)\ I^0(\lambda_i,T) \tag{5.4}$$

$$F_i = \int_{\Delta\lambda} f_i(\lambda)H_i d\lambda \tag{5.5}$$

$$\lambda_i = \frac{\int_{\Delta\lambda} f_i(\lambda)\lambda d\lambda}{\int_{\Delta\lambda} f_i(\lambda)d\lambda} \tag{5.6}$$

During experiments when the position of the pyrometer is fixed, in Eq. (5.4), the emissivity is independent of direction for every radiative flux measured at each wavelength. But this property depends on wavelength and temperature.

Therefore, in the case of a pyrometer able to separate the received flux in N separated quasi-monochromatic fluxes, for a given surface at temperature T, the system to be solved is the following [Pierre 2022]:

$$\begin{aligned} \Phi_1^{th} &\approx F_1\, \varepsilon(\lambda_1, \theta, \varphi, T)\, I^0(\lambda_1, T) \\ &\vdots \\ \Phi_N^{th} &\approx F_N\, \varepsilon(\lambda_N, \theta, \varphi, T)\, I^0(\lambda_N, T) \end{aligned} \tag{5.7}$$

where there is systematically N equations and $N+1$ unknowns: N radiative properties of emission and the temperature. The system is thus ill-posed since underdetermined, whatever the temperature of the investigated surface is constant or variable. Simultaneous estimation of temperature and emissivity is now a centenary problem [Campbell 1925] and publications dealing with this are numerous, but there is no absolute methodology unanimously accepted. A common way to circumvent this underestimation problem is the use of a spectral emissivity model defined with a restricted number of $\widetilde{N}$ - 1 coefficients. Therefore, the minimum number of wavelengths is $\widetilde{N}$. Model describing emissivity is unknown *a priori*, so it should be a pragmatic choice considering the nature of the targeted material and the working spectral range of the pyrometer. Besides the problem of emissivity model, the contradictory debates concern two points: i) the number of wavelengths; ii) and their position, that is discussed in Section 5.2.

5.1.2. The radiative and the photonic fluxes

In terms of observable, two types of signals are possible in multispectral pyrometry: *radiative flux* expressed in watt and *photonic flux* expressed in photons·s^{-1}. The former is measured generally by photon detectors, which have a working spectral range between 1.50 µm and 40.00 µm (Figure 1 [Audaire 2000]) "absorbing the energy of the incident radiation with their electrons by producing free charge carriers" [Modest 2003]. The latter is measured through photomultiplier tubes (PMTs) of working spectral range between 0.15 µm and 2.00 µm (Figure 5.2 [Audaire 2000]): "they detect light by making use of the external photoelectric effect or namely the phenomenon in which electrons are released into the vacuum when light strikes a metal or semiconductor in a vacuum" [www.hamamatsu.com].

Introducing photon energy Eq. (5.8), a monochromatic photonic flux density expression can be obtained Eq. (5.9). The sensor being able to investigate surface with emissivity, the emitted photonic flux is given by Eq. (5.10).

$$E_\lambda = \frac{h_P c}{\lambda} \tag{5.8}$$

$$\mathcal{p}_\lambda^0 = \frac{I^0(\lambda, T)}{E_\lambda} \tag{5.9}$$

$$\mathcal{P}_i^{th} \approx F_i \, \varepsilon(\lambda_i, \theta, \varphi, T) \mathcal{p}_\lambda^0(\lambda_i, T) \tag{5.10}$$

The use of photonic flux by spontaneous emission of the surface is not as widespread as radiative flux (the stimulated photonic emission is not concerned here). This is an alternative solution when the signal-to-noise ratio is too weak during radiative fluxes measurements. This generally concerns UV-visible range and therefore implies mostly applications where the temperatures exceed 1 000 °C [Hervé 1988][Hervé 1991][Ohji 1995][Hervé 2001][Pierre 2008]. There are two advantageous aspects by working with shorter wavelengths: i) there is a high sensitivity on the left increasing part of Planck's law; ii) emissivity tends to show less variation.

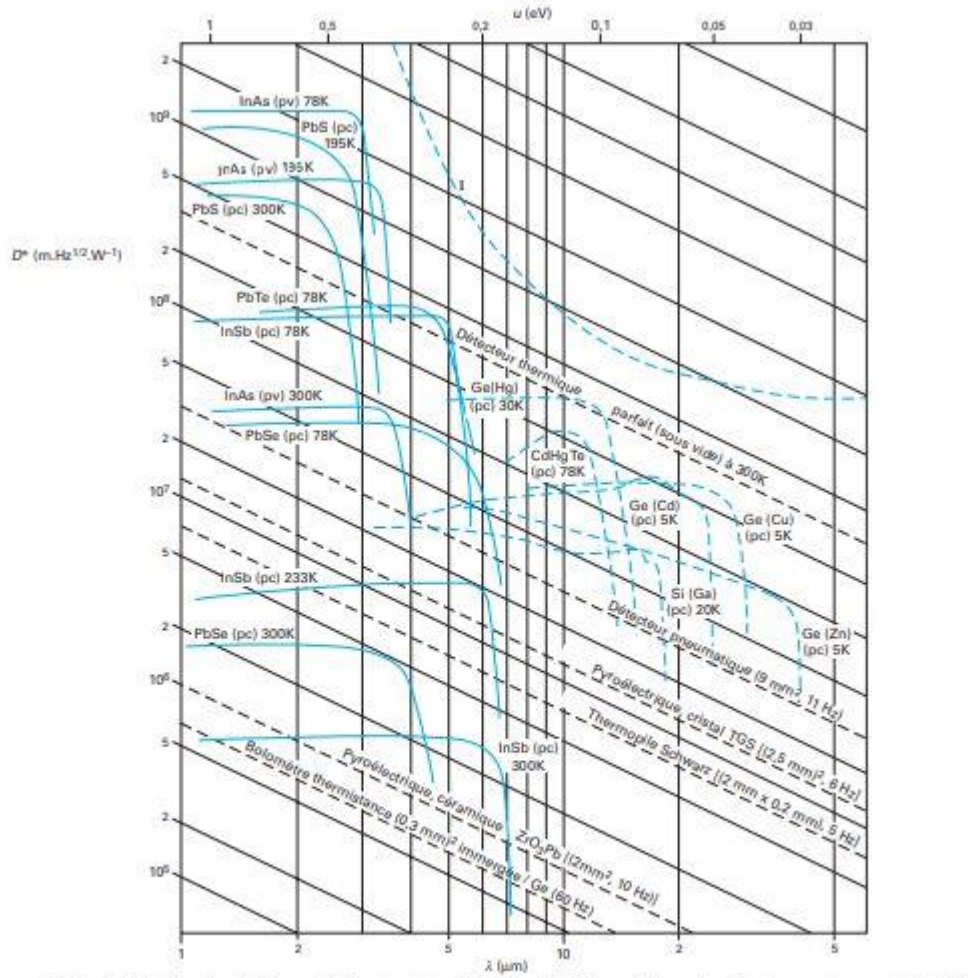

Figure 5.1. Specific detectivity of infrared detectors over the wavelength and photon energy [Audaire 2000].

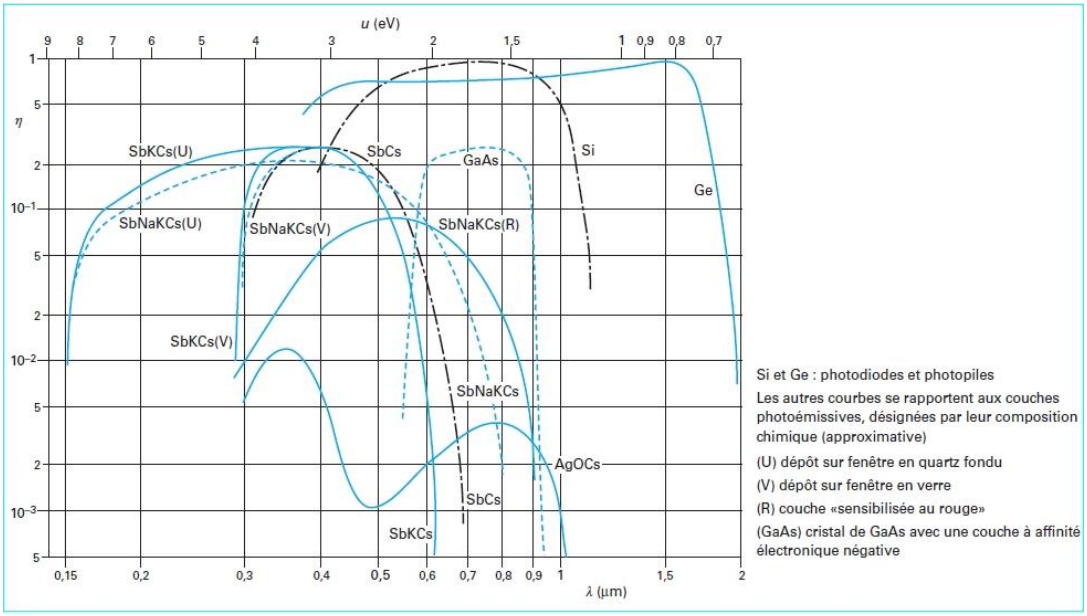

Figure 5.2. Quantum efficiency η of photodetectors over wavelength λ (lower scale) and photon energy u (upper scale) [Audaire 2000].

Figure 5.3 presents evolution of spectral photonic flux P_λ^0 over temperature emitted by a surface $s = \pi\lambda^2/4$ and for different values of wavelength λ of measurement. The detector is assumed perfect with a quantum efficiency of 100 %.

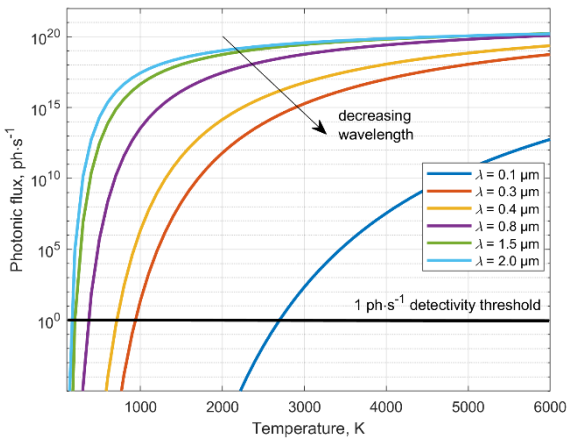

Figure 5.3. Photonic flux emitted from a surface of the size of the detection wavelength versus temperature.

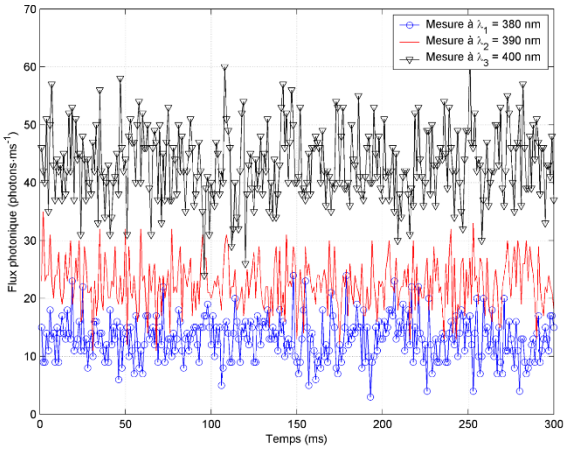

Figure 5.4. Photonic fluxes measured at three wavelengths and for a blackbody temperature of 1 000 K [Pierre 2008].

The detectivity threshold of 1 photon·s^{-1} is reached for a temperature of 711 K for $\lambda = 0.4$ µm. It is necessary to have a minimum of 10 ph·s^{-1} to have exploitable results.

Indeed, spontaneous photonic emission of a surface is a random phenomenon, that is easily exploited through Poisson's law and Gaussian's law. Figure 5.4 presents three photonic fluxes measured at wavelengths 0.38 µm, 0.39 µm and 0.40 µm from the spontaneous emission of a blackbody set at the temperature of $T_c = 1\,273$ K [Pierre 2008] (Figure 5.5). Gaussian's law allows to estimate statistical parameters such as an average photonic flux P_i^{exp} and its standard deviation σ_i^{exp} (Figure 5.6). Measurements are presented in steady-state, and estimation only concerns temperature, which is known thanks to a thermocouple placed in the blackbody. Then the methodology has been extended to transient measurements with the same blackbody and the same wavelengths [Pierre 2016]. In this case, the temperature is not estimated at each time step $\delta t = 10$ ms, but every 500 ms with average fluxes in order to lower the noise (Figure 5.7). Figure 5.7 presents the evolution of the photonic fluxes ratios over time, which is important for the temperature estimation using bispectral pyrometry (see Section 5.2.1) as it is presented in Figure 5.8. Since when temperature is not well-estimated, it means that it is too close from 1.

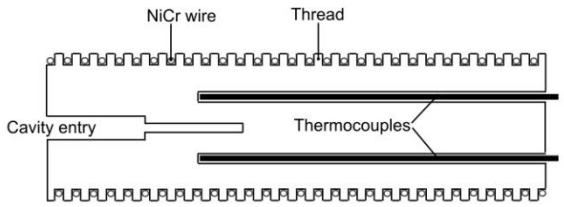

Figure 5.5. Blackbody dedicated to high temperature measurements [Pierre 2008].

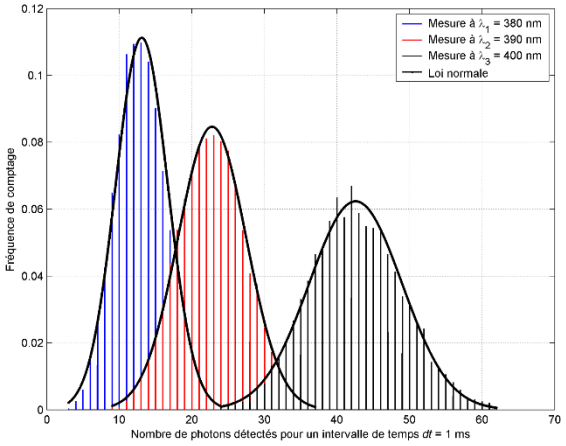

Figure 5.6. Statistical distributions of photonic fluxes with Gaussian's law [Pierre 2008].

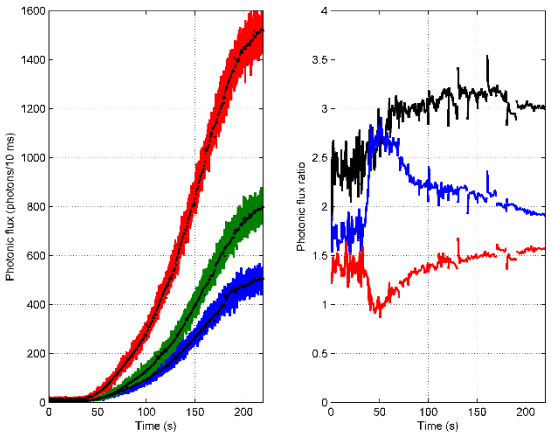

Figure 5.7. Dynamic photonic fluxes measured with the blackbody (left); flux ratios (right) [Pierre 2016].

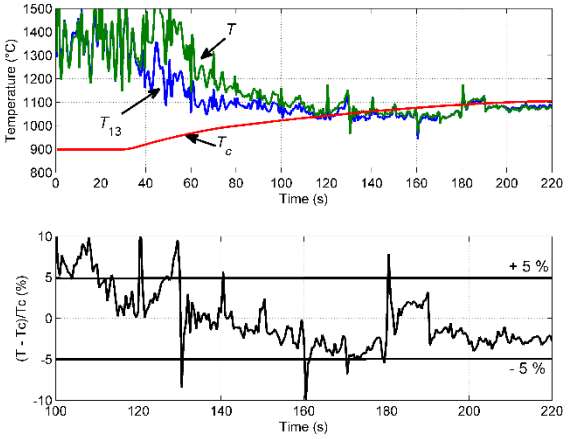

Figure 5.8. Up: temperature estimation T and thermocouple temperature T_c versus time; down: temperature error e_T [Pierre 2016].

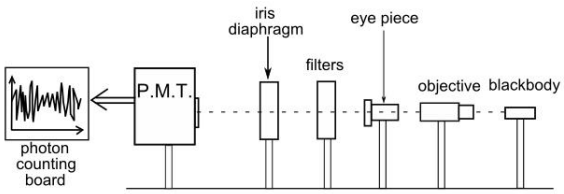

Figure 5.9. Optical experimental bench general view [Pierre 2008].

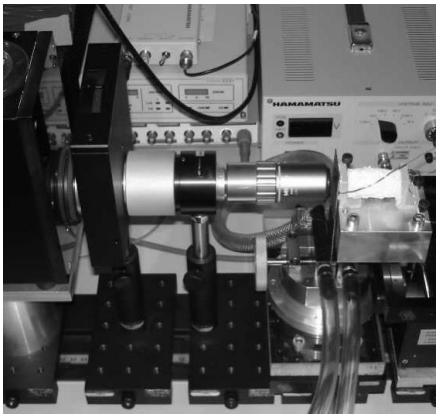

Figure 5.10. Optical experimental bench [Pierre 2008].

5.1.3. The calibration

Figures 5.9 and 5.10 present the global view of the apparatus dedicated to the temperature measurement at microscopic scale using photonic flux. This apparatus has only been tested with a blackbody, which has been specifically developed for this application and for the calibration of the pyrometer. In a general way, whatever the type of detector, it is necessary to calibrate it in the same configuration as the experiment, keeping still the solid angle between the targeted surface and the pyrometer.

Two specific experimental apparatuses have been developed to characterize the physical properties of liquid metals (Section 6). Indeed, IRDL laboratory works for more

than twenty years on high temperature industrial processes such as welding (wire arc additive manufacturing [Cadiou 2020], resistance spot welding [Geslain 2018]) by developing numerical simulations. During these processes, matter changes of state from solid to vaporization, and along this large span of temperature, matter properties vary and must be known to feed the numerical simulations. One of the experimental apparatus is based on the aerodynamic levitation of a metallic sample heated by a laser, and is presented in detail in Section 6 (Figure 5.11), the second one is also presented in the same Section 6. Among all the present instrumentation dedicated to the physical characterization of the liquid metal (thesis of D. Le Maux [Le Maux 2019][Le Maux 2022][Le Maux 2023][Houssein 2023]), five of them are dedicated to radiative flux measurement:

- A six-wavelength pyrometer developed in laboratory: [0.48 µm – 1.55 µm];
- A high-speed camera Phantom VEO-E 310L: [0.4 µm – 1.0 µm];
- A narrow-band pyrometer Lumasense IS6: [0.7 µm – 1.1 µm];
- A bichromatic pyrometer Lumasense ISR6: 0.90 µm and 1.05 µm;
- A bichromatic pyrometer Optris CTratio: 1.45 µm and 1.75 µm.

The six-wavelength pyrometer has been developed for simultaneous temperature emissivity estimation [Dejaeghere 2016][Dejaeghere 2018][Pierre 2022][Pierre 2023][Lamien 2023] (Figure 5.12). The high-speed camera is used at the same time for the observation of the sample [Houssein 2023] (Section 6) and for the measurement of its temperature. The last three pyrometers are strictly used to indicate temperature of liquid sample, and when it is necessary as references. The operation of these three pyrometers is not presented here, but they have been calibrated by manufacturer. It has been a requirement too to calibrate the six-wavelength pyrometer and the high-speed camera: the former with a blackbody, the latter with the help of the solidification temperature of pure iron.

The calibration of the six-wavelength pyrometer has been performed by replacing the nozzle of the levitation by a blackbody (red rectangle in Figure 5.11). The blackbody is made of carbon and its dimensions are: 8.00 mm of height, hole radius of $r = 0.75$ mm and depth of $\ell = 4.00$ mm (Figure 5.13). Considering these dimensions, literature proposes two ways to calculate the apparent emissivity ε_a of the open upper surface: Eq. (5.11) has been proposed by [Bauer 1971] and [Hartmann 2009]; Eq. (5.12) is taken from [Pierre 2007] –demonstration of this relation was given as an exercise proposed to

students, of the very old times I suggest, during radiative transfer classes at the Mines de Nancy!

$$\varepsilon_a = 1 - \frac{1-\varepsilon_w}{\varepsilon_w}\frac{1}{1+\left(\frac{\ell}{r}\right)^2} \tag{5.11}$$

$$\varepsilon_a = \frac{2\sqrt{\varepsilon_w}}{1+\sqrt{\varepsilon_w}} \tag{5.12}$$

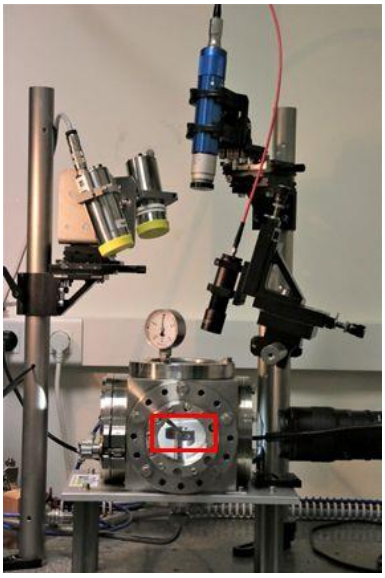

Figure 5.11. Aerodynamic levitation apparatus.

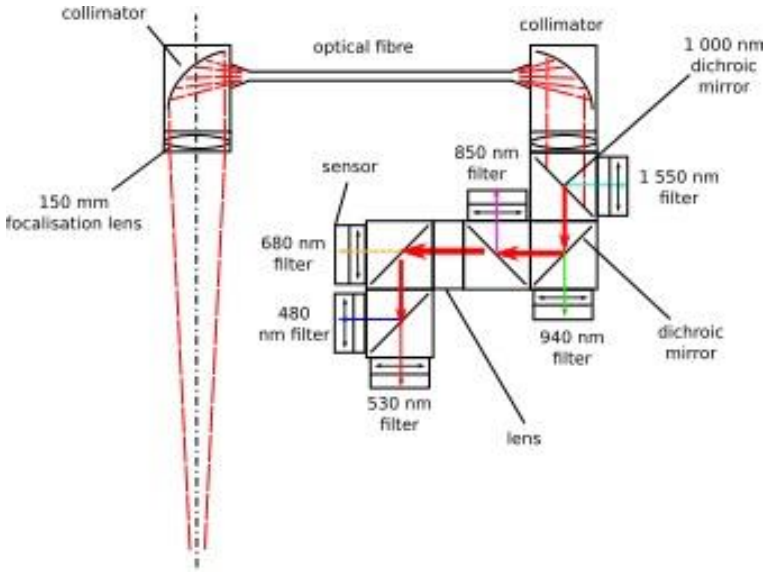

Figure 5.12. Sketch of the six-wavelength pyrometer.

In Eqs. (5.11) and (5.12), ε_w is the wall emissivity, meaning emissivity of the inner of the blackbody. In both cases, using aforementioned dimensions of the blackbody, apparent emissivity is 0.996 and 0.974, respectively, with Eq. (5.11) and Eq. (5.12).

First it is necessary to detail the components of the pyrometer. According to Figure 5.12, it is composed of optical lenses (of transmittivity τ_l), collimators (τ_c), optical fibre (τ_{of}), dichroic mirrors (of transmittivity τ_m and reflectivity ρ_m) splitting radiative fluxes for a given cut-off wavelength λ_c when receiving a radiative flux with an angle of 45°, quasi-monochromatic spectral filters (τ_f), and silicon sensors working in specific narrow spectral band. The value of the central wavelength of the six quasi-monochromatic spectral filters are 0.480 µm, 0.530 µm, 0.680 µm, 0.850 µm, 0.940 µm, and 1.550 µm (Figure 5.12). Each component has its own transfer function over the wavelength given by manufacturers and the global spectral function of each optical path is:

$$f_6(\lambda) = \tau_l\, \tau_c\, \tau_{\lambda f}\, \tau_c\, \rho_{m1}\, \tau_{f6} = \tau_{input}\, \rho_{m1}\, \tau_{f6} \quad (5.13)$$

$$f_5(\lambda) = \tau_{input}\, \tau_{m1}\, \tau_{m2}\, \tau_{f5} \quad (5.14)$$

$$f_4(\lambda) = \tau_{input}\, \tau_{m1}\, \rho_{m2}\, \rho_{m3}\, \tau_{f4} \quad (5.15)$$

$$f_3(\lambda) = \tau_{input}\, \tau_{m1}\, \rho_{m2}\, \tau_{m3}\, \tau_{m4}\, \tau_{f3} \quad (5.16)$$

$$f_2(\lambda) = \tau_{input}\, \tau_{m1}\, \rho_{m2}\, \tau_{m3}\, \rho_{m4}\, \tau_{m5}\, \tau_{f2} \quad (5.17)$$

$$f_1(\lambda) = \tau_{input}\, \tau_{m1}\, \rho_{m2}\, \tau_{m3}\, \rho_{m4}\, \rho_{m5}\, \tau_{f1} \quad (5.18)$$

Figure 5.14 presents the evolution of the six spectral transfer functions (5.13)-(5.18) over wavelength according to manufacturer data. It appears that transfer function $f_1(\lambda)$ has a very low value: this is due to the dichroic mirror m_1, which has a transmittivity τ_{m1} close to zero before 0.500 µm. Secondly, these spectral transfer functions are used to determine a representative wavelength of the filter λ_i according to Eq. (5.6). But this transfer function $f_i(\lambda)$ is not enough, since it does not consider geometric aspects of radiative transfer such as view factors. Only calibration with a blackbody makes possible the determination of one definitive transfer function specific to every optical path, called F_i in Eqs. (5.4) and (5.5).

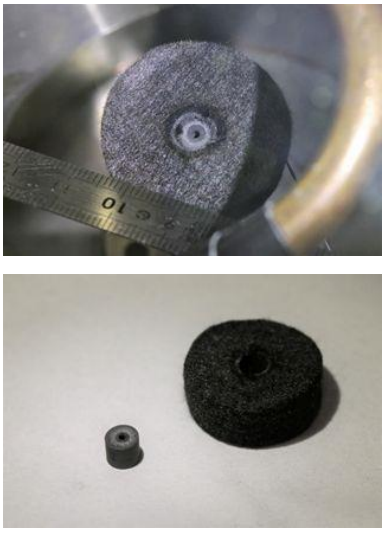

Figure 5.13. Views of the blackbody for the levitation apparatus.

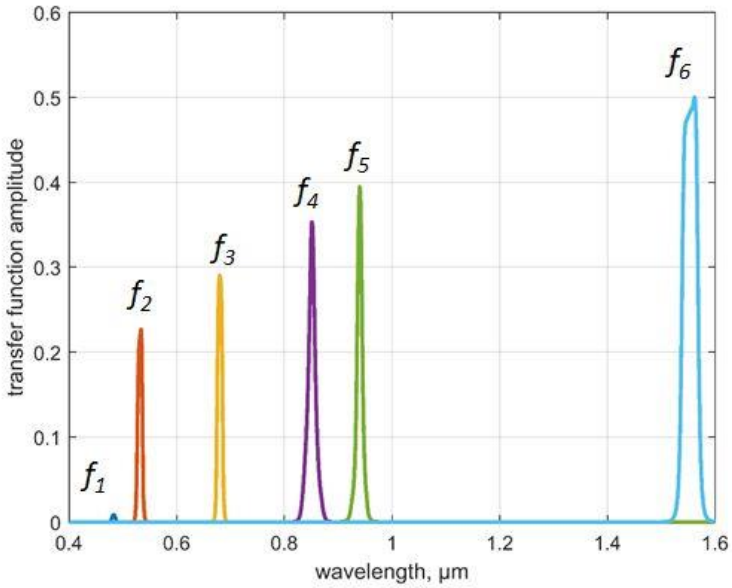

Figure 5.14. Evolution of the six transfer functions according to manufacturer data.

During calibration, both the monochromatic and the bichromatic pyrometers have been placed with the six-wavelength pyrometer according to Figure 5.11. The emissivity

of the blackbody is ε_a (5.19), (5.11), and (5.12). Figure (5.15) presents the evolution of the six radiative fluxes measured by the six-wavelength pyrometer and the temperature given by both commercial pyrometers, which give the same temperatures T^{exp} (5.20). The recording was only possible during the cooling stage of the blackbody due to the perturbation of the laser during the heating period. Indeed, the wavelength of the laser of 1.070 µm disturbs all the pyrometers when it is switched on. Figure 5.15 mentions the threshold of detectivity of the silicon sensors at 50 nW. Therefore, the signals under this limit are not considered. Difference between experimental radiative fluxes and theoretical ones (5.21) is performed in order to estimate the six transfer functions F_i. Evolutions of F_i are presented in Figures 5.16 to 5.21.

$$\varepsilon(\lambda_i, \theta, \varphi, T) = \varepsilon_a \tag{5.19}$$

$$T_{mono} = T_{bi} = T^{exp} \tag{5.20}$$

$$\min\left[\Phi_i^{exp} - \Phi_i^{th}(F_i|\lambda_i, T^{exp})\right] \tag{5.21}$$

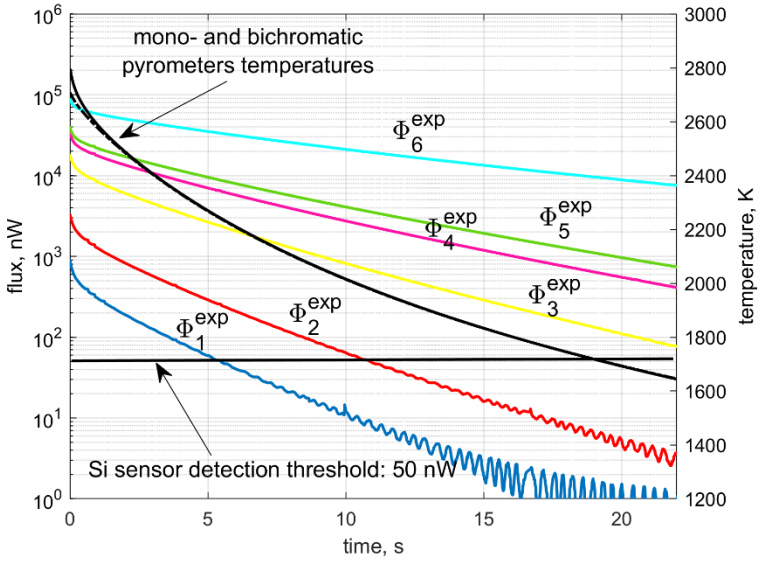

Figure 5.15. Evolutions of the six-wavelength pyrometer fluxes and of the mono- and bichromatic pyrometers temperatures over time during calibration with the blackbody in the levitation apparatus.

Evolutions of F_i do not present an immediate constant value. When the laser is turned off, it takes about 2 s to have the blackbody that behaves like a lumped body.

In Figures 5.16 to 5.18 mainly, it is noticeable that the values of F_i oscillate. This is probably due to natural convective effects. Indeed, the blackbody is the only heated part in the inert chamber (Figure 5.11). As the surrounding is at room temperature, large

temperature difference between the surrounding and the blackbody induces air movement and thus natural convection at the upper surface of the blackbody, which is detected by the pyrometers.

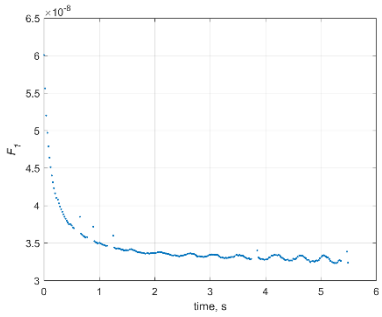

Figure 5.16. Estimation of F_1 over time with Eq. (5.21).

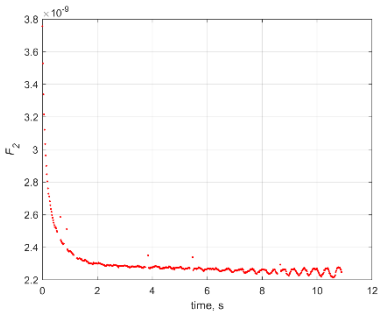

Figure 5.17. Estimation of F_2 over time with Eq. (5.21).

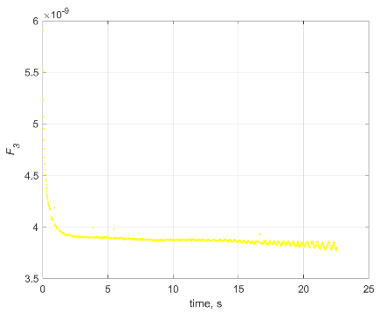

Figure 5.18. Estimation of F_3 over time with Eq. (5.21).

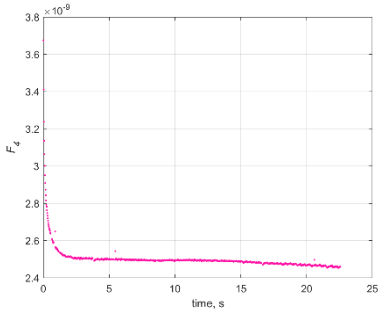

Figure 5.19. Estimation of F_4 over time with Eq. (5.21).

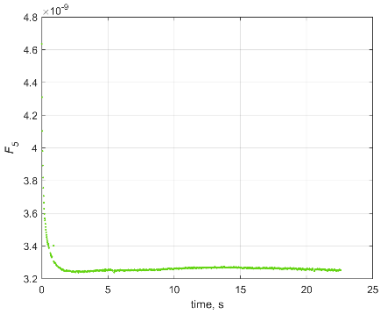

Figure 5.20. Estimation of F_5 over time with Eq. (5.21).

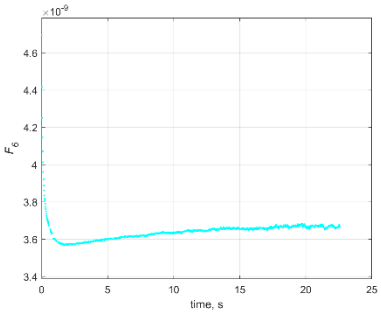

Figure 5.21. Estimation of F_6 over time with Eq. (5.21).

Finally, considering the last stable values of the estimated F_i coefficients, statistical treatment is operated to calculate average value and standard deviation of the F_i. Figures 5.22 to 5.27 and Table 5.1 gather final results of the six transfer functions. The characteristic wavelength λ_i of every flux determined through Eq. (5.6) and Eqs. (5.13)-(5.18) are also presented in Table 5.1.

Table 5.1. Characteristic wavelengths λ_i and transfer functions F_i estimation.

i	1	2	3	4	5	6
Average $F_i \times 10^9$	33.060	2.279	3.899	2.502	3.249	3.592
Standard deviation $\sigma_{F_i} \times 10^9$	0.330	0.011	0.013	0.005	0.005	0.009
Average λ_i (µm)	0.483	0.532	0.680	0.851	0.940	1.554

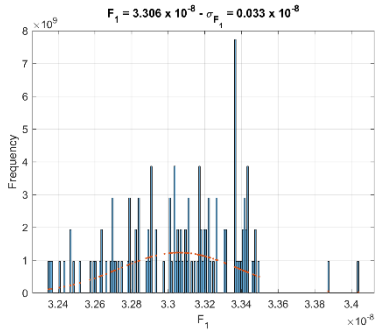

Figure 5.22. Statistical treatment of F_1.

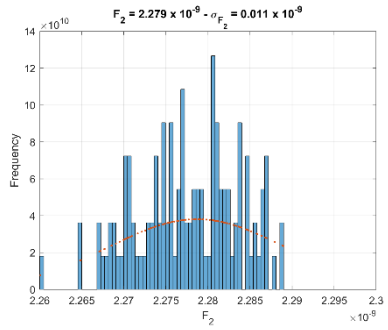

Figure 5.23. Statistical treatment of F_2.

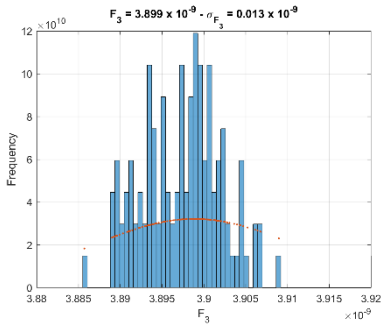

Figure 5.24. Statistical treatment of F_3.

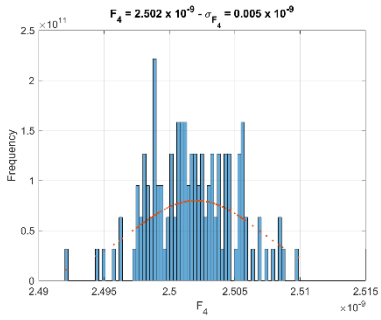

Figure 5.25. Statistical treatment of F_4.

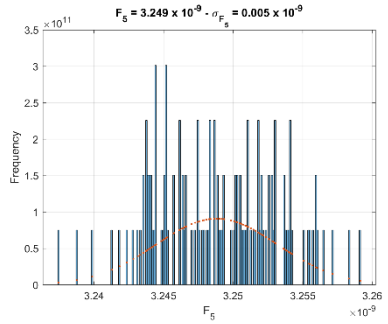

Figure 5.26. Statistical treatment of F_5.

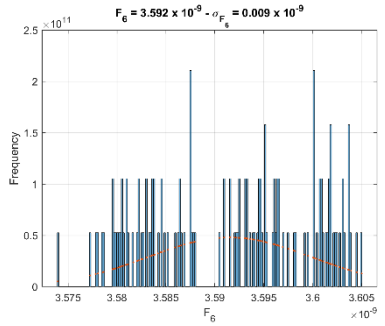

Figure 5.27. Statistical treatment of F_6.

Calibration of the high-speed camera is different. It is not based on the use of a blackbody where the temperature is known and the emissivity is assumed so, but with melting temperature of pure metal, iron in our case, and emissivity extracted from literature [Muller 2012][Houssein 2023]. The entire experiment is presented in Section 6. The basic idea of the calibration is to express a linear relation between greyscale S_{GS} and a parameter X depending on temperature and emissivity (5.22). The parameter X defined in Eq. (5.23) depends on the transmittivity of the camera lens τ and an optical parameter D, as discussed later in this manuscript. These parameters are given by manufacturer.

$$S_{GS} = kX + d \tag{5.22}$$

$$X = \varepsilon\, I^0(T)\, \tau\, 10^{-D} \tag{5.23}$$

$$I^0(T) = \int_{\Delta\lambda} I_\lambda^0(T) d\lambda \approx\ c_0 I_{\lambda_0}^0(T) \tag{5.24}$$

Intensity $I^0(T)$ expressed in Eq. (5.23) is calculated from Eq. (5.24) considering Planck's laws $I_\lambda^0(T)$ and $I_{\lambda_0}^0(T)$, where λ_0 is the characteristic wavelength of the camera in its working spectral range $\Delta\lambda$ and c_0 a coefficient. The combination of Eqs. (5.22)-(5.24) allows to express explicitly the temperature:

$$T = \frac{h\,c}{k\,\lambda_0}\, ln\left[\frac{c_0\, k\, \varepsilon\, \tau\, 10^{-D}}{S_{GS} - d} + 1\right]^{-1} \tag{5.25}$$

Parameters c_0 and λ_0 are first determined either using Wien's approximation by linearization (5.26) or Planck's law by minimization (5.27) considering a fixed temperature range. The choice of the temperature modifies the values of c_0 and λ_0 when using Wien's approximation, but not with Planck's law due to the product $\lambda_0 T$ that increases. For example, in Figure 5.28, evolution of both parameters is plotted considering a fixed minimal temperature of 1 000 K and a changing maximal temperature between 1 500 K and 2 500 K, which represents approximately the temperature range of the experiments performed and presented in Section 6.

$$\ln[\, I^0(T)] = -\frac{hc}{k\lambda_0 T} + \ln(c_0) - 5\ln(\lambda_0) \tag{5.26}$$

$$\frac{c_0 \lambda_0^{-5}}{I^0(T)} + 1 - e^{\frac{hc}{k\lambda_0 T}} \to 0 \tag{5.27}$$

Finally, the last parameters to estimate to complete the calibration are k and d in Eq. (5.25). Experimentally, the protocol consists in measuring the greyscale signals S_{GS} at the melting/solidification plateaus of pure metals assuming known their emissivity, coefficient τ and for different values of D. The tested metal is iron ($T_{fusion} = 1\,811$ K) and its emissivity is assumed 0.3 during the phase changes [Watanabe 2003]. Eight measurements have been performed and linear evolution of S_{GS} versus X is presented in Figure 5.29. Therefore, using equation mentioned in Figure 5.29, temperature T can directly be calculated from Eq. (5.25) for a given emissivity.

5.1.4. Partial conclusion

This section was dedicated to the presentation of basics in multispectral pyrometry and of different types of fluxes: radiative or photonic, and calibration. Considering temperature measurement with a multispectral pyrometer with N fluxes measured at N different wavelengths, by principle the problem is always ill-posed since there are always N equations and $N+1$ unknowns: one temperature and N emissivities. And it comes out that, once identified and estimated the maximum of uncertainty sources, the most important problem is the knowledge of the emissivity. This parameter is naturally present in each radiative flux and happens to be unpredictable most of the time, depending on numerous other parameters. The next section is dedicated to the selection of the wavelengths in the case where pragmatic choice of the emissivity model is made to set multispectral pyrometry.

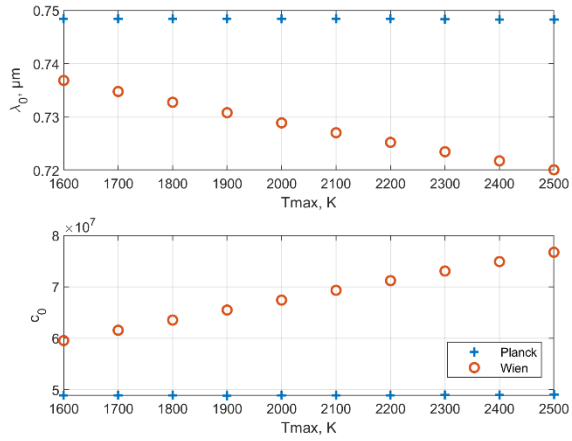

Figure 5.28. Values of coefficients c_0 and λ_0 for different temperature ranges.

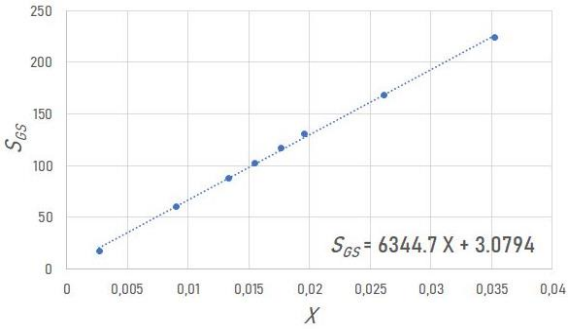

Figure 5.29. Calibration curve of the high-speed camera.

5.2. The selection of the wavelengths

Once established a likely emissivity model in the working spectral range of the detector, the next question deals with the number N of the wavelengths λ_i, their position, and the distance between two consecutive ones λ_i and λ_j. So far, no absolute methodology exists and discussions concern mainly the number of wavelengths to use with contradictory advices [Nordine 1986][Krapez 2011][Araújo 2017] [Krapez 2019].

5.2.1. Bispectral wavelengths selection

It has been said in Section 5.1 that the system to solve in multispectral pyrometry is underdetermined since there is always $N+1$ unknown and N equations (5.7). This problem disappears when an emissivity model is chosen: the minimum number of wavelengths corresponds to the number of parameters of the emissivity model plus the temperature. For example, for a first order polynomial emissivity model, a minimum of three wavelengths is required.

Manufacturers propose monochromatic, bispectral, monoband, multispectral, hyperspectral pyrometers… The selection of the pyrometer is sometimes difficult, it depends on the measured temperature range. It is also possible to develop a home-made pyrometer, as it was the case in my PhD [Pierre 2007] and during the PhD of L. Dejaeghere [Dejaeghere 2016]. In this last case, the choice of the wavelengths has been done regarding the following criteria:

- temperature uncertainty;
- fluxes ratio.

Let express the simplest case of bispectral pyrometry assuming Wien's approximation, the temperature and its uncertainty are explicitly given by:

$$T = \frac{C_2(\lambda_2^{-1} - \lambda_1^{-1})}{ln\left[\frac{\Phi_1^{exp}}{\Phi_2^{exp}}\frac{F_2}{F_1}\frac{\varepsilon_{\lambda_2}}{\varepsilon_{\lambda_1}}\left(\frac{\lambda_2}{\lambda_1}\right)^{-5}\right]} \tag{5.28}$$

$$\frac{e_T}{T} = \frac{\frac{e_{\lambda_1}}{\lambda_1}\left|5 - \frac{C_2}{\lambda_1 T} - \frac{\lambda_1}{\varepsilon}\frac{d\varepsilon}{d\lambda}\right| + \frac{e_{\lambda_2}}{\lambda_2}\left|5 - \frac{C_2}{\lambda_2 T} - \frac{\lambda_2}{\varepsilon}\frac{d\varepsilon}{d\lambda}\right| + \frac{e_{\Phi_1^{exp}}}{\Phi_1^{exp}} + \frac{e_{\Phi_2^{exp}}}{\Phi_2^{exp}}}{\frac{C_2}{T}\left|\frac{1}{\lambda_1} - \frac{1}{\lambda_2}\right|} \tag{5.29}$$

$$\varepsilon_{\lambda_2} = \varepsilon_{\lambda_1} + \frac{d\varepsilon}{d\lambda}(\lambda_2 - \lambda_1) \tag{5.30}$$

Eq. (5.30) is first order Taylor's series on emissivity at two positions λ_1 and λ_2, and $C_2 = hc/k_B$. The principle of bispectral pyrometry is to assume a known emissivity ratio. This ratio has a higher probability to be equal to one if wavelengths are getting close to each other. However, experimental radiative fluxes have also a higher probability to become equivalent considering the noise of the signals. Moreover, the relative uncertainty given by Eq. (5.29) tends to infinity if λ_2 gets closer to λ_1. Therefore, in order not to penalize the temperature uncertainty in Eq. (5.30), the following criterion has been imposed [Pierre 2008]:

$$\frac{C_2}{T}\left|\frac{1}{\lambda_1}-\frac{1}{\lambda_2}\right|>1 \tag{5.31}$$

$$\Delta\lambda > \frac{T\lambda_1\lambda_2}{C_2} \tag{5.32}$$

The criterion (5.32) proposes a minimum distance between two consecutive wavelengths. If this criterion is respected between λ_1 and λ_2, for multispectral pyrometry, it is also respected between λ_1 and λ_3... However, between λ_1 and λ_3, the emissivity ratio is likely to be different. Figure 5.30 presents example of evolution of $\Delta\lambda$ versus λ_1 and for different temperatures.

The second criterion presented is based on the radiative fluxes ratio α in the system (5.33)-(5.36) [Pierre 2008]. Still starting from the bispectral case assuming Wien's approximation, and the transfer functions and emissivity ratios equal to one in Eq. (5.28), let x be the wavelength ratio:

$$x^* e^{x^*} = \gamma(\lambda_1) \tag{5.33}$$

$$\gamma(\lambda_1) = -\frac{C_2}{5\lambda_1 T}\frac{1}{\alpha^{1/5}}e^{-\frac{C_2}{5\lambda_1 T}} \tag{5.34}$$

$$x^* = -\frac{C_2}{5\lambda_1 T}x \tag{5.35}$$

$$x^{-5}e^{-\frac{C_2}{\lambda_1 T}(1-x)} = \alpha \tag{5.36}$$

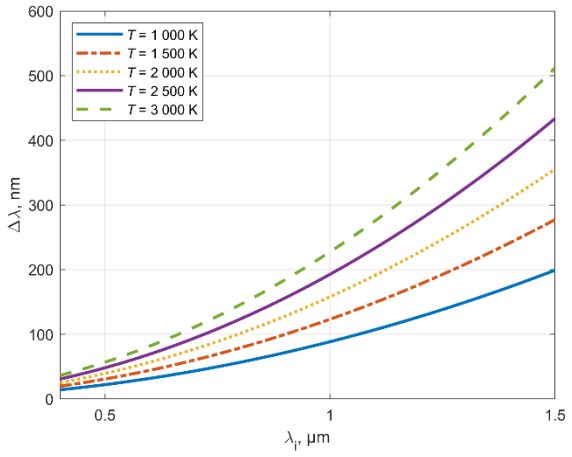

Figure 5.30. Evolution of the wavelength distance $\Delta\lambda = \lambda_2 - \lambda_1$ versus λ_1 for different temperatures.

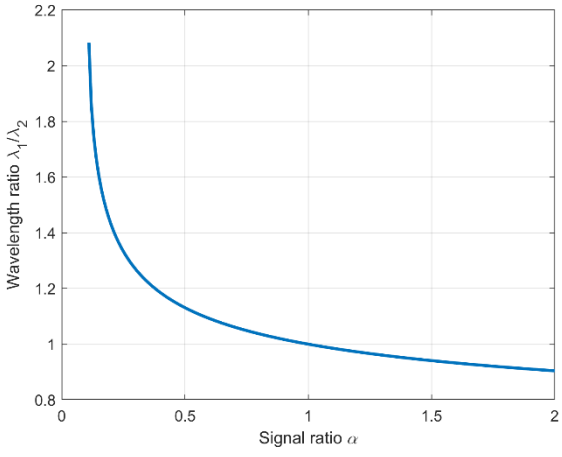

Figure 5.31. Evolution of the wavelength ratio versus signal ratio α for a given temperature of 1 273 K.

For a given temperature and the first wavelength λ_1, Figure 5.31 plots the evolution of the wavelength ratio versus the signal ratio α. Signals are noiseless, but it would be interesting to include this specificity since it is of particular importance for a signal ratio close to unity. Note as a verification that for $\alpha = 1$, $\lambda_1/\lambda_2 = 1$ too.

As an example, Table 5.2 presents a sum up of numerical results in order to check the criteria of Eq. (5.32) considering the six-wavelength pyrometer [Dejaeghere 2018]. Only five wavelengths are here considered: λ_1 to λ_5, and the wavelength of interest is λ_4. For three temperatures T, we can observe that the distance criterion $\Delta\lambda$ is respected between wavelength λ_4 and the other ones except between λ_4 and λ_5, which is too weak implying an amplification of the temperature uncertainty (5.29) with a denominator inferior to 1. The second point is the fluxes ratio α, which is generally quite high, meaning greater than 2, most of the time, except for α_{43} and α_{54}, which are both close to 1 for a temperature of 3 273 K. At this temperature, the wavelength of maximal emission is 0.885 µm. As these three wavelengths are around the maximum of Planck's law, the signal variations are very low. Therefore, assuming that $\varepsilon_{\lambda3}/\varepsilon_{\lambda4}$ and $\varepsilon_{\lambda4}/\varepsilon_{\lambda5}$ are known, bichromatic estimation is not recommended with ratios α_{43} and α_{54} for $T = 3\,273$ K. Moreover, it would be not necessary to use λ_4 and λ_5 in multispectral pyrometry at $T =$ 3 273 K as long as the emissivity model is linear.

Table 5.2. Example of numerical results of radiative fluxes ratio and distance between wavelengths in the case of the six-wavelength pyrometer [Dejaeghere 2018] and presented in Section 5.1.3. Green cells represent cases where the criteria are satisfied contrary to red ones.

T(K)	$\lambda_4 = 0.850$ µm	$\lvert\lambda_4 - \lambda_1\rvert$ = 370 nm	$\lvert\lambda_4 - \lambda_2\rvert$ = 320 nm	$\lvert\lambda_4 - \lambda_3\rvert$ = 170 nm	$\lvert\lambda_5 - \lambda_4\rvert$ = 90 nm
	Eq. (5.32)	α_{41} (5.36)	α_{42}	α_{43}	α_{54}
1 273	64 nm	1 622	289	9	2,2
2 273	115 nm	17	8,5	2,1	1,2
3 273	164 nm	3,1	2,2	1,2	1,0

Table 5.2 shows that the criteria are temperature-dependent and the selection of wavelengths depends on the desired temperature range. The use of the six wavelengths (with the complete pyrometer!) is not systematic for large temperature variation.

Furthermore, one should be careful that a system does not become underdetermined with less wavelengths than parameters to estimate (the emissivity coefficients and the temperature).

5.2.2. Multispectral wavelength selection

From those two previous criteria, the most subjective one remains the fluxes ratio, which depends on the signal-to-noise ratio of each radiative flux. The works of Rodiet *et al.* are interesting, since they try to bring objectivity for the selection of the wavelengths with the use of a minimization of the variance on the estimated temperature in the correlation matrix of the estimated parameters (5.41)-(5.42) by ordinary least squares (5.40) [Rodiet 2016]. They start with linear Wien's approximation (5.37) with $C_1 = 2\pi hc^2$. The wavelengths are progressively estimated assuming first a blackbody emissivity ($N = 1$ and $\boldsymbol{\beta} = T$) for the first wavelength λ_{1opt}, then a grey body emissivity ($N = 2$ and $\boldsymbol{\beta} = [T\ a_0]^T$), then linear emissivity ($N = 3$ and $\boldsymbol{\beta} = [T\ a_0\ a_1]^T$), and finally a parabolic emissivity ($N = 4$ and $\boldsymbol{\beta} = [T\ a_0\ a_1\ a_2]^T$), for, respectively, the three next ones λ_{2opt}, λ_{3opt}, and λ_{4opt}, in a narrow spectral band imposed by infrared camera.

From a given temperature, the first wavelength is estimated considering $\boldsymbol{\beta} = T$ thanks to Eq. (5.41) reduced to a single value σ_T^2 by minimising Eq. (5.40). Considering one single radiative flux Φ_1 and T = 2 273 K, Figure 5.32 plots its evolution versus the wavelength (5.37), meaning Wien's approximation, and its derivative over temperature, $\partial\Phi_1/\partial T$, which maximum has the same wavelength as the minimum of $\sigma_T = f(\lambda)$. Maximum of Wien's approximation is for $\lambda_m T = C_2/5$, with λ_m the wavelength of maximal emission, here equals to 1.266 µm for $T = 2\ 273$ K. Maximum of the derivative corresponds to the wavelength $\lambda_{1opt} = 1.055$ µm, which is the first selected wavelength.

$$\Phi^{th} = \varepsilon(\lambda) C_1 \lambda^{-5} e^{-\frac{C_2}{\lambda T}} \tag{5.37}$$

$$\varepsilon(\lambda) = \sum_{i=2}^{N} a_{i-2} \lambda^{i-2} \tag{5.38}$$

$$\boldsymbol{\beta} = [T, a_0 \dots, a_{N-1}]^T \tag{5.39}$$

$$J = \sum_{i=1}^{N} \left| \Phi_i^{th}(\boldsymbol{\beta}) - \Phi_i^{exp} \right|^2 \tag{5.40}$$

$$\mathrm{cov}(\beta) = \begin{bmatrix} \sigma_T^2 & \mathrm{cov}(T,a_0) & \dots & \mathrm{cov}(T,a_n) \\ \mathrm{cov}(a_0,T) & \sigma_{a_0}^2 & \ddots & \mathrm{cov}(a_0,a_n) \\ \vdots & \vdots & \ddots & \vdots \\ \mathrm{cov}(a_n,T) & \mathrm{cov}(a_n,a_0) & \dots & \sigma_{a_n}^2 \end{bmatrix} = (X^T X)^{-1}\sigma_{noise}^2 \qquad (5.41)$$

$$X = \begin{bmatrix} \frac{\partial \Phi_1}{\partial T} & \frac{\partial \Phi_1}{\partial a_0} & \dots & \frac{\partial \Phi_1}{\partial a_n} \\ \frac{\partial \Phi_2}{\partial T} & \frac{\partial \Phi_2}{\partial a_0} & \dots & \frac{\partial \Phi_1}{\partial a_n} \\ \vdots & \vdots & \vdots & \vdots \\ \frac{\partial \Phi_n}{\partial T} & \frac{\partial \Phi_n}{\partial a_0} & \dots & \frac{\partial \Phi_n}{\partial a_n} \end{bmatrix} \qquad (5.42)$$

The selection of λ_{2opt}, once λ_{1opt} is known, considers the covariance matrix with a dimension 2×2, Eq. (5.38) with $N = 2$ and $\boldsymbol{\beta} = [T\ a_0]^T$. Figure 5.33 plots σ_T over the wavelength, which is minimal for two wavelengths: $\lambda_{2opt}^1 = 0.725$ µm and $\lambda_{2opt}^2 = 1.983$ µm. For example, the second value can be rejected since it is beyond the spectral range of the detector, even if σ_T is smaller at this position than the other one. Thus $\lambda_{2opt} = \lambda_{2opt}^1 = 0.725$ µm. Procedure is repeated for the two last wavelengths and presented in Figures 5.34 and 5.35. Several possibilities are offered and the use of the previous criteria presented in Eq. (5.32) and Eqs. (5.33)-(5.36) can help the choice.

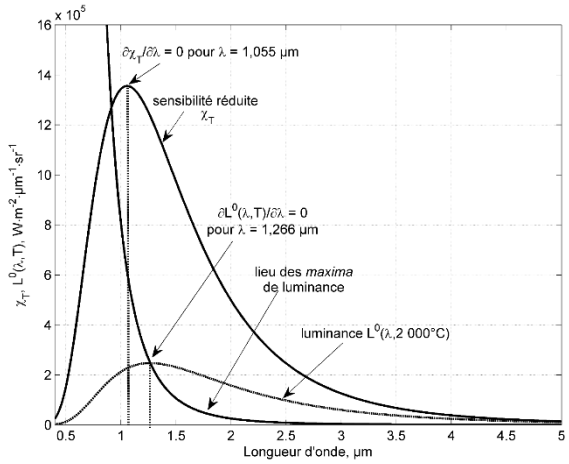

Figure 5.32. Intensity and its spectral derivative over the wavelength. Derivative of the flux gives position of the first wavelength.

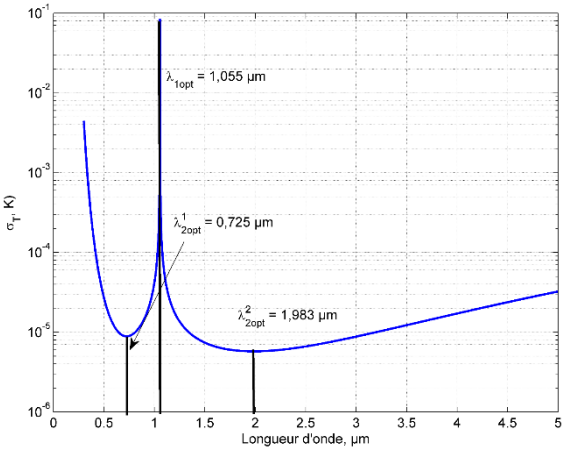

Figure 5.33. Standard deviation on temperature σ_T from Eq. (5.41) versus wavelength for the estimation of the parameter of the constant emissivity model.

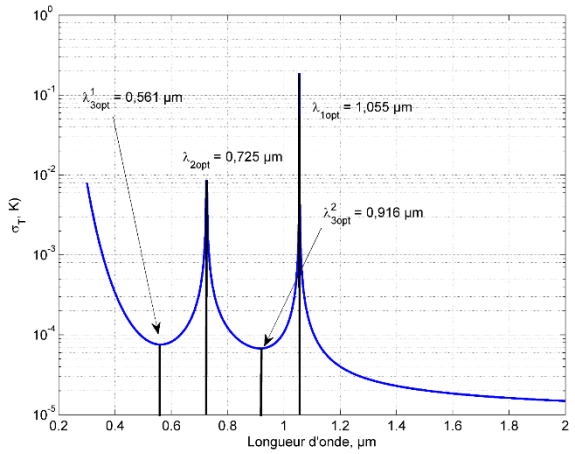

Figure 5.34. Standard deviation on temperature σ_T from Eq. (5.41) versus wavelength for estimation of the second parameter of the linear emissivity model.

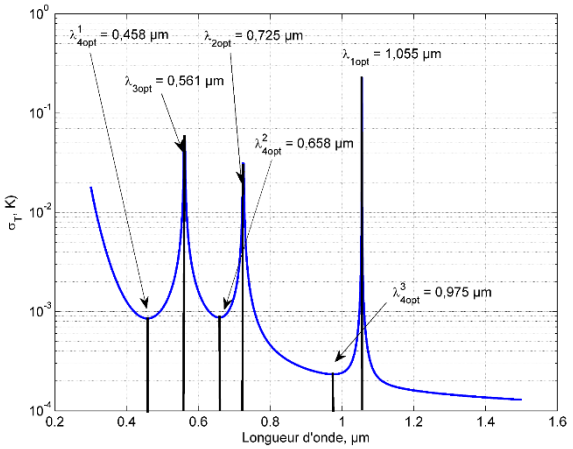

Figure 5.35. Standard deviation on temperature σ_T from Eq. (5.41) versus wavelength for estimation of the third parameter of the parabolic emissivity model.

The methodology proposed by Rodiet *et al.* has been tested with the six-wavelength pyrometer [Pierre 2022][Pierre 2023]. Four wavelengths on six have been selected based on minimization of the temperature variance σ_T^2 assuming a linear emissivity model. Estimation by ordinary least squares gave satisfying results, which are presented in Section 5.3, based on the knowledge on the melting point for pure metal, which has been estimated properly.

5.2.3. Partial conclusion

We presented in Section 5.2 methodologies to select wavelengths for a given temperature assuming a faithful emissivity model. Some of these procedures of selection have the advantage to be based on objective criteria and have the possibility to consider technical and experimental limitations, such as the spectral range of the detector.

The techniques of selection are relevant with the condition that the temperature of the investigation surface does not vary a lot during application. Indeed, the use of pyrometer with chosen fixed wavelengths is limitative and would become inefficient when the signal to noise ratio is too low.

The selection of the wavelengths is based on the choice of a characteristic temperature, which must be an average if the temperature is not constant along the experiment. Therefore, it is important to have a good prior of the temperature range of

the application. Consequently, if it becomes too large, selected wavelengths would not be that optimal and the temperature uncertainty would increase.

Working with a reduced number of wavelengths has the advantage to have a short calculation time compared with measurements with a greater number of wavelengths, but it becomes limited when the temperature range becomes too large. The next section is dedicated to different techniques I experimented for the temperature emissivity estimation based on ordinary least squares or Bayesian inference.

5.3. The simultaneous temperature emissivity estimation

5.3.1. Presentation of the experiment and some previous theoretical considerations

Several techniques to estimate simultaneously temperature and emissivity have been tested during multispectral pyrometry measurements: deterministic ordinary least squares (OLS) [Pierre 2022], and statistic Bayesian MCMC [Pierre 2022][Pierre 2023], and Bayesian particle filters [Lamien 2023]. All of them have been tested with the same experiment with niobium and a mild steel. Only results with niobium are presented here.

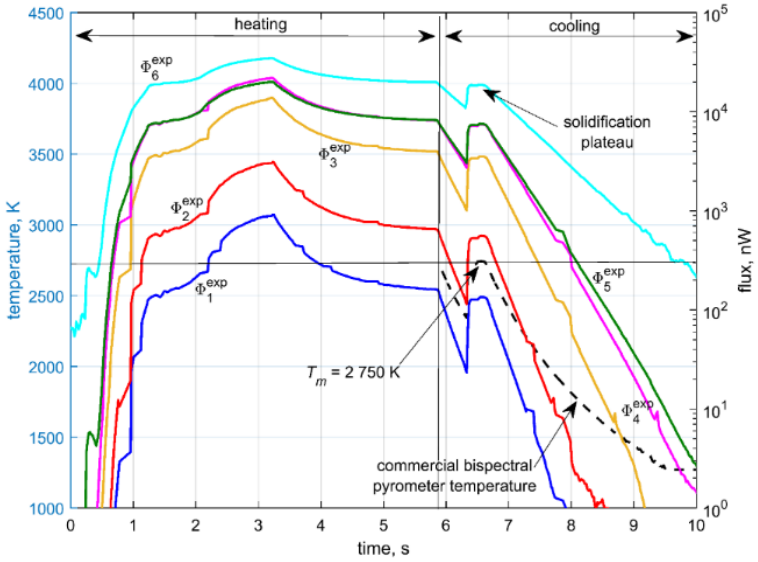

Figure 5.36. Niobium sample fluxes and commercial bispectral pyrometer temperature as a function of time.

Experiments have been performed with the six-wavelength pyrometer. Figure 5.36 plots all the radiative fluxes recorded along one experiment.

Commercial bispectral pyrometer is also used during experiment and gave the temperature (black dashed line in Figure 5.36), only during the cooling stage since the laser wavelength disturbs this pyrometer. This temperature is considered as a reference since the solidification plateau temperature is respected for pure niobium at $T_f = 2\,750$ K.

Figure 5.37 shows at the same time the same radiative fluxes and the laser heating sequence. Both time scales are not synchronized. There are two sequences for the laser heating: one of 140 W during 1 s and a second one of 30 W during 6 s. Considering the radiative fluxes, measurements for only five wavelengths are presented (wavelength $\lambda_1 = 0.480$ µm has been omitted due to its very weak signal). Melting and solidification plateaus and the undercooling are visible. The cooling starts when the laser is off.

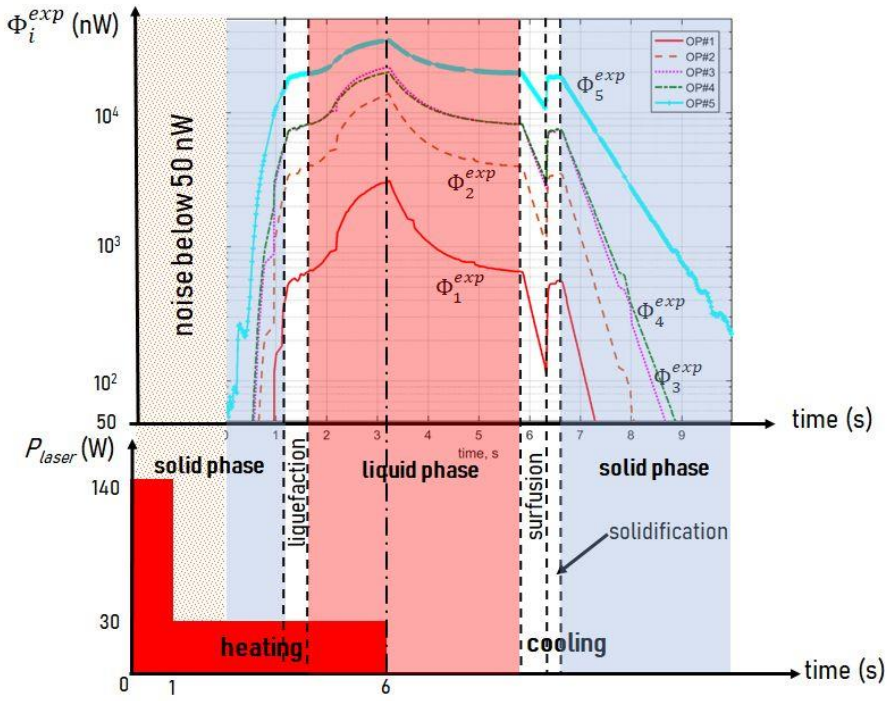

Figure 5.37. Simultaneous presentation of the laser heating sequence and the radiative fluxes measured with five wavelengths on six (wavelength $\lambda_1 = 0.480$ µm has been skipped due to its very weak signal).

Synthesis of the different techniques used to perform simultaneous temperature emissivity estimation is presented in Table 5.3. A first study concerns bispectral pyrometry using OLS, Bayesian inference using Maximum a Posteriori (MAP), and Bayesian inference with Monte Carlo Markov Chains (MCMC) [Pierre 2022]. The second

study is dedicated to multispectral pyrometry with the same experimental data, also using Bayesian inference with particle filter [Pierre 2023][Lamien 2023]. Table 5.3 explains the theoretical model used: Planck's law or Wien's approximation; the emissivity model: constant, linear, even independent; what parameters to estimate; and their prior for Bayesian inference: Gaussian, normal.

Whatever the relation used to express the theoretical flux, Eqs. (5.2) or (5.3), the signal is experimentally contaminated by an additive random noise e_i. Thus, let's define the observable Y_i as following:

$$Y_i = \varepsilon_i(T)\Phi_i^{0,th}(T) + e_i \tag{5.43}$$

where $\Phi_i^{0,th}(T)$ is the blackbody radiative flux. Moreover, Section 5.3.4 presents temperature emissivity estimation through Bayesian technique using linear approximation. Therefore, assuming Wien's approximation (5.3) and introducing mean values λ_i, ε_i and F_i for the wavelength, the emissivity, and the transfer function (see Section 5.1.1), respectively, in each spectral band i, the flux in the band i can thus be simplified to:

$$\Phi_i^{th}(T) = F_i\varepsilon_i C_1 \lambda_i^{-5} e^{-\frac{C_2}{\lambda_i T}} \tag{5.44}$$

Eq. (5.44) can be linearized by taking the logarithm function. This gives the observable Y' :

$$Y_i' \equiv ln\left(\frac{\Phi_i^{th}(T)\lambda_i^5}{C_1 F_i}\right) = ln(\varepsilon_i) - \mu_i \frac{T_{ref}}{T} + e_i' \tag{5.45}$$

The new observables are now $\mathbf{Y}' = [Y_1', Y_2', \dots Y_m']^{\boldsymbol{T}}$ and in Eq. (5.45) μ_i is defined by Eq. (5.46), T_{ref} is an arbitrary reference temperature used for scaling the temperature, e_i' is a Gaussian additive experimental error affecting the observables Y_i', and m is the length of the time step. e_i' differs from e_i because of the linearization.

$$\mu_i = \frac{C_2}{\lambda_i T_{ref}} \tag{5.46}$$

Table 5.3. Synthesis of the techniques used for simultaneous temperature emissivity estimation [Pierre 2022][Pierre 2023][Lamien 2023].

Method		Model	Emissivity	Parameter $\boldsymbol{\beta}$	Priors
bispectral	OLS	Planck	$\varepsilon = a_0$	$[a_0, T]^T$	-
	Bayesian – MAP	Wien	Independent values	$\left[\ln(\varepsilon_i), \ln\left(\varepsilon_j\right), T\right]^T$	Gaussian
	Bayesian – MCMC	Planck	$\varepsilon = a_0$	$[a_0, T]^T$	Gaussian
multispectral	OLS	Pl./Wi.	$\varepsilon = a_0 + a_1\lambda$	$[a_0, a_1, T]^T$	-
	Bayesian – MAP	Wien	Independent values	$[\ln(\varepsilon_1) \ldots \ln(\varepsilon_5), T]^T$	Gaussian
	Bayesian – MCMC (MLE)	Planck	$\varepsilon = a_0 + a_1\lambda$	$[a_0, a_1, T]^T$	Normal
	Bayesian – particle filter	Planck	$\varepsilon = a_0 + a_1\lambda$	$[a_0, a_1, T]^T$	Normal

5.3.2. The bispectral method with ordinary least squares

Fundamentally, the bispectral method consists in estimating temperature by using two radiative fluxes measured at wavelengths $\boldsymbol{\lambda_i}$ and $\boldsymbol{\lambda_j}$. Regarding the spectral emissivity values, one of them is estimated in the same time as temperature, say $\boldsymbol{\varepsilon_i}$ at $\boldsymbol{\lambda_i}$, whereas a functional relationship is assumed between $\boldsymbol{\varepsilon_j}$ (at $\boldsymbol{\lambda_j}$) and $\boldsymbol{\varepsilon_i}$. One possible functional relationship is $\boldsymbol{\varepsilon_j/\varepsilon_i = \xi_{ji}}$ where $\boldsymbol{\xi_{ji}}$ is a predetermined constant. In the classical "greybody" approximation constant $\boldsymbol{\xi_{ji}}$ is set to one, which, to be satisfactory, requires that wavelengths $\boldsymbol{\lambda_i}$ and $\boldsymbol{\lambda_j}$ be not too far from each other (see Section 5.2.1).

Consider two radiative fluxes $\Phi_i^{exp}(T) \equiv Y_i$ and $\Phi_j^{exp}(T) \equiv Y_j$ measured at wavelengths $\boldsymbol{\lambda_i}$ and $\boldsymbol{\lambda_j}$. The method lays on simultaneous temperature emissivity estimation by solving the Eqs. (5.47)-(5.48):

$$\Phi_i^{th}\left(\varepsilon_i, T_{ij}\right) = Y_i \tag{5.47}$$

$$\xi_{ji}\Phi_j^{th}\left(\varepsilon_i, T_{ij}\right) = Y_j \tag{5.48}$$

5.3.3. The multispectral method with ordinary least squares

The proposed method here implies to use experimental flux Y_i according to Planck's law. In order not to amplify the standard deviation on the estimated temperature

and emissivity by multispectral methods, constrains presented in Eqs. (5.31)-(5.36) are used [Rodiet 2013][Pierre 2008][Rodiet 2015][Rodiet 2016]. The objective is to minimize the cost function (5.49), where N is the number of considered wavelengths, Φ_i^{th} is the theoretical flux, and $\boldsymbol{\beta} = [T, a, b]^T$ is the parameter vector of the emissivity model.

$$\sum_{i=1}^{N} \left[\Phi_i^{th}(\boldsymbol{\beta}) - Y_i\right]^2 \tag{5.49}$$

5.3.4. Estimation by Bayesian inference

Bayesian theorem is given in reference [Krapez 2019]:

$$\pi(\boldsymbol{\beta}|\mathbf{Y}) = \frac{\pi(\mathbf{Y}|\boldsymbol{\beta})\pi(\boldsymbol{\beta})}{\pi(\mathbf{Y})} \tag{5.50}$$

$\pi(\mathbf{Y}|\boldsymbol{\beta})$ is the likelihood function or the probability density of measurements with the parameters $\boldsymbol{\beta}$ given, $\pi(\boldsymbol{\beta})$ is the *a priori* density of the unknown or uncertain parameters, and $\pi(\mathbf{Y})$ is the marginal probability density of the measurements, which plays the role of a normalization constant. As for Eqs. (5.42) and (5.45), measurement uncertainties are supposed Gaussian with known zero-mean and a covariance matrix, additive, and independent from the unknown parameters. Thus, the likelihood function can be written:

$$\pi(\mathbf{Y}|\boldsymbol{\beta}) \propto exp\left\{-\frac{1}{2}\left[\mathbf{Y} - \boldsymbol{\varepsilon}\otimes\boldsymbol{\Phi}^{\mathbf{0},\boldsymbol{th}}(T)\right]^T \boldsymbol{\Omega}^{-1}\left[\mathbf{Y} - \boldsymbol{\varepsilon}\otimes\boldsymbol{\Phi}^{\mathbf{0},\boldsymbol{th}}(T)\right]\right\} \tag{5.51}$$

where $\boldsymbol{\Omega}$ is the measurement error covariance matrix and $\otimes$ denotes the element-wise product. Regarding the density of an *a priori* distribution of the parameters, $\boldsymbol{\Omega}$ is assumed independent and given by Eq. (5.52), where $\pi(\boldsymbol{\varepsilon})$ and $\pi(\mathrm{T})$ are the probability densities of the emissivity and the temperature, respectively:

$$\pi(\boldsymbol{\beta}) = \pi(\boldsymbol{\varepsilon})\pi(T) \tag{5.52}$$

5.3.4.1. Multispectral pyrometry in linear approximation

In the case of the linear approximation, Eq. (5.45) can be rewritten as:

$$\mathbf{Y} = \mathbf{X}\boldsymbol{\beta} + \mathbf{e}' \tag{5.53}$$

$$\mathbf{X} = [\mathbf{I_{mm}} \quad -\boldsymbol{\mu}_{\boldsymbol{m1}}] \tag{5.54}$$

$$\boldsymbol{\mu} = [\mu_1\ \mu_2 \ldots\ \mu_m]^T \tag{5.55}$$

where $\mathbf{I_{mm}}$ is the identity matrix of size $m \times m$. Thus, Eq. (5.51) becomes, considering Eq. (5.52) and the linear hypothesis:

$$\pi(\boldsymbol{\beta}|\mathbf{Y}) \propto exp\left\{-\frac{1}{2}[(\mathbf{Y}-\mathbf{X}\boldsymbol{\beta})^T\boldsymbol{\Omega}^{-1}(\mathbf{Y}-\mathbf{X}\boldsymbol{\beta})+(\boldsymbol{\beta}-\boldsymbol{\beta}^{\boldsymbol{prior}})^T\mathbf{W}^{-1}(\boldsymbol{\beta}-\boldsymbol{\beta}^{\boldsymbol{prior}})]\right\} \quad (5.56)$$

where $\mathbf{W}$ is the error matrix of the parameters. The maximum *a posteriori* (MAP) estimator is then obtained when the derivative of (5.56) is null with respect to the parameter vector. Introducing the MAP estimator and the posterior covariance matrix, Eq. (5.56) becomes:

$$\pi(\boldsymbol{\beta}|\mathbf{Y}) \propto \left\{-\frac{1}{2}\left[\left(\boldsymbol{\beta}-\widehat{\boldsymbol{\beta}}_{MAP}\right)^T\boldsymbol{\Gamma}_{\boldsymbol{\beta}|\mathbf{Y}}{}^{-1}\left(\boldsymbol{\beta}-\widehat{\boldsymbol{\beta}}_{MAP}\right)\right]\right\} \quad (5.57)$$

In relation (5.57), $\hat{\beta}_{MAP}$ is the MAP estimator (5.58) and $\boldsymbol{\Gamma}_{\boldsymbol{\beta}|\mathbf{Y}}$ is the posterior covariance matrix (5.59). They are given by [Krapez 2019]:

$$\widehat{\boldsymbol{\beta}}_{MAP} = \boldsymbol{\beta}^{\mathbf{prior}} + \mathbf{W}\mathbf{X}^{\mathbf{T}}(\mathbf{X}\mathbf{W}\mathbf{X}^{\mathbf{T}}+\boldsymbol{\Omega})^{-1}(\mathbf{Y}-\mathbf{X}\boldsymbol{\beta}^{\mathbf{prior}}) \quad (5.58)$$

$$\boldsymbol{\Gamma}_{\boldsymbol{\beta}|\mathbf{Y}} = \mathbf{W}-\mathbf{W}\mathbf{X}^{\mathbf{T}}(\mathbf{X}\mathbf{W}\mathbf{X}^{\mathbf{T}}+\boldsymbol{\Omega})^{-1}\mathbf{X}\mathbf{W} \quad (5.59)$$

5.3.4.2. Multispectral pyrometry in non-linear estimation

In the non-linear case, the theoretical fluxes are calculated from Eqs. (5.2) and (5.4), that is with Planck's law. The $\boldsymbol{\beta}$ vector of the parameter is the same as in Table 5.3.

A sampling method based on the Markov Chain Monte Carlo (MCMC) method is used in this work. The Metropolis-Hastings algorithm was applied to generate samples of the posterior distribution based on the likelihood given by Eq. (5.51). This algorithm begins with the selection of a proposal distribution $p(\boldsymbol{\beta}^*, \boldsymbol{\beta}^{j-1})$, which is used to define a new candidate $\boldsymbol{\beta}^*$, given the current state $\boldsymbol{\beta}^{j-1}$ of the Markov Chain. Once the proposal distribution is defined, the Metropolis-Hastings sampling algorithm can be implemented by repeating the following steps:

1- Sample a candidate $\boldsymbol{\beta}^*$ from the proposal distribution $p(\boldsymbol{\beta}^*, \boldsymbol{\beta}^{j-1})$.

2- Calculate the acceptance:

$$\alpha = min\left[1, \frac{\pi(\boldsymbol{\beta}^*|\mathbf{Y}), p(\boldsymbol{\beta}^*, \boldsymbol{\beta}^{\mathbf{j-1}})}{\pi(\boldsymbol{\beta}^{j-1}|\mathbf{Y}), p(\boldsymbol{\beta}^{j-1}, \boldsymbol{\beta})}\right] \quad (5.60)$$

3- Generate a random value U uniformly distributed between 0 and 1.

4- If $U \leq \alpha$, set $\boldsymbol{\beta}^j = \boldsymbol{\beta}^*$; otherwise, set $\boldsymbol{\beta}^j = \boldsymbol{\beta}^{j-1}$.

5- Return to step 1 to generate the sequence $\{\boldsymbol{\beta}^1, \boldsymbol{\beta}^2 \ldots, \boldsymbol{\beta}^n\}$.

In this manner, a sequence is generated to represent the *posterior* distribution, and inference on this posterior distribution is obtained from inference on the samples $\{\beta^1, \beta^2 \dots, \beta^n\}$. Note that the values β^i must be rejected as long as the chain has not converged.

5.3.4.3. Multispectral pyrometry using particle filters algorithm

A state estimation problem is solved, that is more consistent with the sequential estimation of the dynamic (time-dependent) vector $\boldsymbol{\beta}_k$, $k = 1,\dots M$, being the index of the time step. State estimation problems may be written in the form of evolution and observation models, which are modelled as stochastic processes [Arulampalam 2001][Ristic 2004][Kaipio 2006][Ozisik 2021]. The state variables are given by the vector $\boldsymbol{\beta}_k$ (see Table 5.3). The observed quantities, that is, the available measurements at each time t_k, are the fluxes from each photodetector arranged in the following vector: $\boldsymbol{\Phi}_k^{exp} = \left[\Phi_{k,1}^{exp}, \dots, \Phi_{k,N}^{exp}\right]^T$. We further assume that the state evolution model and the observation model are given by the general functions $\mathbf{f}_k$ and $\mathbf{g}_k$, respectively, that is:

$$\boldsymbol{\beta}_k = \mathbf{f}_k(\boldsymbol{\beta}_{k-1}, \mathbf{v}_{k-1}) \qquad \text{for} \quad k = 1, \dots, M \tag{5.61}$$

$$\boldsymbol{\Phi}_k = \mathbf{g}_k(\boldsymbol{\beta}_k, \mathbf{n}_k) \qquad \text{for} \quad k = 1, \dots, M \tag{5.62}$$

where $\boldsymbol{\Phi}_k$ is the model prediction of the measurements $\boldsymbol{\Phi}_k^{exp}$, while $\mathbf{v}$ and $\mathbf{n}$ represent the noises in the state evolution model and in the observation model, respectively.

Although different kinds of problems can be considered with the evolution-observation models described above [Arulampalam 2001][Ristic 2004][Kaipio 2006][Ozisik 2021], here we deal with the filtering problem where the state variables $\boldsymbol{\beta}_k$ are sequentially estimated with the measurements $\boldsymbol{\Phi}_k^{exp}$ at each time t_k. The state estimation problem is solved within the Bayesian framework of statistics. Thus, we apply Bayes´ theorem [Arulampalam 2001][Ristic 2004][Kaipio 2006][Ozisik 2021] (see Section 5.3.4).

Even though conceptually simple, the sequential estimation of the posterior probability density, $\pi\left(\boldsymbol{\beta}_k | \boldsymbol{\Phi}_k^{exp}\right)$, only allows an analytical treatment if the evolution and observation models are linear and with Gaussian additive uncertainties. In this case, the optimal solution of the state estimation problem is obtained with the classical Kalman filter [Arulampalam 2001][Ristic 2004][Kaipio 2006][Ozisik 2021]. On the other hand, for the case of nonlinear and/or non-Gaussian models, such as in the present work,

Sequential Monte Carlo Methods, also known as Particle Filters, are robust stochastic tools that can be generally applied to obtain samples of the posterior distribution at each time t_k. The goal of the particle filter is to draw a set of independent and identically distributed samples (particles) $\{\boldsymbol{\beta}_k^j\}_{j=1}^Q$ that approximates $\pi(\boldsymbol{\beta}_k|\boldsymbol{\Phi}_k^{exp})$, by starting from a set $\{\boldsymbol{\beta}_0^j\}_{j=1}^Q$ at time $t_0 = 0$. Since it is not possible to sample directly from the posterior probability density, particle filters make use of importance sampling followed by an update step in order to approximate the posterior probability density [Arulampalam 2001][Ristic 2004][Kaipio 2006][Ozisik 2021]. The posterior probability density of the state variables $\boldsymbol{\beta}_k$ at time t_k is then approximated through a weighted Monte Carlo realization from the importance density in terms of Q particles, i.e.:

$$\pi(\boldsymbol{\beta}_k|\boldsymbol{\Phi}_k^{exp}) \approx \sum_{j=1}^{Q} w_k^j \, \delta(\boldsymbol{\beta}_k - \boldsymbol{\beta}_k^j) \tag{5.63}$$

where w_k^j is the weight of the j^{th} particle at the time t^k with $\sum_{j=1}^{Q} w_k^j = 1$ and δ is the Dirac Delta function.

The most popular particle filter algorithms are the Sequential Importance Resampling (SIR) and the Auxiliary Sequential Importance Resampling (ASIR) [Arulampalam 2001][Ristic 2004][Kaipio 2006][Ozisik 2021]. Both are described next.

The Sampling Importance Resampling particle filter algorithm (SIR)

In the SIR algorithm, the importance density $\pi(\boldsymbol{\beta}_k^j|\boldsymbol{\beta}_{k-1}^j)$ is chosen as the prior density that is obtained from the evolution model. Since the importance density is independent of the information conveyed by the measurements $\boldsymbol{\Phi}_k^{exp}$, the state space is explored without any information about the measurements at the current time. Hence, this algorithm can be inefficient and sensible to outliers [Arulampalam 2001][Ristic 2004][Kaipio 2006][Ozisik 2021]. The SIR algorithm can be summarized by the steps presented in Table 5.4, as applied to the system evolution from t_{k-1} to t_k [Arulampalam 2001][Ristic 2004][Kaipio 2006][Ozisik 2021].

Table 5.4. Sampling Importance Resampling (SIR) algorithm [Arulampalam 2001][Ristic 2004][Kaipio 2006][Ozisik 2021].

Step 1
For $j = 1,...,Q$ draw new particles $\boldsymbol{\beta}_k^j$ from the prior density $\pi(\boldsymbol{\beta}_k^j \mid \boldsymbol{\beta}_{k-1}^j)$ and then use the likelihood density to calculate the corresponding weights $w_k^j = \pi\left(\boldsymbol{\Phi}_k^{exp} \mid \boldsymbol{\beta}_k^j\right)$.
Step 2
Normalize the weights, that is, for $j = 1,...,Q$ let $w_k^j = w_k^j / \sum_{j=1}^{Q} w_k^j$.
Step 3
Resample the particles as follows: Construct the cumulative sum of weights (CSW) by computing $c_j = c_{j-1} + w_k^j$ for $j = 1,...,Q$ with $c_0 = 0$. Let $j = 1$ and draw a starting point u_1 from the uniform distribution $\mathcal{U}(0, Q^{-1})$ For $j^* = 1,...,Q$ Move along the CSW by making $u_{j^*} = u_1 + Q^{-1}(j^* - 1)$ While $u_{j^*} > c_j$ make $j = j + 1$ Assign sample $\boldsymbol{\beta}_k^{j*} = \boldsymbol{\beta}_k^j$ Assign uniform weights to the samples, that is, $w_k^{j*} = Q^{-1}$

The Auxiliary Sampling Importance Resampling particle filter algorithm (ASIR)

The Auxiliary Sampling Importance Resampling (ASIR) algorithm is an extension of the SIR algorithm, in which an attempt is made to overcome the loss of diversity by performing the resampling step at time t_{k-1} with the available measurement at time t_k [Arulampalam 2001][Ristic 2004][Ozisik 2021]. It is then expected that the optimal importance density $\pi(\boldsymbol{\beta}_k^j \mid \boldsymbol{\beta}_{k-1}^j, \boldsymbol{\Phi}_k^{exp})$ can be better represented [Arulampalam 2001][Ristic 2004]. The resampling is based on some point estimate $\boldsymbol{\mu}_k^j$ that characterizes $\pi(\boldsymbol{\beta}_k^j \mid \boldsymbol{\beta}_{k-1}^j)$, which can be the mean or simply a sample of this density. If the state evolution model noise is small, then $\pi(\boldsymbol{\beta}_k^j \mid \boldsymbol{\beta}_{k-1}^j)$ is well characterized by $\boldsymbol{\mu}_k^j$, so that the weights w_k^j are more even and the ASIR algorithm is less sensitive to outliers than the SIR algorithm. On the other hand, if the state evolution model noise is large, then the single point estimate $\boldsymbol{\mu}_k^j$ in the state space may not characterize well $\pi(\boldsymbol{\beta}_k^j \mid \boldsymbol{\beta}_{k-1}^j)$ and the ASIR algorithm may not be as effective as the SIR algorithm. The ASIR algorithm can be

summarized by the steps presented in Table 5.5, as applied to the system evolution from t_{k-1} to t_k [Arulampalam 2001][Ristic 2004][Ozisik 2021].

Table 5.5. Auxiliary Sampling Importance Resampling (ASIR) algorithm [Arulampalam 2001][Ristic 2004][Ozisik 2021].

Step 1
For $j = 1,...,Q$ draw new particles $\boldsymbol{\beta}_k^j$ from the prior density $\pi(\boldsymbol{\beta}_k^j|\boldsymbol{\beta}_{k-1}^j)$ and then calculate some characterization $\boldsymbol{\mu}_k^j$ of $\boldsymbol{\beta}_k^j$, given $\boldsymbol{\beta}_{k-1}^j$. Then use the likelihood density to calculate the corresponding weights $w_k^j = \pi(\boldsymbol{\Phi}_k^{exp}|\boldsymbol{\beta}_k^j)w_{k-1}^k$.
Step 2
Normalize the weights, that is, for $j = 1,...,Q$ let $w_k^j = w_k^j / \sum_{j=1}^{Q} w_k^j$.
Step 3
Resample the particles as follows: Construct the cumulative sum of weights (CSW) by computing $c_j = c_{j-1} + w_j^k$ for $j = 1,...,Q$ with $c_0 = 0$. Let $j = 1$ and draw a starting point u_1 from the uniform distribution $\mathcal{U}(0, N^{-1})$ For $j^* = 1,...,Q$ Move along the CSW by making $u_{j^*} = u_1 + Q^{-1}(j^* - 1)$ While $u_{j^*} > c_j$ make $j = j + 1$ Assign sample $\boldsymbol{\beta}_k^{j*} = \boldsymbol{\beta}_k^j$ Assign parent $i^j = j$
Step 4
For $j = 1,...,Q$ draw new particles $\boldsymbol{\beta}_k^j$ from the prior density $\pi(\boldsymbol{\beta}_k^j|\boldsymbol{\beta}_{k-1}^j)$, using the parent i^j, and use the likelihood density to calculate the corresponding weights $w_k^j = \pi(\boldsymbol{\Phi}_k^{exp}|\boldsymbol{\beta}_k^j)/\pi(\boldsymbol{\Phi}_k^j|\boldsymbol{\beta}_k^j)$
Step 5
Normalize the weights, that is, for $j = 1,...,Q$ let $w_k^j = w_k^j / \sum_{j=1}^{Q} w_k^j$.

Implementation of the particle filters algorithm

For the implementation of the particle filter algorithms described above, the observation model is given by:

$$\Phi_{k,i}^{th} \equiv F_i \varepsilon(\lambda_i, T_k) I^0(\lambda_i, T_k) + e_k^i \tag{5.64}$$

where e_k^i is the additive measurement uncertainty, which is modeled as an independent Gaussian variable, with zero mean and constant standard deviation. Based on the calibration process, the standard deviation of the measurement errors was fixed as $\sigma =$ 100 nW. Thus, the likelihood function is given by:

$$\pi\left(\mathbf{\Phi}_k^{exp} \middle| \boldsymbol{\beta}_k\right) \propto exp\left\{-\frac{1}{2}\sum_{i=1}^{N} \frac{\left[\Phi_{k,i}^{exp} - \Phi_{k,i}^{th}\right]^2}{\sigma^2}\right\} \tag{5.65}$$

The evolution model for the temperature is based on the calibration process of the measurement system with the blackbody (see [Pierre 2022] for details). We denote $\theta_i(\Phi_b^0)$ as the function that fits the temperature with respect to the blackbody spectral flux Φ_b^0, which was measured with detector i in the calibration process (see Section 5.1.3, Figure 5.15). A first order Taylor´s series approximation for the time variation of the temperature gives:

$$\hat{T}_i(t_k) \approx \hat{T}_i(t_{k-1}) + \frac{\partial \theta_i(t_{k-1})}{\partial \Phi_b^0}\left(\Phi_{k,i}^{exp} - \Phi_{k-1,i}^{exp}\right) \tag{5.66}$$

where $\hat{T}_i(t_k)$ is the temperature at time t_k estimated with the calibration curve of detector i, that is, $\theta_i(\Phi_b^0)$. Note in Eq. (5.66) that the time variations of the fluxes measured during the experiment were assumed equal to the time variations of the fluxes measured in the calibration process with the blackbody. The evolution model for temperature was then obtained as:

$$T(t_k) = \tilde{T}(t_k) + e_{k,T} \tag{5.67}$$

where $e_{k,T}$ is a Gaussian random variable with zero mean and standard deviation of $0.05\tilde{T}(t_k)$ and:

$$\tilde{T}(t_k) = \frac{1}{N}\sum_{i=1}^{N} \hat{T}_i(t_k) \tag{5.68}$$

Such an evolution model for the temperature is independent of the emissivities, which were time-dependent with a random walk model for the parameters a_0 and a_1 (see Table 5.3), that is:

$$a_{0,k} = a_{0,k-1} + e_{a_0,k} \tag{5.69}$$

$$a_{1,k} = a_{1,k-1} + e_{a_1,k} \tag{5.70}$$

where the random variables $e_{a_0,k}$ and $e_{a_1,k}$ are also Gaussian, with zero means and standard deviations of $0.01a_{0,k-1}$ and $0.01a_{1,k-1}$, respectively.

Since the initial distributions of the state variables were unknown, samples were initially generated at time $t = 0$ from the following uniform distributions: 1 000 K $\leq T \leq$ 2 500 K, $-2\ \mu m^{-1} \leq a_1 \leq +2\ \mu m^{-1}$ and $0 \leq a_0 \leq 1$. The sample that resulted in the maximum likelihood at $t = 0$ was selected and then the particles were generated from a Gaussian distribution centered at this sample with a relative standard deviation of 10^{-2}.

5.3.5. Results and discussion

All the results, due to the multiple techniques presented in Table 5.3, are not presented in this section. As already mentioned in introduction of Section 5.3.4, tests have been performed on niobium and mild steel, but only results with niobium are presented.

First, Figures 5.38 to 5.41 are dedicated to bi- and multispectral estimation using OLS. We first analyze the solution of Eqs. (5.37)-(5.40) using two radiative fluxes Φ_3^{exp} and Φ_4^{exp} by considering $\varepsilon_3 = \varepsilon_4$, for different initial guesses of temperature and emissivity, by comparison with literature values of emissivity at the melting temperature. As the results are not satisfying, greybody assumption should be relieved, which means that one should solve Eqs. (5.47)-(5.48) by introducing an emissivity ratio ξ_{43}. Estimation of this parameter is only possible using a known data, such as the solidification plateau. This estimation is based on the experimental data, obtained during the cooling period, when the bispectral commercial pyrometer measures temperature T_{bis}. This minimization is based on a high level of confidence in the temperature given by the commercial bispectral pyrometer T_{bis} (black dashed line in Figure 5.36). Indeed, the measured temperature during the solidification plateau has been estimated at (2 731 $\pm$ 12) K (*i.e.* 0.5 %), which is consistent with literature [Incropera 2002], and its emissivity ratio has been set to 1.025. Then the principle is to minimize the mean of the residuals (5.71) between estimated temperature T_{ij} and T_{bis} during a short time interval (between 5.9 s and 6.9 s).

$$\frac{1}{N}\sum_{k=1}^{N}\left[T_{ij}(t_k) - T_{bis}(t_k)\right]^2 \tag{5.71}$$

Consequently, $\xi_{43} = 1.087$ and the results of emissivity and temperature obtained for this value are presented in Figure 5.38. Even if the emissivity ratio has been evaluated during the short time interval of solidification, the obtained value has been applied to the whole duration of the experiment. Even if literature mentions a rather constant emissivity in the liquid state [Seifter 2001], this is a major assumption.

Figure 5.39 shows temperature results after multiple multispectral combinations. No constrains have been imposed. It appears clearly that results are very different from one combination to the other, and the most credible one is for the combination using the radiative fluxes Φ_1^{exp}, Φ_2^{exp}, Φ_4^{exp}, and Φ_5^{exp}, due to the knowledge of the solidification plateau temperature.

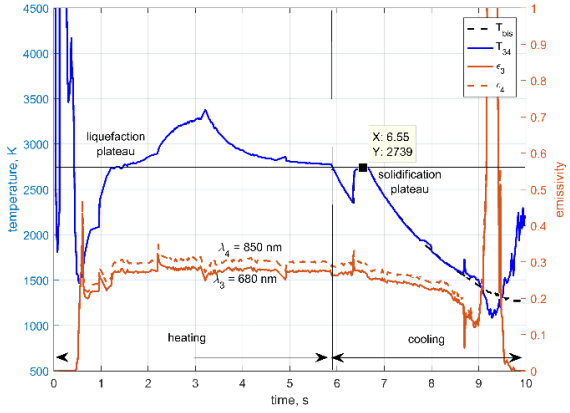

Figure 5.38. Bispectral temperature emissivity estimation with Φ_3^{exp} and Φ_4^{exp}.

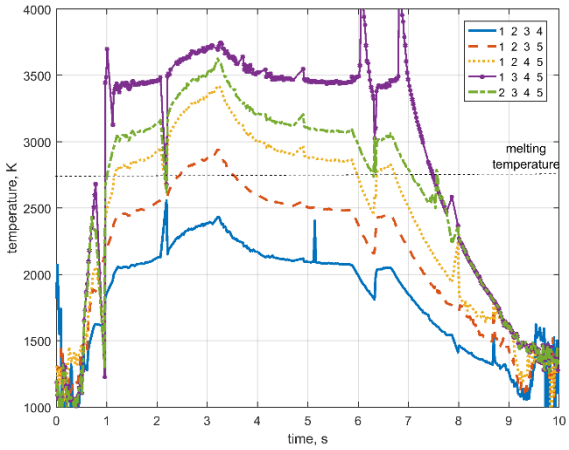

Figure 5.39. Estimated temperature with the combinations of four signals with OLS.

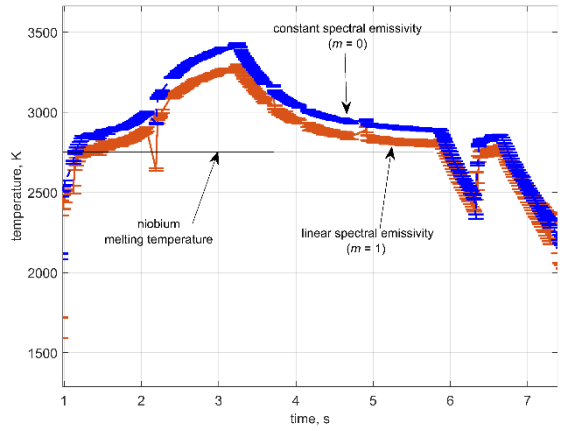

Figure 5.40. Estimated temperatures by multispectral method using Eqs. (5-37)-(5.42).

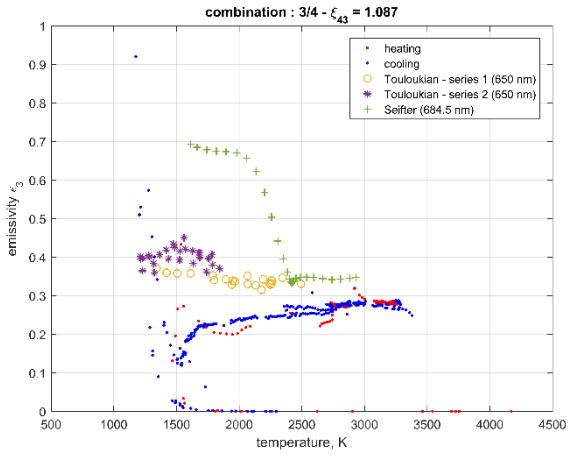

Figure 5.41. Estimated emissivity ε_3 (λ_3 = 0.680 µm) versus temperature and comparison with literature data at approximatively the same wavelength [Touloukian 1970][Cezairliyan 1970][Seifer 2001].

However, the use of constrains developed in Section 5.2.2 with Eqs. (5.37)-(5.42) allows to estimate correctly the temperature using a proper choice of wavelengths such as in Figure 5.40: $\lambda_2 = 0.530$ µm, $\lambda_3 = 0.680$ µm, $\lambda_5 = 0.940$ µm, and $\lambda_6 = 1.055$ µm. Constant, linear, and parabolic emissivity models have also been tested and it appears that, in the spectral range of the pyrometer, the linear model gets relevant temperature due to the knowledge of solidification plateau temperature.

Finally, estimated emissivity at the wavelength $\lambda_3 = 0.680$ µm is presented in Figure 5.41 versus temperature and compared with data from literature. In solid state, emissivity tends to decrease from 0.6 around 1 200 K to 0.3 until the melting plateau, and are closer to Touloukian's value than Seifter's value [Seifer 2001][Touloukian 1970][Cezairliyan 1970]. However, in solid state, these emissivity and temperature are estimated values from fluxes recorded after 9 s (Figure 5.36), so they must be considered very carefully, since fluxes are lower than 50 nW, which is at the lower limit of confidence of the sensor. Then in liquid state, emissivity is constant and just below 0.3 whereas other values are rather between 0.3 and 0.4. There is obviously a strong dispersion between measurements and literature values, and they are in the range 0.20 – 0.40.

Now parameter estimation is performed according to Bayesian method linear approximation with fluxes Φ_3^{exp} and Φ_4^{exp}. Theoretical fluxes are linearized, as presented in Eqs. (5.45)-(5.46). Estimations are performed during the first part of the cooling, mainly during the solidification plateau. Three parameters are considered: temperature and two emissivities. Tests are performed with different levels of confidence, with priors of good or bad quality.

In the first stage, we concentrated on the solidification plateau. Since the phase-change temperature is well-known, we introduced a temperature prior of small uncertainty, $T^{prior} = (2\,750 \pm 30)$ K whereas emissivity priors were given with a high uncertainty, namely $\varepsilon_3^{prior} = \varepsilon_4^{prior} = 0.30 \pm 0.15$. Figures 5.42 and 5.43 show normalized probability densities for the three parameters. On the solidification plateau, mean and standard-deviation of emissivities are $\varepsilon_3 = 0.261 \pm 0.023$ and $\varepsilon_4 = 0.288 \pm 0.020$ and for temperature $T = (2\,748 \pm 29)$ K.

Method has then been extended to the whole duration of the experiment by levering the previous results. As a matter of fact, since we have now a better confidence into the emissivity values, we considered as new priors $\varepsilon_3^{prior} = 0.260 \pm 0.023$ and

$\varepsilon_4^{prior} = 0.290 \pm 0.020$, whereas temperature was given a prior of reduced quality since it is expected to evolve widely during the experiment: $T^{prior} = (2\,000 \pm 1\,000)$ K.

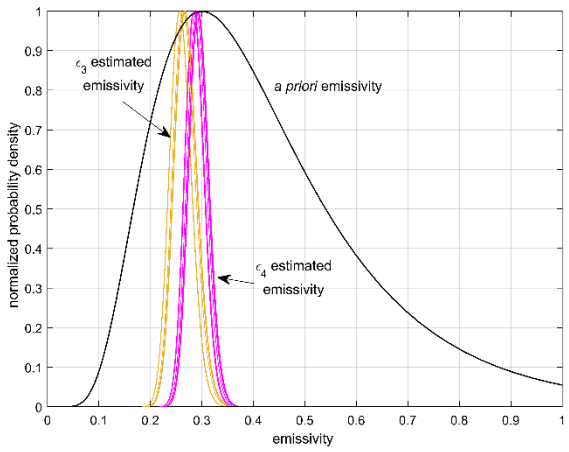

Figure 5.42. *A priori* and estimated emissivities ε_4 and ε_5 at solidification plateau.

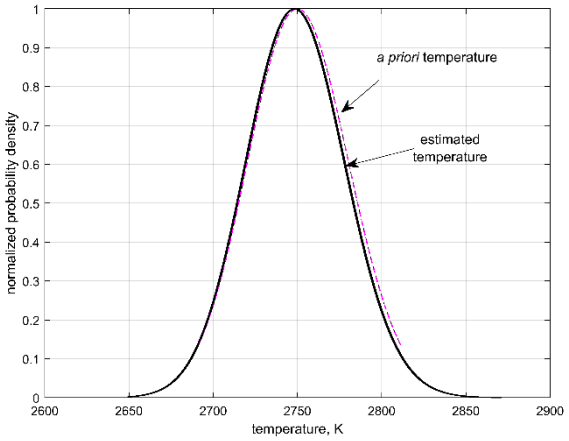

Figure 5.43. *A priori* and estimated temperature at solidification plateau.

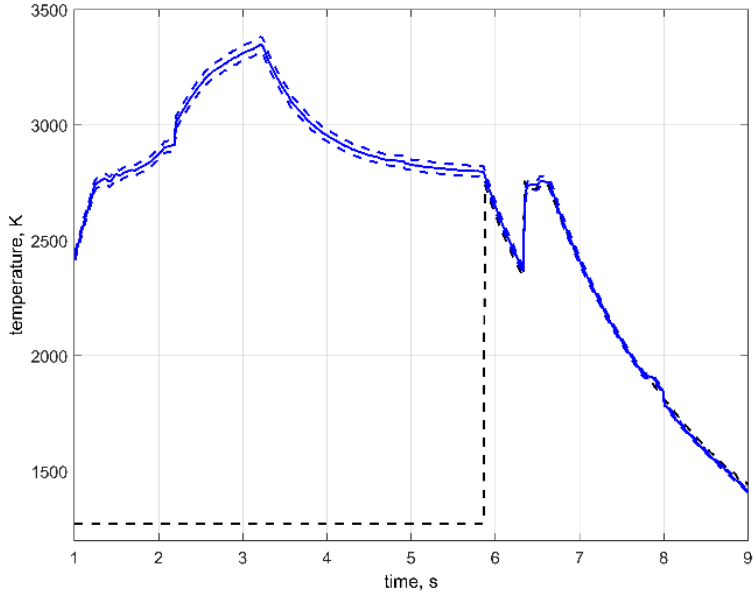

Figure 5.44. MAP estimator of temperature (in blue) with plus or minus one standard-deviation (dashed blue) and bispectral pyrometer (dashed black).

Results of this second identification step are described in Figures 5.44 for the temperature. It is not presented here but the MAP estimator of the emissivity ε_3 and ε_4 are quite stable in liquid phase. On the contrary, in the solid phase, ε_3 shows a slight increase whereas ε_4 shows a slight decrease. The mean standard-deviation of the estimator of temperature is between 7 and 32 K during the period [1s, 9s] of the experiment.

Procedure has been repeated with the signals Φ_2^{exp}, Φ_3^{exp}, Φ_4^{exp}, Φ_5^{exp}, and Φ_6^{exp}, and the linear parameter model assuming five independent emissivities with the same procedure of estimation in two steps. For the first step, Figure 5.45 shows priors and MAP estimates for emissivities during the solidification plateau. Then, for the second step, Figure 5.46 shows emissivities estimated during the whole experiment only for two wavelengths for a sake of clarity. Temperature at solidification plateau is well estimated (such as in Figure 5.44), but it is interesting to observe that the evolution of emissivity versus wavelength is not linear, not even monotonic. Estimated spectral variation of emissivity invalidates the choice of a linear model, and offers a great challenge for a quadratic model, which possibly explains the errors obtained with emissivity-model-based methods.

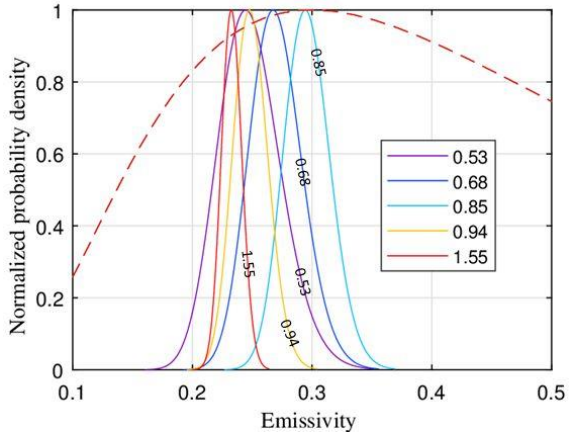

Figure 5.45. Linear parameter model (MAP estimation) First step - Normalized probability density function of emissivity at t = 6.53 s, in five wavelengths for niobium. Dashed line: prior probability; solid line: MAP estimation.

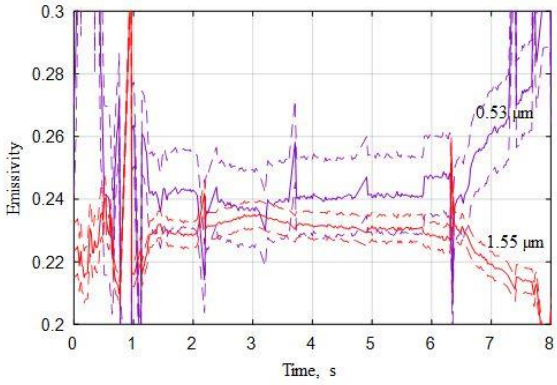

Figure 5.46. Linear parameter model (MAP estimation) Second step – Solid lines: Mean values of emissivities at 0.53 µm (purple) and 1.55 µm (red). Dashed lines: 99 % confidence interval.

Now parameter estimation is performed according to Bayesian method in non-linear case, using MCMC (Section 5.3.4.2), still with fluxes Φ_3^{exp} and Φ_4^{exp}. Estimation has been performed during the whole experiment and only two parameters are considered: temperature and emissivity ε_{34}. The parameters a and b of the emissivity model (see Table 5.3) were assigned with uniform priors in the intervals [-2 , 0], and [0 , 2], respectively. Temperature was also assigned with a uniform prior in the interval between

273 K and 4 000 K. Markov chains were started with parameters with the same priors as previously (of good quality for the temperature and bad quality for the emissivity). The chains were run with 30 000 states and the 15 000 first states were neglected for the computation of the posterior statistics (burn-in period). Figures 5.47 and 5.48 show the good fitting between the experimental and estimated flux and temperature, respectively. The 2.5 % and 97.5 % quantiles have also been calculated and presented in these figures, for the verification of the estimated fluxes and temperature versus the experimental ones.

Finally, Figures 5.49 and 5.50 present the states of the Markov chains for both the temperature and emissivity at $t = 6.7$ s, that is, during the solidification plateau. They clearly show that the estimation tends to a rather constant value after 10 000 states. The histograms plotted for values after 15 000 states are not of Gaussian shapes, especially as regards the temperature. The prior for the temperature was centred at values at previous time with a constant standard deviation of 300 K, while the prior for the emissivity was considered as uniform in the interval [0, 1]. The estimated values for the solidification plateau are $T = (2\,747 \pm 2)$ K, $\varepsilon_{34} = 0.303 \pm 0.002$.

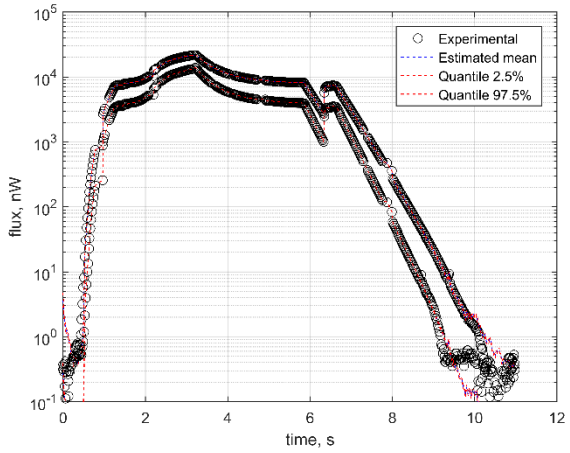

Figure 5.47. Estimated and experimental fluxes.

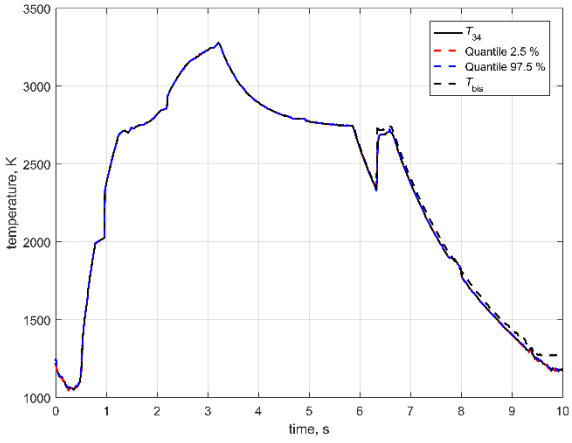

Figure 5.48. Estimated and experimental temperatures.

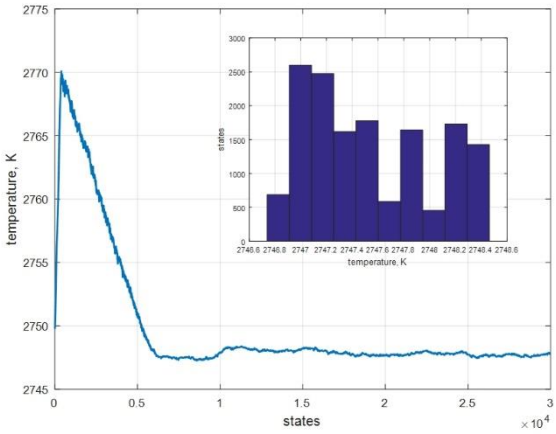

Figure 5.49. Markov chain states for the temperature estimation.

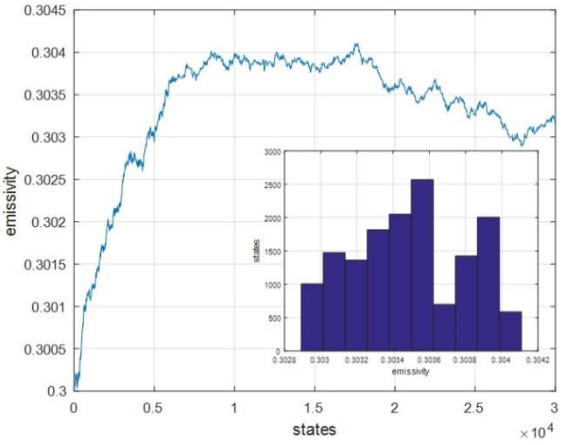

Figure 5.50. Markov chain states for the emissivity estimation.

The last estimation technique is the Bayesian inference with particle filters. Figures 5.51 and 5.52 present the temperatures estimated with the SIR algorithm by using the measurements of sensors 2 to 6 and 3 to 6. The temperatures measured with the bichromatic pyrometer are also presented in these figures. Similar results are presented in Figures 5.53 and 5.54 for the ASIR algorithm. Results obtained with the measurements of other combinations of detectors used in the inverse analysis were similar to those shown by Figures 5.51 to 5.54, except with the measurements from detectors 3, 4 and 6 when the temperature residuals were larger than 300 K. The estimated temperatures shown by Figures 5.51 to 5.54 were quite consistent, despite the fact that they involved different combinations of measurements and algorithms used for the solution of the state estimation problem.

Furthermore, the estimated temperatures show an excellent agreement with those measured by the bichromatic pyrometer that were used as a reference. In fact, the amplifications of Figures 5.51 and 5.52 (temperatures estimated with the measurements of detectors 2 to 6 by using the SIR and ASIR algorithms, respectively) in the region where the bichromatic pyrometer measurements were available reveal that the estimated 95 % credible intervals of temperature included the measurements. Also, the means of the estimates were within the pyrometer measurement uncertainties.

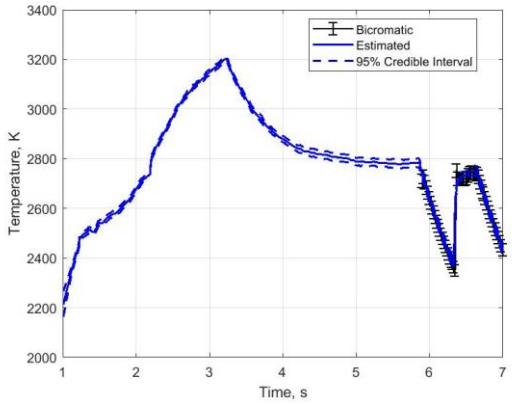

Figure 5.51. Temperatures estimated with the SIR algorithm for niobium by using the measurements of detectors: (a) 2, 3, 4, 5 and 6; (b) 3, 4, 5 and 6.

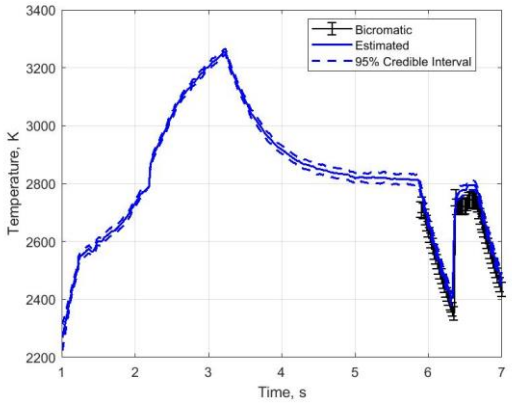

Figure 5.52. Temperatures estimated with the SIR algorithm for niobium by using the measurements of detectors: (a) 2, 3, 4, 5 and 6; (b) 3, 4, 5 and 6.

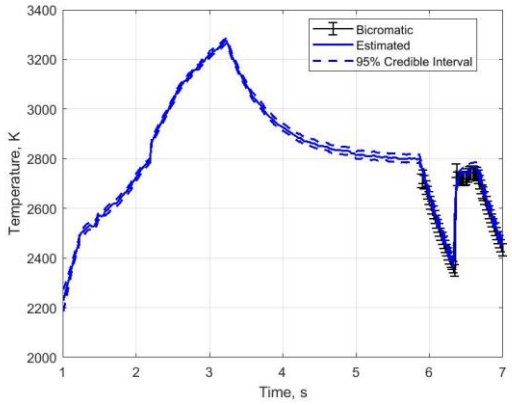

Figure 5.53. Temperatures estimated with the ASIR algorithm for niobium by using the measurements of detectors: (a) 2, 3, 4, 5 and 6; (b) 3, 4, 5 and 6.

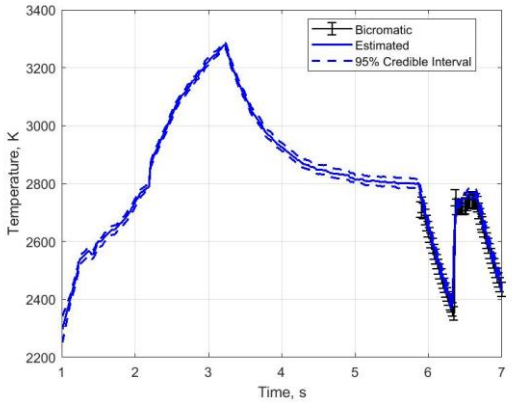

Figure 5.54. Temperatures estimated with the ASIR algorithm for niobium by using the measurements of detectors: (a) 2, 3, 4, 5 and 6; (b) 3, 4, 5 and 6.

The variation with temperature of the emittance at the wavelength of sensor 3, obtained with SIR algorithm and the measurements of detectors 2 to 6, is presented in Figure 5.55. This figure shows that there is a hysteresis of the estimated emissivity values as the sample was heated and then cooled. However, the emissivities shown in Figure 5.55, including the observed hysteresis, are quite consistent with values encountered in the literature [Seifer 2001][Touloukian 1970][Cezairliyan 1970].

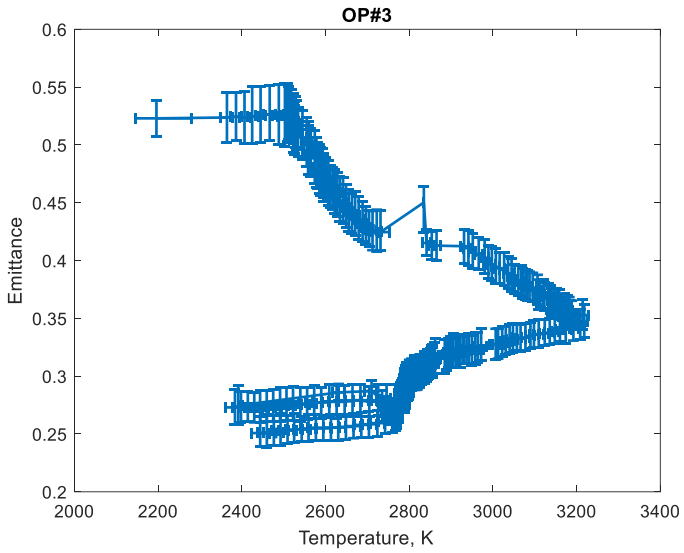

Figure 5.55. Variation of the emissivity (or emittance) of niobium at the wavelength of detector 3 estimated with the measurements of detectors 3 to 6 and the SIR algorithm.

5.3.6. Partial conclusion

This Section 5.3. was dedicated to the presentation of different techniques of estimation of both temperature and emissivity: deterministic techniques based on ordinary least squares and statistical techniques such as Bayesian inference with MAP, MCMC, or particle filters. Estimation results have been obtained from the same experimental data: the radiative fluxes measured by the six-wavelength pyrometer (see Section 5.1) during the melting of a niobium sample.

Most of the time, all techniques present successful and encouraging results. Indeed, working with pure metal such as niobium is very convenient since crucial information for the verification of estimations is available: here the solidification temperature. It has been helpful most of the time, except with OLS methodology with constrains (Section 5.3.3), which gave good estimation results as long as the emissivity model is correct. Globally, all techniques of estimation are dependent of priors on parameters.

Other experiments with mild steel have already been performed, but not presented here. Estimations are more difficult to verify since there is no information about this alloy (see [Pierre 2022][Pierre 2023][Lamien 2023]).

5.4. Conclusion

This Section 5 concerns simultaneous estimation of temperature and emissivity of metals mainly around and above the liquid state. Section 5.1 dealt with basics on multispectral pyrometry, calibration, blackbody. Section 5.2 discussed about the selection of the wavelengths and their number. And Section 5.3 was about the tools available to perform temperature emissivity estimation.

Simultaneous estimation of temperature and emissivity can be performed through different experimental apparatuses: mono-, bispectral pyrometers, (home-made) multispectral pyrometer, or spectroradiometer (*e.g.* for hyperspectral pyrometry). It seems more interesting to have the maximum of information, that is using the maximum of wavelengths and thus reconstruct a part of Planck's law in the spectral range of the detector. However, the increase of wavelengths increases also the calculation time for estimation.

If it is possible, for applications where temperature varies slightly (but what does slightly mean?) the selection of a limited number of wavelengths would be sufficient, as it is the case with the six-wavelength pyrometer, or even with commercial pyrometers listed in Section 5.1.3. In the extreme case, for a given temperature, the selected wavelengths must belong to the useful spectral range, meaning between $0.5\lambda_m$ and $5\lambda_m$, where λ_m is the wavelength of maximum emission for the temperature T. The signal to noise ratio would be acceptable and the radiative measurements for each wavelength exploitable.

For applications where the temperature variation exceeds several thousands of kelvins, measurements with a spectroradiometer would be more relevant. These apparatuses are appropriate since they can cover spectral range of about several micrometres and some can make possible hyperspectral measurements: less than ten nanometres between two consecutive wavelengths. In this case, each sequence of measurement at a time t_k represents a non-negligible part of Planck's law, where the observable is the radiative flux and the variable the wavelength.

In every case, calibration remains mandatory using reference temperature (*e.g.*, blackbody, melting point).

The major issue is emissivity: what is well-known is that emissivity is not. Behaviour of emissivity of a surface during experiment is more or less unpredictable, since it depends on many factors: wavelength, temperature, direction, surface roughness,

impurities. So, literature presents researches who try to consider emissivity, or to skip it, temperature being the parameter of interest most of the time. And a bad choice for an emissivity model can lead to important uncertainty regarding the temperature estimation.

All the methodology of estimation tested and presented in Section 5.3 are confronted to the problem of emissivity model and on the need of good priors and prediction of temperature and emissivity. I suppose neural networks will be also confronted to the same problem.

The major perspective to all the studies presented in Section 5 is to investigate the behaviour of this parameter. First, the knowledge of this behaviour would lay on a cautious study of the microscopic aspect of the surface (roughness, impurities). Moreover, for anyone who works with radiative transfers, it is a necessity to read reference books dealing with them: [Siegel 1992][Modest 2003], mainly (unfortunately, I only recently start to read these books). [Siegel 1992][Modest 2003] of recent editions have several chapters dedicated to radiative properties from both theoretical and experimental points of view. For example, basics on electromagnetic theory state relations to predict radiative properties considering ideal, meaning optically smooth surface. But departures between predictive properties and measured ones exist and are caused by "surface roughness, surface contamination, impurities, and crystal-structure modification by surface working" [Siegel 1992]. However, trends are most of the time respected and satisfied numerous numbers of applications.

References

[Araújo 2017] Araújo A., Multi-spectral pyrometry – a review, Meas. Sci. Technol. 28 (2017) 082002 (15 pp).

[Arulampalam 2001] S. Arulampalam, *et al.*, A tutorial on particle filters for on-line non-linear/non-gaussian Bayesian tracking, *IEEE Trans. Signal Processing*, 50, 174-188, 2001.

[Audaire 2000] Audaire L., Détecteurs de rayonnement optique, Techniques de l'Ingénieur, R6450, 2000.

[Bauer 1971] Bauer, G., et K. Bischoff. « Evaluation of the Emissivity of a Cavity Source by Reflection Measurements ». *Applied Optics*, vol. 10, nº 12, décembre 1971, p. 2639-43.

[Cadiou 2020] Cadiou, S., et al. « Heat Transfer, Fluid Flow and Electromagnetic Model of Droplets Generation and Melt Pool Behaviour for Wire Arc Additive Manufacturing ». *International Journal of Heat and Mass Transfer*, vol. 148, février 2020, p. 119102.

[Campbell 1925] Campbell N. R., Gardiner H. W. B., Photo-Electric color matching, Journal of Scientific Instruments, Vol. II, No. 6, March 1925.

[Cezairliyan 1970] A Cezairliyan et al., *High-speed (subsecond) measurement of heat capacity, electrical resistivity, and thermal radiative properties of molybdenium in the range 1900 to 2800 K*, J. Res. Nat. Bur. Stand. 74A: 65-92 (Jan-Feb 1970), janvier 1970.

[Dejaeghere 2016] Dejaeghere Laurent, Méthode de mesure par pyrométrie multispectrale et développement d'un dispositif à hautes températures, thèse, Université Bretagne Sud, 2016.

[Dejaeghere 2018] L. Dejaeghere, T. Pierre, M. Carin, P. Le Masson, M. Courtois, *Development and validation of a high temperature inductive furnace dedicated to molten metals characterization*, High Temperatures High Pressure, 2018.

[Geslain 2018] Geslain, Edouard, et al. « Coating Effects on Contact Conditions in Resistance Spot Weldability ». *Journal of Materials Processing Technology*, vol. 253, mars 2018, p. 160-67.

[Gömöry 1997] Gömöry, Fedor. « Characterization of High-Temperature Superconductors by AC Susceptibility Measurements ». *Superconductor Science and Technology*, vol. 10, nº 8, août 1997, p. 523.

[Hartmann 2009] Hartmann, Jürgen. « High-Temperature Measurement Techniques for the Application in Photometry, Radiometry and Thermometry ». *Physics Reports*, vol. 469, nº 5, janvier 2009, p. 205-69.

[Hervé 1988] Hervé P., Patent n°F.8803874 « Pyromètre Ultraviolet », 03-23-1988.

[Hervé 1991] Hervé P., Sicard J., Rakotoarisoa M., *Pyrométrie dans l'ultraviolet*, Actes du colloque de thermique SFT 1991, 139-142.

[Hervé 2001] Hervé P., Pinat V., *Thermographie par comptage de photons dans l'ultraviolet*, Deuxième colloque francophone – Méthodes et Techniques Optiques pour industrie – Vol. 1, S.F.O. 20-23 novembre 2001, Trégastel, France, 31-38.

[Houssein 2023] Houssein Jad, et al., *A novel apparatus dedicated to the thermal diffusivity estimation of metals at high temperature*, International Journal of Thermal Science, accepted for publication.

[Ikeuchi 1998] Ikeuchi, Ken, et al. « High-Temperature Measurements in Well WD-1A and the Thermal Structure of the Kakkonda Geothermal System, Japan ». *Geothermics*, vol. 27, nº 5, août 1998, p. 591-607.

[Incropera 2002] F. P. Incropera, D. P. DeWitt, *Fundamentals of heat and mass transfer*, Fifth Ed., Wiley, New-York, 2002.

[Kaipio 2006] J Kaipio, E Somersalo *Statistical and computational inverse problems*. Springer Science & Business Media 2006.

[Khalid 2008] Khalid, Ashiq Hussain, et Konstantinos Kontis. « Thermographic Phosphors for High Temperature Measurements: Principles, Current State of the Art and Recent Applications ». *Sensors*, vol. 8, nº 9, septembre 2008, p. 5673-744.

[Krapez 2011] J.-C. Krapez, Radiative measurements of temperature, in Thermal Measurements and Inverse Techniques, Taylor & Francis, 2011.

[Krapez 2019] J.-C. Krapez, *Measurements without contact in heat transfer. Part A: radiative thermometry: principles, implementation and pitfalls*, Lecture 4 from METTI 7 advanced School, Volume 1: Lectures, Porquerolles, France, Sept. 29th – Oct. 4th, 2019.

[Lamien 2023] Bernard Lamien *et al.*, *Temperature estimation using particle filter techniques – Application on liquid niobium and 100c6 steel*, High temperatures – high pressures, article soumis.

[Le Maux 2019] Le Maux, Dylan, et al. « Density measurement of liquid 22MnB5 by aerodynamic levitation ». *Review of Scientific Instruments*, vol. 90, nº 7, juillet 2019, p. 074904.

[Le Maux 2022] Le Maux, Dylan, et al. « Surface Tension of Liquid Fe, Nb and 304L SS and Effect of Drop Mass in Aerodynamic Levitation ». *Journal of Materials Science*, vol. 57, nº 25, juillet 2022, p. 12094-106.

[Le Maux 2023] Dylan Le Maux, et al., *La lévitation aérodynamique dédiée à l'estimation de la viscosité de métaux liquides*, Actes du congrès de thermique SFT, Reims, 30 mai – 2 juin 2023.

[Modest 2003] M.F. Modest, *Radiative heat transfer*, Academic Press, New-York, 2003.

[Muller 2012] Muller, Maryse, et al. « Temperature measurement of laser heated metals in highly oxidizing environment using 2D single-band and spectral pyrometry ». *Journal of Laser Applications*, vol. 24, nº 2, mai 2012, p. 022006.

[Nordine 1986] Nordine P.C., *The accuracy of multicolour optical pyrometry*, High Temperature Science 21 (1986) 97-109.

[Ohji 1995] Ohji, T., et al. « Temperature measurement by UV thermal radiation ». *Welding International*, vol. 9, nº 3, janvier 1995, p. 185-90.

[Ozisik 1973] N. Ozisik, *Radiative transfer*, Wiley and sons, New-York, 1973. [Siegel 1992] R. Siegel, J.R. Howell, *Thermal radiation heat transfer*, éditions Taylor and Francis, New York (1992).

[Ozisik 2021] M Ozisik and H. Orlande, *Inverse Heat Transfer: Fundamentals and Applications*, CRC Press, Boca Raton, 2021.

[Pierre 2007] Pierre Thomas, Mesure de la température à l'échelle microscopique par voie optique dans la gamme ultraviolet-visible, thèse, Université de Lorraine, 2007.

[Pierre 2008] Pierre T., Rémy B., Degiovanni A., *Micro-scale temperature by multi-spectral and statistic method in the UV-visible wavelengths*, J. Appl. Phys. 103(3), p. 1-10, 2008.

[Pierre 2016] T. Pierre, C. Rodiet, B. Rémy, A. Degiovanni, *Steady-state and transient microscale temperature measurements by multispectral method and photons counting*, Applied Thermal Engineering, 99, p. 343-351, 2016.

[Pierre 2022] Pierre, Thomas, et al. « Simultaneous Estimation of Temperature and Emissivity of Metals around Their Melting Points by Deterministic and Bayesian Techniques ». *International Journal of Heat and Mass Transfer*, vol. 183, février 2022, p. 122077.

[Pierre 2023] Thomas Pierre et al., *Multiple inversion techniques with multispectral pyrometry for the estimation of temperature and emissivity of liquid niobium and 100c6 steel*, Heat Transfer Engineering, accepted for publication.

[Ristic 2004] B Ristic, *et al.*, *Beyond the Kalman filter*, Artech House, Boston, 2004.

[Rodiet 2013] Rodiet, Christophe, et al. *Quantitative InfraRed Thermography Journal*, vol. 10, nº 2, décembre 2013, p. 222-36.

[Rodiet 2015] C. Rodiet, T. Pierre, B. Rémy, A. Degiovanni, *Influence of measurement noise and wavelengths on the temperature measurement of opaque surface with variable emissivity by a multi-spectral method based on the flux ratio in the infrared-ultraviolet range*, High temperatures – High pressures, 44(3), p. 211-226, 2015.

[Rodiet 2016] Rodiet, Christophe, et al. *Infrared Physics & Technology*, vol. 76, mai 2016, p. 444-54.

[Seifter 2001] A Seifter et al. *Microsecond Laser Polarimetry for Emissivity Measurements on Liquid Metals at High Temperatures—Application to Niobium*. International Journal of Thermophysics, vol. 22, nº 5, septembre 2001, p. 1537-47.

[Smith 2000] Smith, J. F., et S. Zheng. « High temperature nanoscale mechanical property measurements ». *Surface Engineering*, vol. 16, nº 2, avril 2000, p. 143-46.

[Sparrow 1978] E. M. Sparrow, R. D. Cess, *Radiation heat transfer*, CRC Editions, Boca Raton, 1978.

[Touloukian 1970] Y S Touloukian, *Thermal radiative properties*, Plenum, New York, 1970.

[Watanabe 2003] Watanabe, Hiromichi, et al. « Phase (Liquid/Solid) Dependence of the Normal Spectral Emissivity for Iron, Cobalt, and Nickel at Melting Points ». *International Journal of Thermophysics*, vol. 24, nº 2, mars 2003, p. 473-88.

[www.hamamatsu.com] https://www.hamamatsu.com/jp/en/product/optical-sensors/pmt/about_pmts.html, seen Mars 13th 2023.

[www.larousse.fr] https://www.larousse.fr/dictionnaires/francais/pyrom%C3%A9trie/65318, seen March 13th 2023.

6. Characterization of thermal properties by non-contact techniques

As already mentioned in Introduction of this document, part of PTR2 has been working for more than twenty years in collaboration with companies specializing in all types of welding or additive manufacturing. One of PTR2 contributions is to perform numerical simulations of welding processes using commercial codes such as Comsol Multiphysics®. These industrial processes being highly multiphysical (thermal, mechanical, hydrodynamic, metallurgical, electromagnetism...), large number of physical properties is required (viscosity, density, surface tension, heat capacity, conductivity...) and over a wide temperature range since matter changes from solid state to liquid state and can reach its boiling point. However, literature is almost mute from liquid state and beyond.

Since 2016, we have developed two high temperature apparatuses. The first one deals with metallic balls aerodynamically levitated, the second one with fixed horizontal plates with of thickness less than a millimetre. In every case, heating is assured by laser, radiative measurements by infrared and visible fast cameras.

So far, we are able to determine two physical parameters with these apparatuses: density and surface tension (thesis of D. Le Maux [Le Maux 2019][Le Maux 2022]). And we are working on estimation of viscosity [Le Maux 2023] and on thermal diffusivity (post-doctoral application of B. Lamien [Lamien 2019], thesis of J Houssein [Houssein 2023]).

Section 6 deals with the use of pyrometers and cameras during the characterization of physical properties of materials and is divided in two sub-Sections. Section 6.1 is dedicated to estimation of thermal diffusivity of metals at solid state but near the melting point [Lamien 2019]. Second 6.2 deals with the other experimental configuration. This time thermal diffusivity estimation is performed through comparison between a temperature-temperature analytical model and experimental measurements [Houssein 2023].

6.1. The estimation of the thermal diffusivity of metals at temperature close to the melting point with the aerodynamic levitation

First part of this section concerns the definition of an experiment of aerodynamic levitation to estimate both thermal conductivity and diffusivity through Bayesian inference, where the theoretical model is a flux-temperature one [Lamien 2019]. The levitation apparatus, briefly introduced in Section 5, is well-detailed in [Le Maux 2022]. Note that I also participate to the estimation with this apparatus of hydrodynamic properties when matter is at liquid state (density, surface tension, and viscosity) but it is not presented in this manuscript. However, readers may refer to the following references: [Le Maux 2019][Le Maux 2022][Le Maux 2023].

6.1.1. Presentation of the levitation apparatus

The experimental device is presented in Figure 6.1 (see also [Le Maux 2019]). Its legend using capital letters in brackets is indicated below. An argon hydrogen mix Ar + 2.5 %vol. H_2 is blown through a 60° convergent-divergent nozzle to levitate an approximately 30 mg sample (about 2 mm of diameter for iron alloys) (A). A first numerical flowmeter Brooks SLA5850S controls the lift gas (B). The levitation part is set in a vacuum chamber equipped with borosilicate viewports (C). The upper window is dedicated to the heating laser (IPG Photonics YLR 300/3000 QCW at 1 070 nm) (D) and pyrometric measurement. The heating laser has a 280 W maximal power in continuous mode. It is equipped with a 500 mm focalization optic slightly defocused to make the aimed spot about 2 mm. A set of mirrors is placed at the upper window and at a lateral one (E) in order to deport the upper and lateral views of the sample to a high-speed camera (F) Phantom VEO-E 310L (see its calibration in Section 5.1.3). A backlighting laser (300 mW, 532 nm diode laser with a beam expander) (G) is placed at the opposite lateral window. The sample is heated up by the laser until it becomes liquid, its temperature is measured by the pyrometer previously detailed in Section 5.1.3.

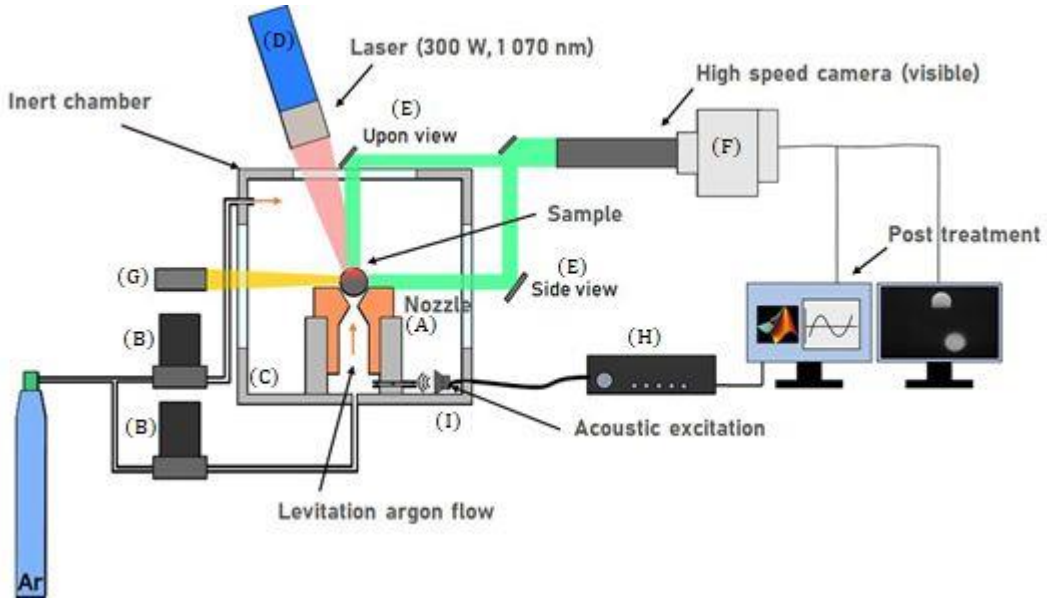

Figure 6.1. Scheme of the complete levitation apparatus.

Other components are present dealing with estimation of surface tension and viscosity. An acoustic solicitation is used to make oscillate the liquid sample: a sinusoidal signal is generated, amplified (H) and transformed into pressure waves thanks to a speaker (I). The second flowmeter (B) controls a lateral gas jet to force the drop rotation along the vertical axis to facilitate frequency analysis. Finally, an oxygen analyzer measures residual oxygen in the pipe of the levitation gas.

During experiment for the estimation of thermal diffusivity in Section 6.1.2, the six-wavelength pyrometer would be placed next to the laser. It is not shown in Figure 6.1.

6.1.2. Theoretical model of the sphere in the levitation apparatus and results

The proposed methodology is based on the front-face flash method with laser excitation and contactless transient flux measurements available from a multispectral pyrometer [Lamien 2019]. However, the parameter estimation presented at the end of this Section is based on synthetic data and not from experimental ones. Based on Figure 6.2, the mathematical formulation of the heat conduction problem in dimensionless form in spherical coordinates (r, θ, φ), with transformed polar angle $\mu = \cos\theta$ and associated initial and boundary conditions, is given by:

$$\frac{1}{\alpha^*}\frac{\partial T^*(r^*,\mu,\tau)}{\partial r^*}=\frac{1}{r^{*2}}\frac{\partial}{\partial r^*}\left(r^{*2}\frac{\partial T^*(r^*,\mu,\tau)}{\partial r^*}\right)+\frac{1}{r^{*2}}\frac{\partial}{\partial \mu}\left[(1-\mu^2)\frac{\partial T^*(r^*,\mu,\tau)}{\partial \mu}\right] \tag{6.1}$$

$$\begin{aligned}k^*\frac{\partial T^*(1,\mu,\tau)}{\partial r^*}+Bi_{rad}[T^{*4}(1,\mu,\tau)-T_\infty^{*4}]+Bi_{cv}[T^{*4}(1,\mu,\tau)-T_\infty^*]\\ =\kappa_{\lambda,laser}q_0^* f(\mu,\tau,\mu_0,\tau_h)\end{aligned} \tag{6.2}$$

$$T^*(r^*,\mu,0)=1 \tag{6.3}$$

with the dimensionless measured radiative flux given by:

$$\Phi_{s,i}^*(\tau)=\frac{\varepsilon_{\lambda,pyro}F_{d1-2}}{q_{ref}S_{ref}}\int_0^\infty\int_{S_{ref}} f_i(\lambda)I^0(\lambda,T)d^2S_k d\lambda \tag{6.4}$$

The following dimensionless parameters are introduced for the model formulation:

$$T^*=\frac{T(r,\mu,t)}{T_0} \tag{6.5}$$

$$T_\infty^*=\frac{T_\infty}{T_0} \tag{6.6}$$

$$r^*=\frac{r}{R} \tag{6.7}$$

$$\tau=\frac{\alpha_{ref}t}{R^2} \tag{6.8}$$

$$\alpha^*=\frac{\alpha}{\alpha_{ref}} \tag{6.9}$$

$$k^*=\frac{k}{k_{ref}} \tag{6.10}$$

$$Bi_{cv}=\frac{h_{cv}R}{k_{ref}} \tag{6.11}$$

$$Bi_{rad}=\frac{\varepsilon\sigma R T_0^3}{k_{ref}} \tag{6.12}$$

$$q_0^*=\frac{q_0}{q_{ref}} \tag{6.13}$$

$$\Phi_{s,i}^{*} = \frac{\Phi_s}{q_{ref} S_{ref}} \tag{6.14}$$

$$q_{ref} = \frac{k_{ref} T_0}{R} \tag{6.15}$$

$$S_{ref} = 2\pi R^2 \left(1 - \mu_{spot}\right) \tag{6.16}$$

and the subscript *ref* denotes reference value for the material being characterized. These reference values can be taken from literature for similar materials. S_{ref} is a reference surface, given by the area of the spherical cap observed by the pyrometer around the symmetry axis. In the formulation of Eq. (6.2), boundary heat source term $f(\mu, \tau, \mu_0, \tau_h)$ represents the spatio-temporal profile of the laser excitation written in terms of transformed polar angle μ and of dimensionless time τ. The functional form of $f(\mu, \tau, \mu_0, \tau_h)$ is written in terms of the product of functions $g(\mu, \mu_0)$ and $u(\tau, \tau_h)$, representing the spatial and temporal profiles, respectively. These functions are given as:

$$g(\mu, \mu_0) = \exp\left[-2\frac{(1-\mu^2)}{(1-\mu_0^2)}\right] \tag{6.17}$$

for the spatial distribution, while the temporal profile is either a square pulse represented by:

$$u(\tau, \tau_h) = \frac{1}{2}\{1 + \mathrm{erf}[\phi(\tau - \tau_{\uparrow})]\} - \frac{1}{2}\{1 + \mathrm{erf}[\phi(\tau - \tau_{\downarrow})]\} \tag{6.18}$$

or an exponential decaying pulse:

$$u(\tau, \tau_h) = \frac{\tau^2}{4\tau_h^2} \exp\left(2 - \frac{\tau}{\tau_h}\right) \tag{6.19}$$

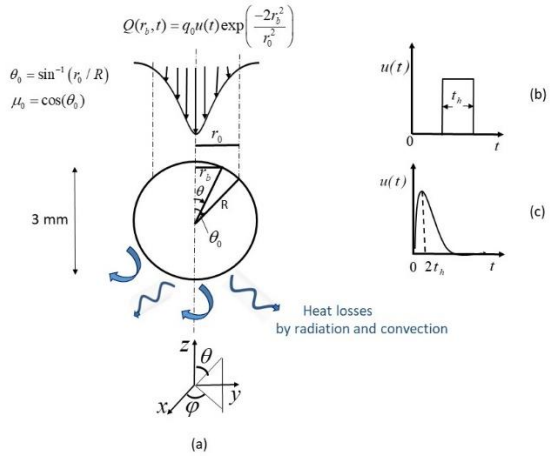

Figure 6.2. Scheme of the metallic ball.

In the above equations, ϕ is a smoothing parameter, while subscripts " $\uparrow$ "and " $\downarrow$ " refer to the ascent and descent times of the square pulse. For solution of the complete model given by Eq. (6.1), finite element method was used through COMSOL Multiphysics® 4.3b commercial package.

For the purpose of speeding-up the inverse problem solution, a reduced model is proposed. This reduced model involves linear boundary conditions, with a combined heat transfer coefficient that takes into account heat losses by radiation and convection. Analytical solution of the heat conduction problem is obtained through classical integral transform technique [Ozisik 1993]. In order to reduce the importance of nonhomogeneous boundary condition on the convergence of the series solution, solution of the problem (not presented here) is defined as the sum of solutions of a quasi-steady state heat conduction problem with nonhomogeneous boundary condition (*filtering problem*) and a transient heat conduction problem with homogeneous boundary conditions (*filtered problem*) by assuming [Cotta 1997][Cotta 2017]:

$$T^*(r^*, \mu, \tau) = T_H^*(r^*, \mu, \tau) + T_F^*(r^*, \mu, \tau) \tag{6.20}$$

Direct problem, associated with the above physical problem consists in determining the temperature distribution at discrete angular positions on the surface seen by the pyrometer and the corresponding fluxes collected by the multispectral pyrometer, from the knowledge of initial, boundary conditions, heat source, geometry, and thermophysical properties of the solid metal sample (Figures 6.3 and 6.4).

Regarding the inverse problem, the objective is the estimation of thermal diffusivity of the solid metal from measured fluxes by the multispectral pyrometer.

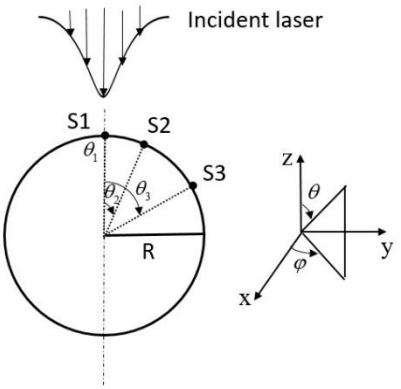

Figure 6.3. Surfaces observed by the pyrometer.

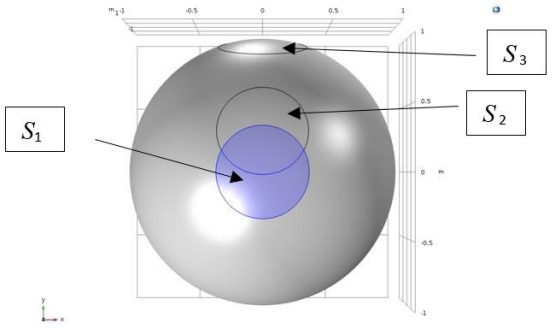

Figure 6.4. Surfaces observed by the pyrometer.

However, the lack of knowledge and/or uncertainties on parameters appearing in the mathematical formulation, such as thermal conductivity of the solid metal, its total hemispherical emissivity, heat losses and laser parameters (irradiance, spot size, pulse width), must be taken into account. A sensitivity analysis is later performed to determine whether these parameters can be estimated together with the parameters of interest.

The sensitivity analysis is performed with the complete forward model and the effects of:

- the laser beam size incident on the steel ball;
- the temporal profile of the pulse;
- and the position of the surface seen by the pyrometer (surface S1 centred on $\theta_1 = 0°$, surface S2 centred on $\theta_2 = 20°$, surface S3 centred on $\theta_3 = 60°$)

as illustrated in Figures 6.3 and 6.4, were investigated. The parameters to estimate are the following:

$$\boldsymbol{\beta}^{\mathbf{T}} = \left[\alpha \; k \; Bi_{rad} \; \varepsilon_{\lambda,pyro} \; \kappa_{\lambda,laser} \; q_0^* \; Bi_{cv} \; f_i \; F_{d1-2}\right] \tag{6.21}$$

Note that f_i is H_{Mi} in Figures 6.5 to 6.9. In order to perform sensitivity analysis, the maximum temperature increase of the heated surface was set to 50 K to have a reasonable approximation of the assumption of constant physical properties with respect to temperature variation. The sensitivity coefficients computed for the different wavelengths of the multispectral pyrometer presented the same behaviour, with the largest flux magnitudes obtained for the wavelength $\lambda = 1\,550$ nm. Therefore, the analysis below is presented only for this wavelength. Moreover, for the case under study, flux measurements obtained at the wavelength $\lambda = 1\,550$ nm and $\lambda = 940$ nm are the only useful information, since the lower measured threshold power of the multispectral pyrometer is 50 nW.

- The influence of the incident laser beam size on the sensitivity coefficients is examined for beam diameters of 1 mm and 2.6 mm, for square pulses with $P = 13$ W and $\tau_h = 3$ ms, as well as for $P = 30$ W and $\tau_h = 15$ ms. These values were chosen so that the maximum temperature increase of the heated surface was limited to 50 K. Figures 6.5 and 6.6 present the transient behaviour of the sensitivity coefficients of the different model parameters, computed by considering measurements taken over the surface S_1. The dimensionless flux is also presented in Figures 6.5 and 6.6. It can be noticed in these figures that the sensitivity coefficients of thermal diffusivity and thermal conductivity obtained for the incident laser beam size of 2.6 mm are of larger magnitudes than those

corresponding to the laser beam size of 1 mm. This is due to the fact that more energy is provided to the steel ball in the case of an incident laser beam size of 2.6 mm for the same maximum temperature increase of 50 K. The beam size of 2.6 mm is therefore favourable for estimation of the parameters of interest, because the sensitivity coefficients present large magnitudes. It can be observed in Figures 6.5 and 6.6 that the sensitivity coefficients of the parameters of interest (thermal diffusivity and thermal conductivity) are an order of magnitude smaller than the dimensionless flux and than the sensitivity coefficients of the emissivity $\varepsilon_{\lambda,pyro}$, the form factor F_{d1-2} and the flux losses f_i.

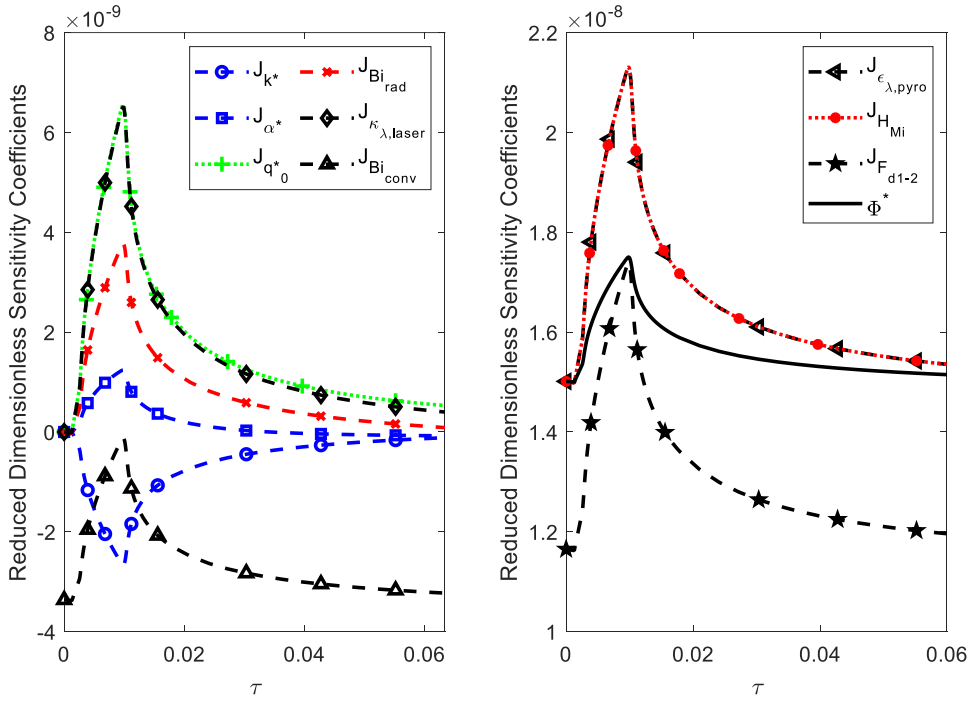

Figure 6.5. Effect of the incident laser beam size on sensitivity coefficients: 1 mm and surface S_1.

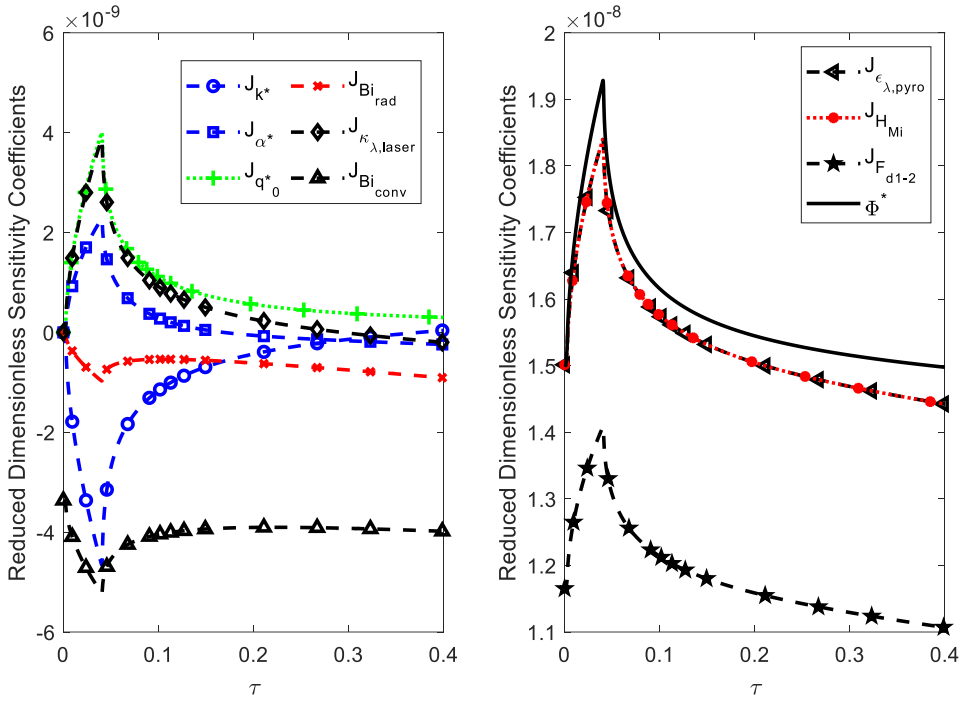

Figure 6.6. Effect of the incident laser beam size on sensitivity coefficients: 2.6 mm with a square pulse.

The analysis of the sensivitity coefficients suggests the possibility of simultaneously estimating the thermal diffusivity and the thermal conductivity of the steel ball. However, the remaining model parameters have to be known, since they are correlated and the magnitudes of their sensitivity coefficients are one order larger or of the same order of those for the parameters of interest.

- For the analysis of the effect of the position of the surface where the measurements are taken by the pyrometer on the sensitivity coefficients, a square pulse of power $P = 30$ W, with pulse duration $\tau_h = 15$ ms is considered, with the laser beam diameter of 2.6 mm. Figures 6.5, 6.7, and 6.8 present the transient behaviour of the sensivitiy coefficients computed at surfaces S_1, S_2, and S_3, respectively. In these figures the magnitudes of the sensivity coefficients calculated at surface S_1 are the largest. The sensitivity coefficients computed at surface S_2 present a similar behaviour, but with magnitudes smaller than those at S_1, in particular those of the thermal diffusivity and of the thermal conductivity. Although the sensitivity coefficients of thermal diffusivity and of thermal conductivity computed at surface S_3 seem less correlated, they are two orders of magnitude smaller than the flux observed by the pyrometer.

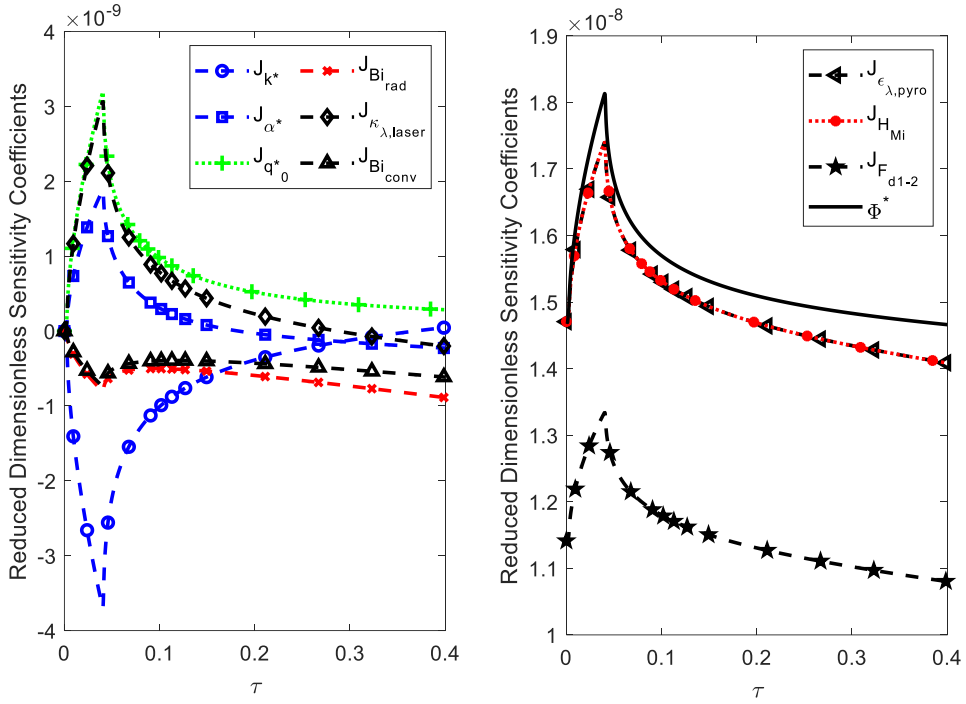

Figure 6.7. Effect of the position of the surface seen by the pyrometer on sensitivity coefficients: surface S_2.

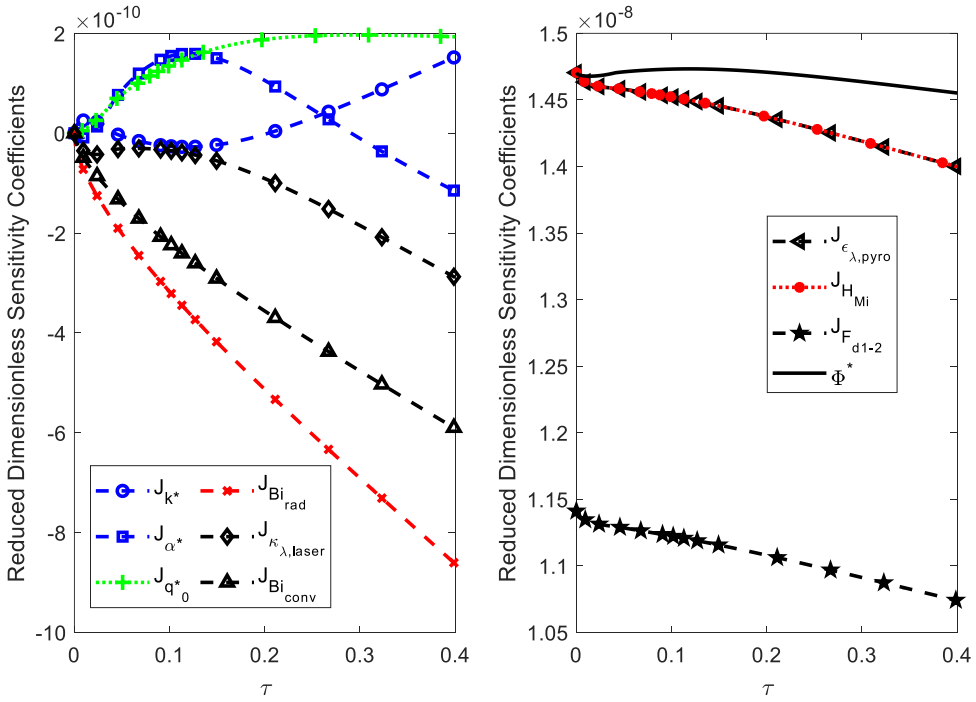

Figure 6.8. Effect of the position of the surface seen by the pyrometer on sensitivity coefficients: surface S_3.

The measurements of the flux obtained at surface S_1 are therefore more appropriate for the estimation of the parameters of interest, because the sensitivity coefficients of the parameters of interest present large magnitudes.

- Regarding the effect of the temporal profile of the incident laser pulse on the sensitivity coefficients, a square pulse and an exponentially decaying pulse were examined (Eqs. (6.18) and (6.19)). Figure 6.9 presents the sensitivity coefficients for the case of an exponentially decaying pulse (P= 30 W, τ_h = 15 ms), while the case of a square pulse is given in Figure 6.6. In these figures the case of a square pulse presents sensitivity coefficients of the same magnitude with those of the exponentially decaying pulse. Moreover, one can note in Figure 6.9 that thermal diffusivity and thermal conductivity are strongly correlated in the case of the exponentially decaying pulse. It is also clear from these figures that thermal diffusivity and thermal conductivity tend to be uncorrelated once the heating is stopped.

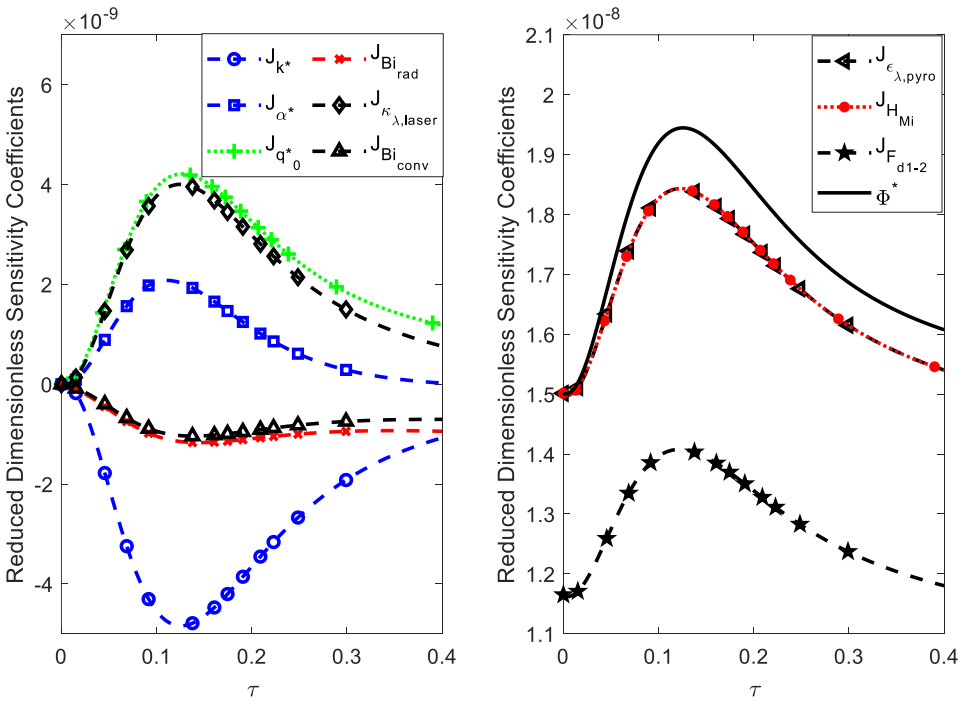

Figure 6.9. Effect of the temporal profile of the pulse on sensitivity coefficients for an exponentially decaying pulse.

6.1.3. Results and discussion

For the solution of the inverse problem, techniques within Bayesian framework of statistics are used (Section 5.3.4): namely Gauss-Newton minimization of the maximum a

posteriori objective function and the Markov chain Monte Carlo method, coded in the form of Metropolis-Hastings algorithm. Analysis of the sensitivity coefficients with respect to the model parameters reveals that thermal diffusivity and thermal conductivity of the levitated metal sample can be estimated, provided that other auxiliary parameters are known. These auxiliary parameters are correlated and with magnitude of their sensitivity coefficients comparable to those of the sought parameters.

For the solution of inverse problem of simultaneous estimation of thermal diffusivity and thermal conductivity of the steel sphere, prior probability densities associated to thermal diffusivity and thermal conductivity given in Table 6.1 were used.

Figure 6.10 presents the states of Markov chains for thermal conductivity and thermal diffusivity. One can note a rapid convergence of the states of Markov chain to an equilibrium distribution around the exact values of the sought parameters.

Table 6.1: Prior probability densities used in the computation of the approximation error.

Property / Parameter	Dimensionless Parameter	Prior Distribution	Mean	Standard deviation
Thermal diffusivity	α^*	Gaussian	$\bar{\alpha}^* = 1.09\alpha^*$	$0.15\bar{\alpha}^*$
Thermal conductivity	k^*	Gaussian	$\bar{k}^* = 1.09k^*$	$0.15\bar{k}^*$
Irradiance	q_0^*	Gaussian	$\bar{q}_0^* = q_0^*$	$0.05\bar{q}_0^*$
Radiative Biot number	Bi_{rad}	Gaussian	$\overline{Bi}_{rad} = 1.05Bi_{rad}$	$0.05\overline{Bi}_{rad}$
Absorptivity at $\lambda_{laser} = 1\,060$ nm	$\kappa_{\lambda,laser}$	Gaussian	$\bar{\kappa}_{\lambda,laser} = \kappa_{\lambda,laser}$	$0.05\bar{\kappa}_{\lambda,laser}$
Normal spectral emissivity at λ_{filter}	$\varepsilon_{\lambda,pyro}$	Gaussian	$\bar{\varepsilon}_{\lambda,pyro} = 1.05\varepsilon_{\lambda,pyro}$	$0.05\bar{\varepsilon}_{\lambda,pyro}$
Amplitude correction	f_i	Gaussian	$\bar{f}_i = 1.05f_i$	$0.1\bar{f}$
Form factor	F_{d1-2}	Gaussian	$\bar{F}_{d1-2} = 1.05F_{d1-2}$	$0.1\bar{F}_{d1-2}$
Convective Biot number	Bi_{cv}	Gaussian	$\overline{Bi}_{cv} = 1.05Bi_{cv}$	$0.1\overline{Bi}_{cv}$

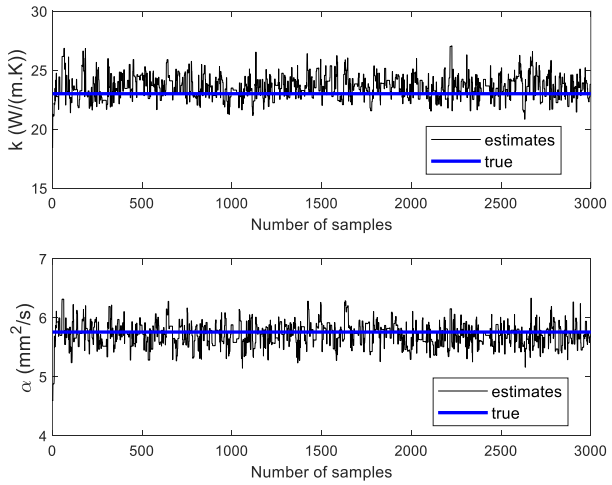

Figure 6.10. States of Markov Chain for thermal diffusivity and for thermal conductivity.

Figures 6.11 and 6.12 compare prior distributions of the parameters and the posterior distributions obtained from MCMC samples. The histograms of the marginal posteriors for thermal diffusivity and thermal conductivity are also shown in this figure. The first 1 000 states of Markov chain were discarded (burn-in period) for the computation of statistics. One can note in these figures that information provided by measurements has resulted in a considerable reduction of the initial uncertainties on thermal diffusivity and thermal conductivity. Moreover, the most likely values of these parameters are concentrated around their exact values.

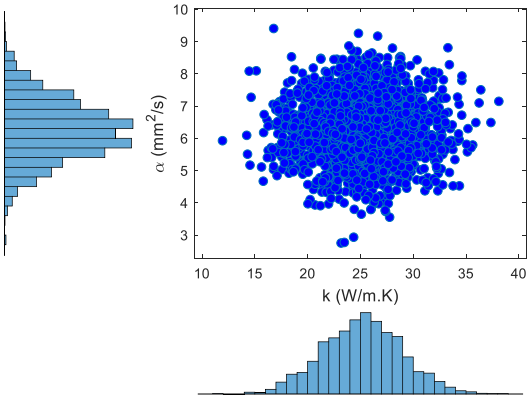

Figure 6.11 Scatter distribution of the samples representing: prior distribution with associated marginal (a).

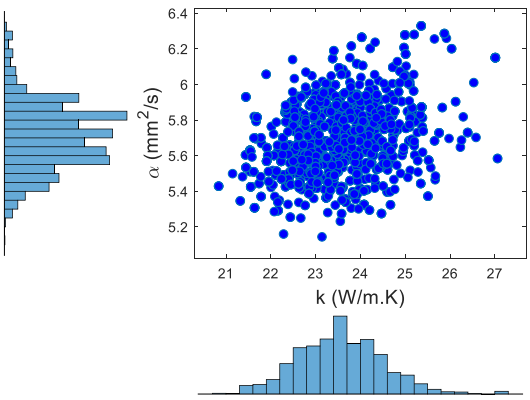

Figure 6.12. Scatter distribution of the samples representing: the posterior distribution with associated marginal (b).

6.1.4. Partial conclusion

Section 6.1 presented a study concerning the possibility to estimate thermal diffusivity and thermal conductivity of solid metallic balls at temperature close to the melting point when submitted to aerodynamic levitation and heated by laser. The direct model was a flux-temperature model with numerous unknown unwanted parameters such as the part of the flux absorbed by the ball. Sensitivity studies showed correlation between parameters whatever the position of the radiative measurements around the ball.

Parameter estimation has been performed through Bayesian inference. Estimation tests with priors of weak uncertainties on the unknown parameters showed that estimation of both thermal conductivity and diffusivity can be achieved under the condition that the other parameters are imposed or very well-known.

A possible perspective of this study would be the use of a flux-flux model, where the first one is the input and the second one the observable. A more appropriate flux-flux model where the fluxes are recorded by the same camera (or temperature-temperature model where fluxes are converted into temperatures) would be possible under the condition that the emissivity is known. This last point concerns temperature-emissivity estimation dealt in Section 5. However, another question lays on the feasibility of the experiment, that has never been conducted for estimation of diffusivity and thermal conductivity.

6.2. The estimation of the thermal diffusivity of metals at temperature close to the melting point with the second apparatus

6.2.1. The apparatus with the horizontal plate

The new developed experimental set-up is slightly different from the previous one (Figures 6.13 and 6.14) [Houssein 2023]. With the same laser, the front face of a thin square sample is first heated, then it is irradiated by a short high-power pulse. The studied samples are in the form of metal sheets. The large metal sheets have a measured thickness of approximately 0.23 mm and are then cut into smaller square pieces adapted to the apparatus (approximately 20 mm × 20 mm).

In order to maximize the area of the homogeneous temperature zone, and therefore reduce the radial temperature gradients, the initial heating stage is done at a relatively low power (70 W) and takes up to 30 seconds. The duration of the pulse is about 10 ms at a power of 270 W.

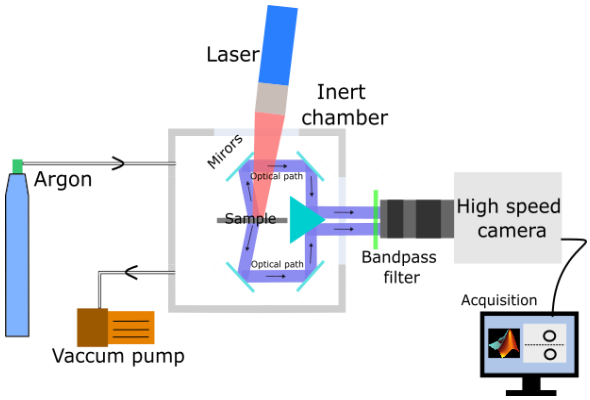

Figure 6.13. Sketch of the experimental set-up.

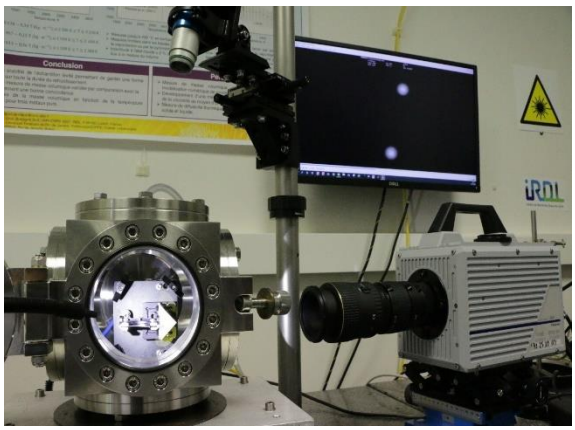

Figure 6.14. Experimental set-up. The four mirrors system is contained inside the inert chamber. High-speed camera is on the right and laser is above the inert chamber.

The inert chamber contains four gold coated mirrors (ThorLabs ME1-M01) that are symmetrically arranged around the sample, so that at the faces of the prismatic mirror, we get a simultaneous view of both faces of the sample.

The high-speed thermography technique [Altenburg 2020][Muller 2013] is used to measure simultaneously temperature responses at both front and rear surfaces. The collected signal is recorded at 10 000 frames per second, with a resolution of 640 × 1008 pixels. A spatial calibration is made to convert distance measurements from pixel into millimetres. An 880 nm band pass filter (ThorLabs FB 880-70) is used to narrow the detected radiation to a smaller band. The choice of the operating wavelength is made in a way to assure maximum signal transmission efficiency and to limit disturbing influences from laser beam. The laser and the camera are synchronized and controlled by an in-house program.

At the end of each experiment, we get a gray scale video. Figure 6.15 illustrates the front and rear heated faces visible in one image thanks to the six mirrors. The gray scale intensity of each heat spot is between 0 and 255 and is proportional to the pixel illumination. The gray scale frame is converted into a temperature map (Figure 6.16) using the signal-temperature calibration curve. The estimation is made at the centre of the heat spot ($r = 0$) where the program extracts the gray scale intensity evolution along an evaluation square area of 5 × 5 pixels around the centre point to get a smooth temperature profile.

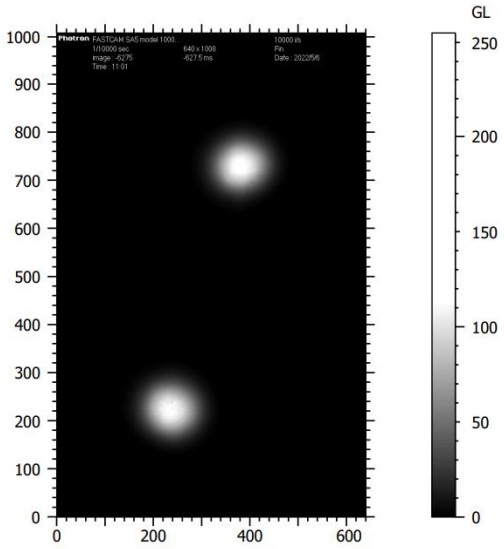

Figure 6.15. Gray-scaled front and rear faces heat field.

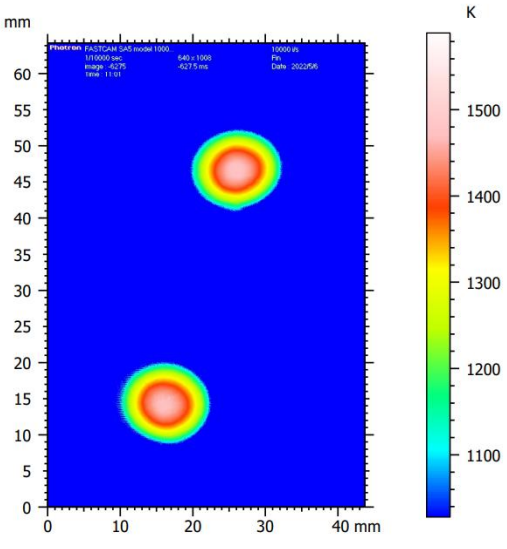

Figure 6.16. Temperature map (K) of the front and rear faces heat field.

6.2.2. Theoretical model with the horizontal plate

As the experiment presents an axisymmetric geometry, the thermal problem is formulated mathematically in 2D cylindrical (r-z) coordinates. The metallic samples are assumed homogeneous and isotropic, of thickness e, and radius R. The heat equation of the sample receiving a heat flux $\varphi_0(r,t)$ involved here and the initial and boundary conditions are given by Eqs. (6.22)-(6.28), assuming constant thermal properties:

$$\frac{\partial^2 T(r,z,t)}{\partial r^2}+\frac{1}{r}\frac{\partial T(r,z,t)}{\partial r}+\frac{\partial^2 T(r,z,t)}{\partial z^2}=\frac{1}{\alpha}\frac{\partial T(r,z,t)}{\partial t} \tag{6.22}$$

$$T(r,z,0)=T_{init} \tag{6.23}$$

$$\frac{\partial T(0,z,t)}{\partial r}=0 \tag{6.24}$$

$$T(R,z,t)=T_{iint} \tag{6.25}$$

$$-k\frac{\partial T(r,0,t)}{\partial z}=\varphi_0(r,t)-h_0[T(r,0,t)-T_\infty] \quad r\le r_0 \tag{6.26}$$

$$k\frac{\partial T(r,0,t)}{\partial z}=-h_0[T(r,0,t)-T_\infty] \quad r_0<r\le R \tag{6.27}$$

$$-k\frac{\partial T(r,e,t)}{\partial z}=h_e[T(r,e,t)-T_\infty] \tag{6.28}$$

where $\alpha=k/(\rho c_p^m)$ is the thermal diffusivity, k is the thermal conductivity, ρ is the density, c_p^m is the specific heat, r_0 is the heat flux radius, T_{init} is the initial temperature, and T_∞ is the room temperature including the gas and the enclosure temperatures, that are assumed constant regarding the large size of the enclosure, the short experiment duration (less than 30s) and a laser beam focusing only on the centre of the sample. Convective and radiative heat exchanges are assumed linear and described by the coefficients h_0 and h_e at locations $z=0$ and e, respectively.

Solution of this problem is given in Laplace domain using the quadrupole formalism [Maillet 2000]. For sake of clarity, the mathematical formulation is detailed in Appendix A of [Houssein 2023]. The expressions of temperatures at locations $z=0$ and $z=e$ are:

$$\theta_0(r,s)=\sum_{n=1}^{\infty}\frac{(A+h_eB)(\Phi_0+Y)-X(C+h_eD)}{(C+h_eD)+h_0(A+h_eB)}\frac{J_0(\gamma_n r)}{\frac{R^2}{2}J_1^2(\gamma_n R)} \tag{6.29}$$

$$\theta_e(r,s) = \sum_{n=1}^{\infty} \frac{\Phi_0 + Y + h_e X}{(C + h_e D) + h_0(A + h_e B)} \frac{J_0(\gamma_n r)}{\frac{R^2}{2} J_1^2(\gamma_n R)} \tag{6.30}$$

θ_0, θ_e, and Φ_0 are, respectively, the expression of temperature at positions $z = 0$ and e and the heat flux φ_0 following Laplace and Hankel integral transforms. The coefficients *A*, *B*, *C* and *D* define the quadrupole matrix [Maillet 2000]. They depend on the Laplace parameter *s*, the sample thickness e, and the thermophysical properties of the material. J_ν is the Bessel function of first kind of order ν. *X* and *Y* are given by:

$$X = \frac{(T_{init} - T_\infty)}{s} [cosh(\omega_n e) - 1] \frac{R J_1(\gamma_n R)}{\gamma_n} \tag{6.31}$$

$$Y = \frac{\rho c_p^m}{\omega_n} (T_{init} - T_\infty) sinh(\omega_n e) \frac{R J_1(\gamma_n R)}{\gamma_n} \tag{6.32}$$

The 2D average temperatures $\tilde{\theta}_0(s)$ and $\tilde{\theta}_e(s)$ considering an area of radius r_a centered around $r = 0$ can be obtained knowing that, from Eq. (6.29) and Eq. (6.30) that:

$$\frac{1}{\pi r_a^2} \int_0^{r_a} 2\pi J_0(\beta_n r) r dr = \frac{2 J_1(\gamma_n r_a)}{\gamma_n r_a} \tag{6.33}$$

From Eq. (6.29) and Eq. (6.30), once removed the radial dependency, the 1D temperature expressions become:

$$\theta_0(s) = \frac{(A + h_e B)(\Phi_0 + Y) - X(C + h_e D)}{(C + h_e D) + h_0(A + h_e B)} \tag{6.34}$$

$$\theta_e(s) = \frac{\Phi_0 + Y + h_e X}{(C + h_e D) + h_0(A + h_e B)} \tag{6.35}$$

In this case *X* and *Y* are computed in the same way but without the *dr* integration. The experimental originality of this work lays on the simultaneous visualization of both rear and front faces of the sample with the same camera. Therefore, a model is presented here where the front face temperature is the input data and the rear face temperature the observable [Jannot 2009][Maillet 2013][Jannot 2018] [Jannot 2020][Pierre 2022]. This temperature-temperature model allows to get rid of the knowledge of the heat flux and the front face heat exchange coefficient. From the quadrupole formalism, link between both front and rear face temperatures is given by Eq. (6.36), whatever the 1D or 2D situations considered:

$$T^{th}(0,e,t) = T^{exp}(0,0,t) \otimes \mathcal{L}^{-1}\left[\sum_{n=1}^{\infty} \frac{1}{cosh(\omega_n e) + \frac{Bi}{\omega_n e} sinh(\omega_n e)}\right] + L\mathcal{L}^{-1}\left[\sum_{n=0}^{\infty} \frac{X}{cosh(\omega_n e) + \frac{Bi}{\omega_n e} sinh(\omega_n e)}\right] \quad (6.36)$$

where $Bi = he/k$ is the Biot number and $\mathcal{L}^{-1}$ represents inverse Laplace transform obtained through numerical procedure such as presented in [Stehfest 1970][de Hoog 1982]. This procedure is also used to express the temperature from Laplace space to the time space for Eqs. (6.29)-(6.35).

Figure 6.17 shows that there is no significant difference between 1D (6.29) and 2D (6.34) front face temperatures, except at the very first time due to Laplace numerical inversion. On the contrary, there is a difference between 1D and 2D models for the rear face.

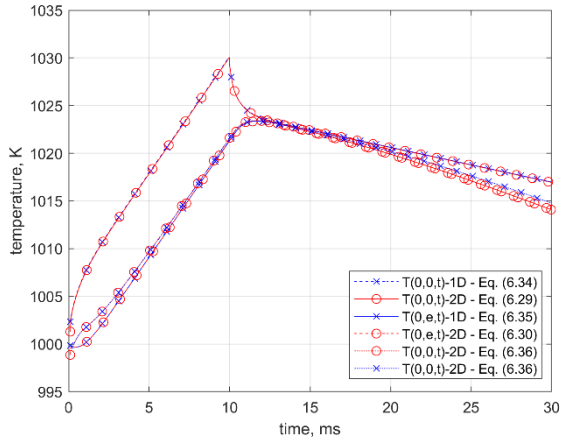

Figure 6.17. Temperatures versus time at front ($z = 0$) and rear ($z = e$) faces of the sample: 1D (cross) and 2D (circle).

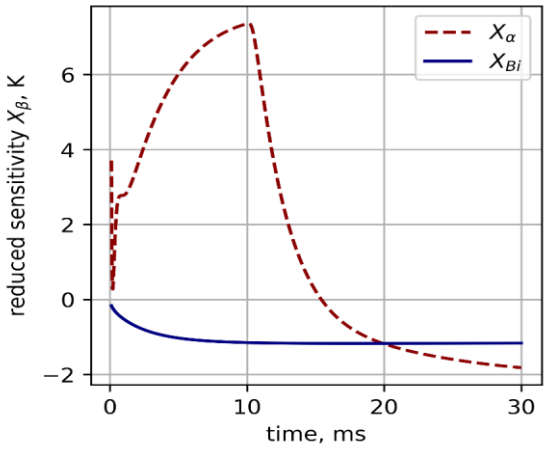

Figure 6.18. Evolution of $\mathbf{X_\beta}$ over time.

In Eq. (6.36), the transmittances between brackets are functions of the parameter of interest: thermal diffusivity α and Biot number Bi. The estimation procedure is based on minimization of the quadratic error between experimental and theoretical rear face temperatures (6.37) with an ordinary least square procedure coupled with a Levenberg-Marquardt optimization [More 1978]. In Eq. (6.37), $\boldsymbol{\beta} = [\alpha, Bi]^T$ and the subscript $j = 1,...$

M represents the time vector. The reduced sensitivity coefficient $\mathbf{X}_{\boldsymbol{\beta}}$ is estimated as described by Eq. (6.38).

$$\sum_{k=1}^{M}\left[\boldsymbol{T}^{\boldsymbol{exp}}(0,e,t_k)-\boldsymbol{T}^{\boldsymbol{th}}(0,e,t_k,\boldsymbol{\beta})\right]^2 \tag{6.37}$$

$$\mathbf{X}_{\boldsymbol{\beta}}=\boldsymbol{\beta}\frac{\partial \mathbf{T}^{\mathbf{th}}(0,0,t)}{\partial \boldsymbol{\beta}} \tag{6.38}$$

Figure 6.18 presents the evolution of $\mathbf{X}_{\boldsymbol{\beta}}$ over time calculated with the same input parameters as in Figure 6.17. Both evolutions of $\mathbf{X}_{\boldsymbol{\beta}}$ behave differently. Thus, thermal diffusivity and Biot number can be estimated with a good level of confidence. The amplitude of X_α is higher than X_{Bi}'s, which becomes constant very quickly, meaning that transmittivities in Eq. (6.36) tend to become insensitive to Biot number a short time during the laser pulse.

6.2.3. Results and discussion

Example of estimation is presented in Figure 6.19 for pure iron and stainless steel 304. The video recorded by the experimental apparatus is used to get temperature rise curve at the centre zone of each heat spot by converting gray level into temperature. Estimated temperature versus time at the rear surface fits well with experimental rear surface temperature, with a highest variation in the residuals less than 1 K. As the residuals mean is close to zero, and for a sake of clarity, residuals in Figure 6.19 are shifted of a value equal to the initial rear face temperature.

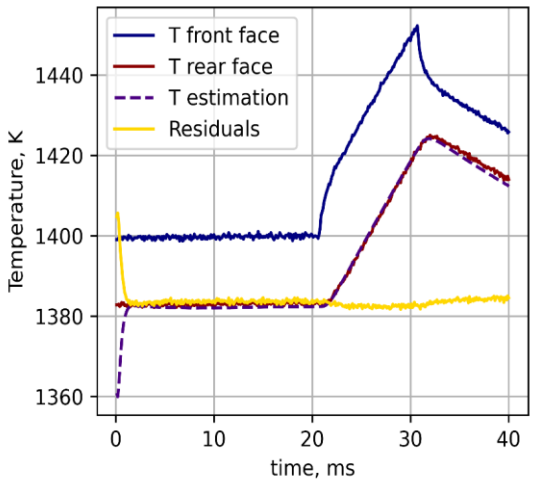

Figure 6.19. Estimated temperature profile and residuals curve over time.

Figures 6.20 and 6.21 show the diffusivity estimation results from stainless steel 304 and iron for a temperature range between 1 300 K and 1 600 K. Results are compared with data from literature [Kim 1975][Touloukian 1977a][Mills 2002]. For stainless steel 304, the estimated diffusivity values lie within the 10 % error range proposed by [Touloukian 1977a] while for iron samples, the diffusivity values are more scattered but still close from data published in literature. In the case of alloys, we suppose that small differences in the chemical components proportion may influence thermophysical characterization results.

Two major error sources influence our results. The first one is the uncertainty related to the sample thickness, a property which is rather hard to measure for very thin samples. The second one is related to the assumed radiative properties, *i.e.* the emittance, of iron samples used to produce the initial signal-temperature calibration curve (see Section 5.1.3.) and therefore it leads to temperature measurement errors.

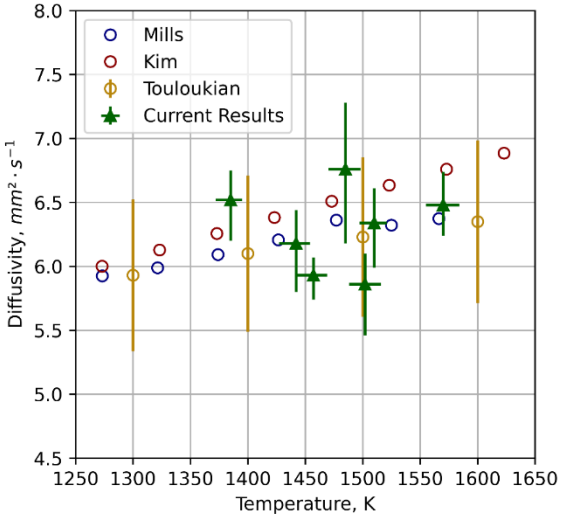

Figure 6.20. Thermal diffusivity of stainless steel 304 and comparison with literature.

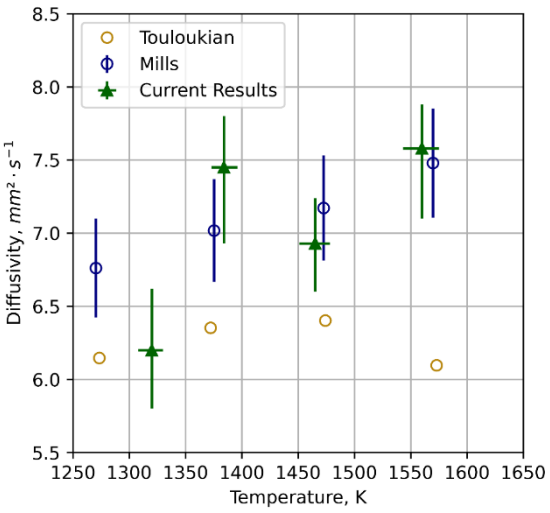

Figure 6.21. Thermal diffusivity for pure iron and comparison with literature.

To address the first error source, uncertainty in the thickness value, first we compute thickness variation induced by thermal expansion at 1 400 K. The coefficients of thermal expansion are taken from [Touloukian 1977b]. For stainless steel 304, a thickness variation of 5 µm leads to a maximum variation in the estimated diffusivity of 9.8 %. On

the other side, a 10 % variation in the assumed emittance value during calibration, leads to an average temperature difference of 13 K and 14 K for iron and steel. In fact, for such a small temperature variation, it can be assumed that any change in the thermophysical properties is negligible, and therefore the high-speed thermography technique can be efficiently used to measure temperature in a laser flash experiment. At the same time, extra caution must be kept while measuring the thickness of the sample, as a very small variation in this value can significantly shift the estimation results.

In order to further test robustness of the proposed method, we cross check estimation results for iron and steel in Table 6.2, using the proposed analytical solution. With the 1D quadrupole model, estimated parameter vector consists of two dimensionless numbers: Fourier and Biot with $Fo = \alpha/e^2$. The advantage of Fourier number is to estimate thermal diffusivity regardless the thickness, a parameter of great influence and which is hard to measure in our case. Setting the thickness value to 230 µm diffusivity estimated by the 1D quadrupole method is smaller than the value given by the 2D model. In fact, for the same heat flux condition on the front face and to get the same heat transfer rate for both models, *i.e.* the same rear face temperature, the diffusivity estimated by the 1D model is smaller, given that the latter does not account for the radial heat losses.

Table 6.2. Results of estimation for iron and steel using three different direct models.

	Iron (T = 1 385 K)				Steel (T = 1 502 K)			
Method	α (mm²·s⁻¹)	Bi × 10⁻³	Fo	t_{estim} (s)	α (mm²·s⁻¹)	Bi × 10⁻³	Fo	t_{estim} (s)
1D	7.30	9.45	138	5.7	5.52	7.15	104.3	5
2D	7.45	9.58	140.8	13	5.86	7.24	110.7	18

On the side, it is possible to compute a global heat exchange coefficient h, accounting for both convection and radiation heat transfers from estimated Biot number. Thickness e is assumed to be 230 µm and thermal conductivity values are taken from literature (k_{Fe} = 33.1 W·m⁻²·K⁻¹ and k_{Steel} = 31.7 W·m⁻²·K⁻¹). For the 2D quadrupole, this coefficient is 1 380 W·m⁻²·K⁻¹ and 998 W·m⁻²·K⁻¹ for iron and steel, respectively. The large value of the convection coefficient is primarily due to the important radiative heat

transfer at high temperature and in a second place to the uncontrolled high-speed argon flow into the inert chamber. Moreover, the method has shown a small sensitivity to Biot number variation.

6.2.4. Partial conclusion

Section 6.2 presented the other study dedicated to estimation of thermal diffusivity of solid metallic plates at temperature close to the melting point when submitted to laser heating. The direct model was a temperature-temperature model with two parameters to estimate: thermal diffusivity and heat losses. Sensitivity study showed decorrelation between parameters.

The originality of the experimental configuration with the mirrors and the visible high-speed camera allowed the possibility to observe simultaneously both sides of the plate. The use of the high-speed camera also allowed to record temperature fields at a frequency of 1 000 frames per second. This speed was a necessity if we wanted to see the in-depth heat propagation with a plate of about 200 µm of thickness.

Parameter estimation has been successfully performed by ordinary least-squares coupled with Levenberg-Marquardt algorithm by minimization of the quadratic error between experimental and theoretical temperatures. Estimated thermal diffusivity for the tested metals is consistent with data encountered in literature.

6.3. Conclusion

Section 6 was mainly dedicated to estimation of thermal diffusivity of solid metallic samples at temperature close to the melting point. This subject was a first step to a more general project in characterization of liquid metal as described in introduction of Section 6. For that, two experimental apparatuses have been developed: the first one heats with a laser millimetric ball once in aerodynamic levitation; the second one still heats by laser a fixed horizontal plate of about 200 µm. Both apparatuses have the possibility to heat the samples above their melting point.

The first study dealing with levitated balls showed that estimation of thermal diffusivity is possible under the condition that all the unwanted parameters present in the theoretical (inappropriate) flux-flux direct model are known: heat flux, absorption coefficient, view-factor… On the contrary, the second study, which uses this time a

temperature-temperature direct model, succeeded to estimate thermal diffusivity, the number of unwanted parameters being reduced to one. As said in Section 6.1.4, regarding the first study, a possibility to reduce the number of unknown parameters would be the development of a flux-flux model or a temperature-temperature model. The latter would be possible if emissivity of the metallic ball is known, which remains a difficult task as discussed in Section 5.

Inverse techniques used for estimation were different (OLS and Bayesian inference) but successful in both cases, which lets a variety of choices and possible comparisons.

However, the development of temperature-temperature models would not be possible without the technical quality of the experimental apparatuses. Experimentally, the use of several mirrors offers the possibility to see different scenes of the same sample at the same time and with the same measurement instrument (the high-speed camera). The physical nature of the input and of the observable is thus the same: here the radiative flux. This principle has already been tested and presented in Section 4 with materials at room temperature with the help of thermocouples. Now in Section 6, the sample temperatures being very high, the use of a laser heating proscribed thermocouples, which are substituted by visible or infrared camera. Therefore, a step of calibration of the camera has been added.

References

[Altenburg 2020] S. J. Altenburg, A. Straβe, A. Gumenyuk, and C. Maierhofer, "In-situ monitoring of a laser metal deposition (LMD) process: comparison of MWIR, SWIR and high-speed NIR thermography," *Quant Infrared Thermogr J*, 2020.

[Cotta 1997] R.M. Cotta, M.D. Mikhailov, Heat Conduction: Lumped Analysis, Integral Transforms, Symbolic Computation, John Wiley & Sons, Chichester, 1997.

[Cotta 2017] J.N. Cotta, Renato M., Knupp, D.C, Quaresma, Analytical Methods in Heat Transfer, in: F.A. Kulacki, V.K. Dhir, M.P. Mengüç (Eds.), Handb. Therm. Sci. Eng., Springer Open Ltd, 2017. doi:10.1007/978-3-319-32003-8.

[de Hoog 1982] F. R. de Hoog, J. H. Knight, and A. N. Stokes, "An Improved Method for Numerical Inversion of Laplace Transforms," *SIAM Journal on Scientific and Statistical Computing*, vol. 3, no. 3, pp. 357–366, Sep. 1982.

[Houssein 2023] Houssein Jad, et al., *A novel apparatus dedicated to the thermal diffusivity estimation of metals at high temperature*, International Journal of Thermal Science, accepted for publication.

[Jannot 2009] Y. Jannot, A. Degiovanni, and G. Payet, "Thermal conductivity measurement of insulating materials with a three layers device," *Int J Heat Mass Transf*, vol. 52, no. 5–6, pp. 1105–1111, Feb. 2009.

[Jannot 2018] Y. Jannot and A. Degiovanni, *Thermal properties measurement of materials*. Wiley Blackwell, 2018.

[Jannot 2020] Y. Jannot, A. Degiovanni, V. Schick, and J. Meulemans, "Thermal diffusivity measurement of insulating materials at high temperature with a four-layer (4L) method," *International Journal of Thermal Sciences*, vol. 150, p. 106230, Apr. 2020.

[Kim 1975] C. Kim, "Thermophysical properties of stainless steels," 1975.

[Lamien 2019] Bernard Lamien, Dylan Le Maux Mickaël Courtois, Thomas Pierre, Muriel Carin, Philippe Le Masson Helcio R. B. Orlande, *A Bayesian Approach for the Simultaneous Estimation of the Thermal Diffusivity and Thermal Conductivity of Aerodynamically Levitated Solid Metals at High Temperatures - Theoretical Study*, International Journal of Heat and Mass Transfer, 141, p. 265-281, 2019.

[Le Maux 2019] Le Maux, Dylan, et al. « Density measurement of liquid 22MnB5 by aerodynamic levitation ». *Review of Scientific Instruments*, vol. 90, n° 7, juillet 2019, p. 074904.

[Le Maux 2022] Le Maux, Dylan, et al. « Surface Tension of Liquid Fe, Nb and 304L SS and Effect of Drop Mass in Aerodynamic Levitation ». *Journal of Materials Science*, vol. 57, n° 25, juillet 2022, p. 12094-106.

[Le Maux 2023] Dylan Le Maux, et al., *La lévitation aérodynamique dédiée à l'estimation de la viscosité de métaux liquides*, Actes du congrès de thermique SFT, Reims, 30 mai – 2 juin 2023.

[Maillet 2000] Denis. Maillet, S. André, J. C. Batsale, A. Degiovanni, and C. Moyne, *Thermal quadrupoles: solving the heat equation through integral transforms*. Wiley, 2000.

[Maillet 2013] D. Maillet, Y. Jannot, and A. Degiovanni, "Analysis of the estimation error in a parsimonious temperature-temperature characterization

technique," *Int J Heat Mass Transf*, vol. 62, no. 1, pp. 230–241, Jul. 2013.

[Mills 2002] K. C. Mills, *Recommended values of thermophysical properties for selected commercial alloys*. Woodhead, 2002.

[More 1978] J. J. More, "The Levenberg-Marquardt: Implementation And Theory," *Numerical analysis: Springer, Berlin,Heidelberg*, pp. 105–116, 1978.

[Muller 2013] M. Muller, "Étude du processus d'initiation par laser de la combustion d'un alliage métallique sous atmosphère d'oxygène," thèse, École National Supérieur de Mécanique et d'Aéronautique, 2013.

[Ozisik 1993] M.N. Ozisik, Heat Conduction, John Wiley & Sons, Inc., New York, NY, 1993.

[Pierre 2022] T. Pierre, É. Geslain, M. Courtois, A. Magueresse, and T. Colinart, "In-plane thermal diffusivity estimation by radial fin method," *Infrared Phys Technol*, vol. 120, p. 103998, Jan. 2022.

[Stehfest 1970] H. Stehfest, "Algorithm 368: Numerical inversion of Laplace transforms [D5]," *Communications of the ACM, 13.1*. pp. 47–49, 1970.

[Touloukian 1977a] Y. Touloukian and C. Ho, "Thermophysical Properties of Selected Aerospace Materials. Part 2. Thermophysical Properties of Seven Materials," 1977. Accessed: May 11, 2022.

[Touloukian 1977b] Y. S. Touloukian, R. K. Kirby, and P. D. Desai, *Thermophysical properties of matter*, vol. 12. 1977.

General conclusion and perspectives

I have presented a synthesis of my activities as Associate Professor, where readers can find detailed conclusions at the end of Sections 4 to 6. Concerning my teaching activities, I wish to pursue and diversify my involvement in terms of teaching and administrative responsibilities. Regarding research, these last years have been an opportunity for me to develop my collaboration at different local, national, and international levels; and I also want to follow up on this investment by getting more involved through projects. I am about to co-direct a post-doctoral internship at UFRJ (Brazil) with Professor Helcio R. B. Orlande on the subject of understanding the development of microorganisms by flash method and inverse techniques. My previous stay in Rio de Janeiro was also an opportunity to meet Liviu Nicu, CNRS research director and director of the CNRS South America section: several possibilities for financial supports over different durations exist. But the construction of a collaborative project is still only at the maturation stage.

Perspectives regarding thermophysical characterization developed in Section 4 concern a less macroscopic approach to transport phenomena with a more rigorous consideration of the internal structure of materials. Literature provides many works on this aspect with the development of predictive models and multiphase and multiconstituent behaviors, as for hemp concretes or aerogels. The use of analytical models taking into account directional thermal conductivity seems more complicated. Finite difference numerical models will take over, always in the spirit of developing direct temperature-temperature models. From an experimental point of view, the in-progress thesis work of J. Houssein [ACL16] (on liquid metals) proposes a promising experimental method for bidirectional visualization of the material tested by a set of mirrors and visible thermography. As the temperature in this case is close to ambient, the measurement would be made by infrared thermography, which would be able to observe the propagation of the heat flow in all directions, an ideal situation to verify and quantify the anisotropy.

The first part of Section 6 has shown the limitation of presented flux-flux model concerning the estimation of thermal conductivity and diffusivity of levitated balls of

metals at temperature close to liquid state. Correlation between the aforementioned parameters of interest and the unknown ones makes impossible their proper estimation. Therefore, one interesting perspective would be to reformulate the direct flux-temperature model by a new temperature-temperature or flux-flux model. The number of parameters to estimate is then reduced to three: thermal conductivity, thermal diffusivity, and convective and radiative losses. The main issue deals with the calibration of the pyrometer and the experiment. As the ball turns around its vertical axis, it is necessary that the heat propagation in the ball is axisymmetric with a heating at the top of the ball.

My implication with the characterization of the physical properties at temperature around and above the melting point continues with the thesis of J. Houssein (defense in 2024) for thermal diffusivity; but also, with ANR project proposed by Associate Professor Mickaël Courtois (see Section 3) for the estimation of heat capacity and latent heat of liquid metal through levitation technique.

For the axis of research developed in Section 5 about multispectral pyrometry, efforts should be made on models of knowledge of emissivity according to the following dependencies: wavelength, roughness and surface impurities. Different methods of simultaneous estimation of temperature-emissivity couple have shown satisfaction, but their success is conditioned by the most reliable model of emissivity. If the emissivity model is satisfying, then the number and the position of the wavelengths should become less of a concern when the measurements are made by a spectroradiometer, which has a wide choice of wavelengths. A first look at the state of the art shows that some remarkable works on the study of oxidation kinetics or the effects of roughness have been undertaken for about twenty years mainly for metals, less for dielectrics since they are less of an issue *a priori*. The approach must be theoretical, experimental, and pragmatic at the same time. For that purpose, in the framework of the Carnot Art contribution, a collaborative project between IRDL and LAMIH (Université de Bourgogne) will be submitted for the specific study of emissivity as a function of roughness; the measurements will be made at room temperature initially.

Caractérisation de propriétés thermophysiques et mesure par pyrométrie multispectrale

Résumé : Deux axes majeurs sont présentés dans ce document. Le premier axe concerne la caractérisation des propriétés thermophysiques de matériaux de natures différentes par la mise en place de protocoles expérimentaux à partir de modèles analytiques et d'étude de sensibilité. La définition d'un protocole expérimental nécessite le développement d'un modèle direct analytique ou numérique. Le modèle analytique peut contrainte fortement les expériences, mais les temps de calcul sont le plus souvent plus courts qu'avec le modèle numérique, ce qui est confortable pour l'estimation de paramètre par techniques inverses. De plus, l'usage de modèle température-température diminue le nombre de paramètres inconnus par rapport à des modèles plus classiques flux-température.

Le second axe concerne l'estimation simultanée de la température et de l'émissivité par pyrométrie multispectrale. Elle repose sur un problème initialement sous-dimensionné et mène bien souvent dans une impasse puisque le caractère imprévisible de l'émissivité d'une surface ne permet pas de la définir théoriquement sous la forme d'un modèle direct.

Le point commun entre les deux thématiques est l'usage de techniques inverses pour l'estimation des paramètres d'intérêt. Parmi toutes celles existantes, plusieurs techniques ont été utilisées et parfois comparées : les techniques déterministes de type moindres-carrés (OLS et MLE) et les techniques stochastiques de type bayésien (MCMC, MAP, filtre de particule).

Characterization of thermophysical properties and measurement by multispectral pyrometry

Abstract: Two major themes are presented. The first axis concerns the characterization of the thermophysical properties of materials of different natures by setting up experimental protocols from analytical models and sensitivity studies. The definition of an experimental protocol requires the development of a direct analytical or numerical model. The analytical model can strongly constrain the experiments, but the calculation times are usually shorter than with the numerical model, which is comfortable for parameter estimation by inverse techniques. In addition, the use of temperature-temperature model reduces the number of unknown parameters compared to more conventional flux-temperature models.

The second axis concerns the simultaneous estimation of temperature and emissivity by multispectral pyrometry. It is based on an initially underdetermined problem and very often leads to a dead end. Indeed, the unpredictable nature of the emissivity of a surface does not allow to define it theoretically in the form of a direct model.

The common point between the two themes is the use of inverse techniques for the estimation of the parameters of interest. Among all the existing ones, several techniques have been used and sometimes compared: deterministic techniques of the least-squares type (OLS and MLE) and stochastic techniques of Bayesian type (MCMC, MAP, particle filter).